ISSN 1726-5479

SENSORS & TRANSDUCERS

vol. 267
4/24

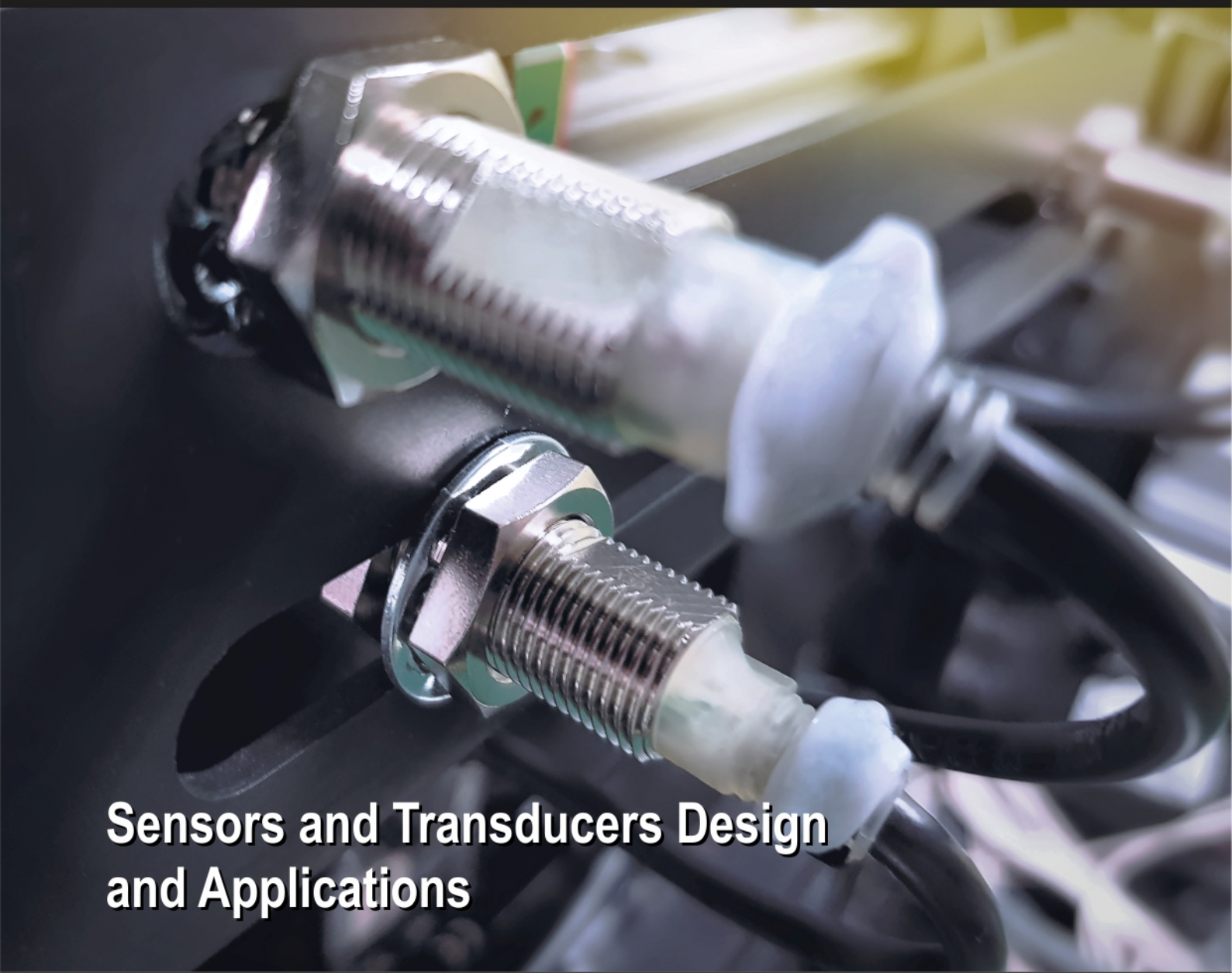

Sensors and Transducers Design and Applications

International Frequency Sensor Association Publishing

IFSA

Sensors & Transducers

International Official Open Access Journal of the International Frequency Sensor Association (IFSA) Devoted to Research and Development of Sensors and Transducers

Volume 267, Issue 4, December 2024

IFSA Publishing: Barcelona • Toronto

Published by International Frequency Sensor Association (IFSA) Publishing. Printed in the USA.

Sensors & Transducers

Volume 267, Issue 4
December 2024

www.sensorsportal.com

e-ISSN 1726-5479
ISSN 2306-8515

Sensors & Transducers journal is an open access, peer review international journal published monthly by International Frequency Sensor Association (IFSA).
Available in both: print and electronic (printable pdf) formats.

Sensors & Transducers Journal

Contents

Volume 267
Issue 4
December 2024

www.sensorsportal.com

ISSN 2306-8515
e-ISSN 1726-5479

Research Articles

Authors are encouraged to submit article in MS Word (doc) and Acrobat (pdf) formats
by e-mail: editor@sensorsportal.com. Please visit journal's webpage with preparation instructions:
https://sensorsportal.com/st_guide_for_authors.html

International Frequency Sensor Association (IFSA).

11th International Conference on Sensors and Electronic Instrumentation Advances

https://www.seia-conference.com/

24-26 September 2025
Ponta Delgada, San Miguel (Azores Islands), Portugal

SÃO MIGUEL SEIA'25

IFSA

The 11th annual SEIA' 2025 Conference is a key platform for sharing the latest in sensor and electronic instrumentation advancements, including AI-based sensor systems. It attracts global experts from academia and industry to discuss innovations in sensors, electronics, and measurement technologies. Since 2015, the event has been held in various locations, with the 2025 edition scheduled for 24-26 September in Ponta Delgada, San Miguel (Azores Islands), Portugal, alongside the 7th IFSA Frequency and Time Conference and the 7th MicDAT Conference under the same conference umbrella. Organized by the International Frequency Sensor Association (IFSA) - one of the main professional association serving the sensor industry and academy since 1999, the SEIA' 2025 also emphasizes networking, featuring social events like a welcome cocktail, Gala Dinner, and farewell cocktail.

Sensor Technology

- Accelerometers
- Inclinometers
- Gyroscopes
- Mechanical Sensors
- Optical Sensors
- Optical Fiber Sensors
- Photonic Sensors
- Chemical Sensors
- Biosensors
- Immunosensors
- BioMEMS
- Temperature Sensors
- Pressure Sensors
- Acoustic Sensors
- Electromagnetic Sensors
- Gas Sensors
- Humidity Sensors
- Infrared Sensors, Devices and Thermography
- Radiation Sensors
- Multi Sensor Fusion
- Smart Sensors
- Intelligent Sensors
- Artificial Intelligence based Sensors and Sensor Systems
- Virtual Sensors
- Sensor Interfacing and Signal Conditioning
- Sensor Calibration
- Nanomaterials and Electronics Technology for Sensors
- Semiconductor Materials for Sensors
- Polymer Materials for Sensors
- MEMS and NEMS
- Remote Sensors and Telemetry
- Sensor Applications

Sensor Instrumentation and Measuring Technology

- Metrology and Measurement Science
- Methods of Measurements
- Calibrations and Standards
- Measurement of Electrical Quantities
- Time and Frequency Measurements
- Measurement of Force, Mass, Torque, Inclination and Acceleration
- Magnetic Measurements
- Hardness Measurements
- Measurement of Geometrical Quantities
- Temperature and Thermal Measurements
- Pressure and Vacuum Measurements
- Vibration and Noise Measurement
- Flow Measurements
- Chemical Measurements
- Quantum Measurements and Photonics
- Acoustics and the Ultrasonic Measurements
- Environmental Measurements
- Power and Energy Measurements
- Measurement of Human Functions
- Measurements in Biology and Medicine
- Mathematical Tools for Measurements
- Optical and Radiation Measurements
- Microwave Measurements
- Virtual Instruments and Data Acquisition Systems
- Soft Measurements
- Measurement Systems
- Distributed Measurements
- Analog-to-Digital Converters, Digital and Mixed Signal Processing
- Waveform Analysis and Measurements
- Scientific and Industrial Instrumentation
- Cyber-Physical Systems and IoT
- Experimental Mechanics
- Measurement in Robotics
- Metrology in Food and Nutrition
- Intelligent and Computer Vision Instruments
- Reliability of Instrument and Measurement Systems
- Nanometrology
- Technical Diagnostics and Testing
- Nondestructive Testing
- Blockchain Applications in Metrology and Measurements
- Education and Training in Measurement and Instrumentation

Special Sessions:

Authors are welcome to propose and manage special sessions during the SEIA' 2025. Each special session will contain 4-6 papers in a related field as specified above.

Session organizers will get: Certificate of Appreciation; Free Registration; Special Publishing Theme within Conference Proceedings.

Contribution Types:

- Keynote Presentations
- Invited Talks
- Special Sessions
- Regular Sessions
- Poster Sessions
- Special Sessions
- Online Sessions
- Exhibition

Deadlines:

Submission (2-page extended abstract):	**30 May 2025**
Notification of acceptance:	**20 June 2025**
Registration:	**25 July 2025**
Camera ready and late registration:	**25 August 2025**

11th International Conference on Sensors and Electronic Instrumentation Advances

SÃO MIGUEL SEIA'25

https://www.seia-conference.com/

One event - three different publications !

1) All registered abstracts will be published in the conference proceedings (with the ISBN and DOI). Some previous SEIA Conference Series Proceedings are indexed in Conference Proceedings Citation Index (CPCI), Web of Science by Clarivate Analytics.

2) Authors will be invited to submit full-page extended papers to special issue of open access journal: Sensors & Transducers (ISSN: 2306-8515, e-ISSN: 1726-5479), published by IFSA Publishing, and indexed in Scopus.

3) The papers, presented at SEIA' 2025 may be extended to open access book chapters for the Book Series on 'Advances in Sensors', Vol. 9/10, 'Advances in Biosensors', Vol. 4 or 'Advances in Measurements and Instrumentation', Vol. 3/4. Some previous Book Series's volumes are indexed in the Book Citation Index (Wed of Science) by Clarivate Analytics.

Conference Hotel

The SEIA' 2025 Conference will take place in the Octant Hotel.
Address: Av. Dr. João Bosco Mota Amaral, 4 9500-771 Ponta Delgada, San Miguel, Portugal.

Social Programme

- Welcome Cocktail: 23 September 2025 (20:00-21:30).
- Gala Dinner: 25 September 2025 (20:00-23:00)
- Farewell Cocktail: 26 September 2025, Friday (during the poster session)

Organizing Committee

Chairman
Prof., Dr. Sergey Y. Yurish (IFSA, Spain),
e-mail: seia@sensorsportal.com

Advisory Chairman
Prof. Vijyakumar Varadarajan (Ajeenkya D Y Patil University India & La Trobe University, Australia)

Conference and Publication Manager
Tetyana Zakharchenko (IFSA Publishing, S.L., Spain)

Steering Committee:

Prof. Gennaro Conte (University Roma Tre, Italy)
Dr. Pavel Shuk (Saint-Gobain NorPro, USA)
Dr. Marius Gheorghe (Ideal Aerosmith, Inc., USA)
Dr. Paolo Dabove (Politecnico di Torino, Italy)
Prof. George Kiriakidis (European Materials Research Society (E-MRS), France)
Prof., Dr. Arkady Zhukov (Univ. of the Basque Country, Spain)

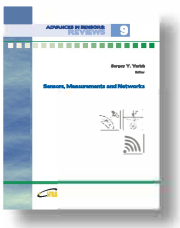


IFSA Publishing

F6S network partner

AJEENKYA D Y PATIL UNIVERSITY THE INNOVATION UNIVERSITY

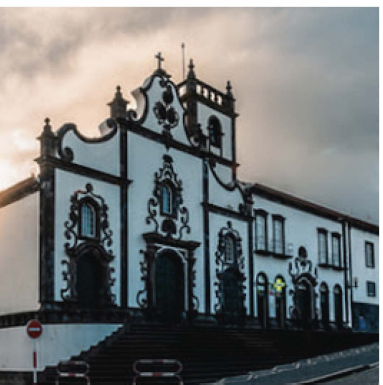


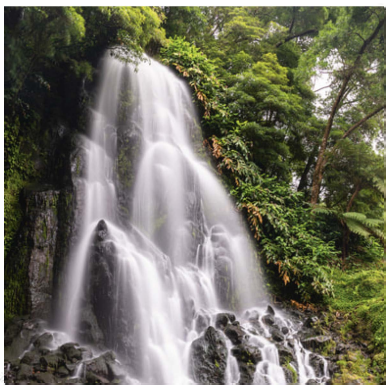

Sensors & Transducers, Vol. 267, Issue 4, December 2024, pp. 1-8

www.sensorsportal.com

Sensors & Transducers

Published by IFSA Publishing, S. L., 2024
http://www.sensorsportal.com

Application of MEMS Sensors in Evaluating Upper Limb Rehabilitation

[1, *] Yasutaka UCHIDA, [1] Eiichi OHKUBO and [2] Tomoko FUNAYAMA

[1] Department of Life and Science, 2-2-1 Senjusakuragi, Adachi-ku Tokyo,125-0045, Japan
[2] Department. of Occupational therapy, Teikyo University of Science, 2525, Yatsusawa, Uenoharashi, Yamanashi, 409-0193, Japan
[1] Tel.: +81369101010, fax: +8169103800
E-mail:uchida@ntu.ac.jp

Received: 30 August 2024 / Revised: 2 December 2024 / Accepted: 15 December 2024
Published: 30 December 2024

Abstract: As a first step toward creating a simple evaluation system for table sliding and peg movements in upper limb rehabilitation, experiments were conducted using STMicroelectronics' micro electro mechanical system (MEMS) board, its evaluation kit, and SensorTile.box. The experiment is conducted from two perspectives, including horizontal movement on the desk corresponding to the table slide and three-dimensional movement away from the table corresponding to the rehabilitation peg. UNICO was employed to assess the operation; software from STMicroelectronics was used to classify idle states, left-right motion states, and forward/backward motion utilizing decision trees. A sensor on a cloth detected features of the table slide during left-right motion, with three different speeds set: fast, slow, and stopped. To address the limitations of the USB cable connection imposed by the geometry and experimental setup, we also utilized SensorTile.box, which connects via Bluetooth and stores data for analysis on the built-in micro SD card. An accelerometer and a gyro sensor were used for the measurements. The results of the confusion matrix differed depending on whether both accelerometers and gyros were employed. A comparison of the accuracy of feature detection by machine learning cores created solely from various accelerometers revealed that the peak-to-peak core was more accurate. Sensor trajectories were obtained from the calculations. It was observed that once stationary, movements back to the origin did not calculate accurately at slow speeds due to errors in trajectory calculations, although repetitive movements were confirmed. However, repetitive movements were confirmed.

Keywords: MEMS sensor, Upper limb rehabilitation, UNICO, Table slide exercise, Machine learning, Decision tree, Imufusion.

1. Introduction

The accurate assessment of a patient's condition is crucial for providing appropriate medical support. Similarly, an accurate assessment of rehabilitation effectiveness is necessary for occupational and physical therapists. Assessing whether therapy and exercises are tailored to a patient's condition and level, as well as objectively measuring the degree of recovery, can effectively support medical rehabilitation and healthcare [1-6]. Practicing table slides, which reduce the weight on the upper limbs, is part of upper limb rehabilitation. This exercise does not require the patient to lift the upper limb, thus encouraging movement without excessive tension on or around the shoulders. Depending on the patient's condition, the below-elbow was placed on a towel or a skateboard and moved accordingly. Motion analysis using motion markers is effective but requires special equipment, making it expensive. Consequently, Leap Motion and Kinect are primarily used to recognize hand gestures [7-13]. However, ordinary medical professionals find it challenging to adjust program settings and movement ranges to match the

rehabilitation level required by the patient. We believe that rehabilitation efficiency can be improved using a system that employs inexpensive accelerometers, which can be easily attached, detached, and evaluated based on an individual's activity level [14].

In this paper, the experiment is conducted from two perspectives, including horizontal movement on the desk corresponding to the table slide and three-dimensional movement away from the table corresponding to the rehabilitation peg. We examined the possibility of using a micro electro mechanical system (MEMS) sensor with user-friendly software for upper limb rehabilitation and demonstrated its potential for use in rehabilitation settings using a Bluetooth-connected model. We also verified the free-movement trajectory, which is an advantage of not requiring a connected USB cable.

2. Experiments

An MK109V3 from STMicroelectronics [15] was combined with a MEMS board (LSM6DSOX) to evaluate the motion of sliding a towel on a desk as a test experiment. Fig. 1 shows the MK109V3 connected to a PC via USB. It measures 5 cm square with a maximum thickness of 1.5 cm due to the expansion board being inserted into a pin header socket. UNICO was used as the evaluation software provided by the company.

Fig. 1. MK109V3 connected to a PC through a USB cable.

A photograph of the Sensortil.box [16] is shown in Fig. 2. The box connects to a smartphone via Bluetooth, eliminating the need for cables. In addition, the side of the rectangular sensor facing up can be displayed on a smartphone screen in real time. As the swipe action in this study involves two directions, as illustrated in Fig. 3, investigating its feasibility would be straightforward. A compact version of the quaternion data used for this display can be obtained and the measurement data can also be sent as an attachment file following measurement. Values from other sensors, such as accelerometers and gyroscopes, are stored as comma separated value (CSV) files on a micro SD card and can be transferred to a PC These data were used to calculate the trajectories.

The accelerometer sensitivity was set to 2 [g], where g is the acceleration of gravity, based on instructions displayed on the PC screen by the UNICO software, assuming sensitive three-dimensional motion. In the MK109V3 experiment, the sampling frequency was set to 26 [Hz] for horizontal and vertical movement during the table swipe experiment. For experiments with different slide speeds, the sampling frequency was set to 12.5 [Hz] to limit data quantity. A frequency of 100 [Hz] was used for the experiments with SensorTile.box.

Fig. 2. Photograph of Sensortile.Box.

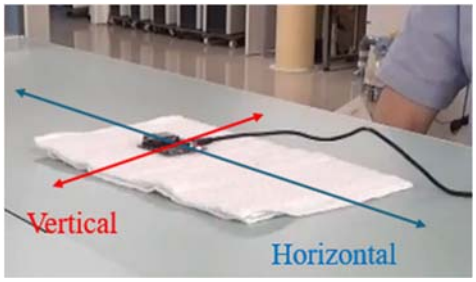

Fig. 3. Defining swiping direction.

Participants were two males in their 60s (A) and 40s (B). Approval for this study was obtained from the Ethics Committee of Teikyo University of Science.

3. Results

3.1. MEMS Board Connected to PC

Fig. 4 illustrates an example of the acceleration and gyroscopic display from the MEMS sensor during reference data training. The waveform at the top of the screen represents that of the acceleration sensor. When the reference data was created, the measurement range was set to ±2[g], and the gyro sensor was set to ±125 [deg/sec]. As shown in the figure, the sensor was placed on cloth to simulate motion analysis conditions. The horizontal and vertical directions of sensor movement are shown in the figure. When stable, a value of 1[g] corresponding to gravity was obtained in the Z-axis direction. For testing, the sensor was manually lifted and swung repeatedly from left to right. Acceleration and gyroscopic signals corresponding to the z-axis direction and right-left movement in response to lifting were recorded. The signal from the acceleration sensor is intuitive, whereas that from the gyro sensor is complex.

Therefore, it is necessary to consider that when the sensor attached to the cloth was slid, the RAW data measured not only the acceleration in the XYZ directions but also the rotational component measured by the gyro sensor.

Table 1 presents an example of acceleration and gyro data during learning. For Subject A, the accelerations on the z, x, and y axes were 1004 [mg], -38.796 [mg], and 14.762 [mg], respectively. The x- and y-axis accelerations were not zero because the board was placed on a desk connected to a USB cable, which may have caused a slight tilt. The z axis represents approximately 1 [g].

Fig. 4. Example of the display of acceleration from the MEMS sensor.

Table 1. Acceleration example.

A_X [mg]	A_Y [mg]	A_Z [mg]	G_X [dps]	G_Y [dps]	G_Z [dps]
-38.80	14.76	1004	0.1138	-0.6475	-0.1488
-47.28	16.29	1006	0.1138	-0.62125	-0.1575
-41.60	18.67	1004	0.1225	-0.6475	-0.1575
-39.77	19.09	1004	0.1138	-0.63875	-0.175
-41.85	17.81	1004	0.1313	-0.65625	-0.175

There are 12 different types of movements that can be performed with a machine learning core (MLC)-embedded MEMS sensor. Table sliding involves simple horizontal and vertical motions rather than lifting a load that adds stress to the shoulders. In this study, the motion involved moving a cloth. As this was a basic experiment, the sensor unit was placed on a cloth. The forward, backward, left, and right movements were straightforward. However, because of the likely shaking of the sensor itself, it was considered suitable to use both the acceleration and gyro sensors. The features to be used in the MLC were also examined.

$$\text{Mean: } \frac{1}{WL}\sum_{K=0}^{WL-1} I_K, \tag{1}$$

$$\text{Var: } \left(\frac{\sum_{K=0}^{WL-1} I_K^2}{WL}\right) - \left(\frac{\sum_{K=0}^{WL-1} I_K}{WL}\right)^2 \tag{2}$$

Fig. 5 shows an example of an Unico Configuration file (ucf) automatically created by the software. In the figure, 0 is “idle” for stop, 4 is “RL” for horizontal movement, and 8 is “Updown” for vertical movement.

```
├- Machine Learning Core Tool v9.17.2.0, LSM6DSOX
-- <MLC0_SRC>DT1,0='idle',4='RL',8='Updown'


Ac 10 00
Ac 11 00
Ac 01 80
Ac 04 00
Ac 05 00
Ac 17 40
```

Fig. 5. Unico configuration file using UNICO.

The accuracy as compared using the confusion matrix with the selected features is presented in Table 2. Based on the initial experimental results and feature values commonly used in inertial measurement sensors, we considered as meaningful indicators the mean (Mean) and variance (Var) shown in the following equations along with the amplitude and magnitude of acceleration in the vertical and horizontal directions. Peak amplitude (PP) and peak detection (P) were added to the measurements. In the table, the acceleration value is denoted as ACC, and the gyro value is denoted as GY.

Table 2. Accuracy comparison using selected features form the confusion matrix.

	Mean	Var	PP	P	PP & P	Accuracy [%]
GY	✓					90.0
GY		✓				92.0
GY	✓	✓				92.2
GY			✓			91.1
GY					✓	91.1
ACC	✓					97.3
ACC		✓				98.7
ACC	✓	✓				100.0
ACC			✓			97.3
ACC				✓		52.2
ACC					✓	97.5

Fig. 6 shows Unico configuration file created using the UNICO software. This figure shows the training class for the three patterns: idle, RL, and Updown.

```
├- Machine Learning Core Tool v9.17.2.0, LSM6DSOX
-- <MLC0_SRC>DT1,0='idle',4='RL',8='Updown'


Ac 10 00
Ac 11 00
Ac 01 80
Ac 04 00
Ac 05 00
Ac 17 40
```

Fig. 6. Unico configuration file created using UNICO.

Fig. 7 shows the features used for classification in the decision tree. The features used in this case were the MEAN and VAR of the accelerations x, y, and z.

```
class:
 => idle, RL, Updown,
features:
 => F1_MEAN_on_ACC_X, F2_MEAN_on_ACC_Y, F3_MEAN_on_ACC_Z,
F4_MEAN_on_ACC_V, F5_VAR_on_ACC_X, F6_VAR_on_ACC_Y, F7_VAR_on_ACC_Z,
F8_VAR_on_ACC_V,
```

Fig. 7. Features used for classification.

Fig. 8 shows actual decision trees created for the accelerometer case. This is an example of how the features used in the classification are displayed in a file. The selected features are mean and variation.

```
F5_VAR_on_ACC_X <= 2.26533e-005
|  F1_MEAN_on_ACC_X <= -0.0404968: idle (180.0)
|  F1_MEAN_on_ACC_X > -0.0404968
|  |  F1_MEAN_on_ACC_X <= -0.000855923: RL (6.0)
|  |  F1_MEAN_on_ACC_X > -0.000855923: Updown (1.0)
F5_VAR_on_ACC_X > 2.26533e-005
|  F5_VAR_on_ACC_X <= 0.00227706
|  |  F6_VAR_on_ACC_Y <= 0.000582436
|  |  |  F2_MEAN_on_ACC_Y <= 0.0077095: Updown (5.0)
|  |  |  F2_MEAN_on_ACC_Y > 0.0077095
|  |  |  |  F1_MEAN_on_ACC_X <= -0.0310669
|  |  |  |  |  F1_MEAN_on_ACC_X <= -0.0350037: RL (1.0)
|  |  |  |  |  F1_MEAN_on_ACC_X > -0.0350037: Updown (1.0)
|  |  |  |  F1_MEAN_on_ACC_X > -0.0310669: RL (18.0)
|  |  F6_VAR_on_ACC_Y > 0.000582436: Updown (148.0)
|  F5_VAR_on_ACC_X > 0.00227706
|  |  F6_VAR_on_ACC_Y <= 0.00146479: RL (155.0)
|  |  F6_VAR_on_ACC_Y > 0.00146479
|  |  |  F5_VAR_on_ACC_X <= 0.00579834
|  |  |  |  F6_VAR_on_ACC_Y <= 0.00180817
|  |  |  |  |  F6_VAR_on_ACC_Y <= 0.00162315: Updown (2.0)
|  |  |  |  |  F6_VAR_on_ACC_Y > 0.00162315: RL (2.0)
|  |  |  |  F6_VAR_on_ACC_Y > 0.00180817: Updown (24.0)
|  |  |  F5_VAR_on_ACC_X > 0.00579834: RL (5.0)

Number of Leaves  :   13
Size of the tree :    25
```

Fig. 8. Decision tree formed using features mean and validity.

Fig. 9 shows another example of the features used for classification in the decision tree. The features used in this case were the peak-to-peak accelerations in the x, y, and z directions.

```
class:
 => idle, RL, Updown,
features:
 => F1_PeakToPeak_on_ACC_X, F2_PeakToPeak_on_ACC_Y,
F3_PeakToPeak_on_ACC_Z, F4_PeakToPeak_on_ACC_V,
```

Fig. 9. Features used for classification.

Fig. 10 shows the actual decision trees created for the accelerometer. This is an example of how the features used in the classification are displayed in a file. The selected features are mean and variation.

```
F2_PeakToPeak_on_ACC_Y <= 0.0178518
|  F1_PeakToPeak_on_ACC_X <= 0.0250092: idle (180.0/6.0)
|  F1_PeakToPeak_on_ACC_X > 0.0250092: RL (1.0)
F2_PeakToPeak_on_ACC_Y > 0.0178518
|  F1_PeakToPeak_on_ACC_X <= 0.228087
|  |  F2_PeakToPeak_on_ACC_Y <= 0.118364
|  |  |  F1_PeakToPeak_on_ACC_X <= 0.146729: Updown (25.0/5.0)
|  |  |  F1_PeakToPeak_on_ACC_X > 0.146729
|  |  |  |  F3_PeakToPeak_on_ACC_Z <= 0.0375977: RL (21.0)
|  |  |  |  F3_PeakToPeak_on_ACC_Z > 0.0375977
|  |  |  |  |  F1_PeakToPeak_on_ACC_X <= 0.175781: Updown (4.0)
|  |  |  |  |  F1_PeakToPeak_on_ACC_X > 0.175781
|  |  |  |  |  |  F2_PeakToPeak_on_ACC_Y <= 0.109558: RL (9.0)
|  |  |  |  |  |  F2_PeakToPeak_on_ACC_Y > 0.109558: Updown (1.0)
|  |  F2_PeakToPeak_on_ACC_Y > 0.118364: Updown (128.0/3.0)
|  F1_PeakToPeak_on_ACC_X > 0.228087
|  |  F2_PeakToPeak_on_ACC_Y <= 0.163949: RL (131.0)
|  |  F2_PeakToPeak_on_ACC_Y > 0.163949
|  |  |  F1_PeakToPeak_on_ACC_X <= 0.328857: Updown (20.0/1.0)
|  |  |  F1_PeakToPeak_on_ACC_X > 0.328857
|  |  |  |  F2_PeakToPeak_on_ACC_Y <= 0.279785
|  |  |  |  |  F3_PeakToPeak_on_ACC_Z <= 0.10791: RL (9.0)
|  |  |  |  |  F3_PeakToPeak_on_ACC_Z > 0.10791
|  |  |  |  |  |  F1_PeakToPeak_on_ACC_X <= 0.395508: Updown (1.0)
|  |  |  |  |  |  F1_PeakToPeak_on_ACC_X > 0.395508: RL (1.0)
|  |  |  |  F2_PeakToPeak_on_ACC_Y > 0.279785: Updown (2.0)

Number of Leaves  :   14
Size of the tree :    27
```

Fig. 10. Decision tree formed using feature is peak-peak.

When the initial experiments were conducted under conditions that achieved high accuracy with the confusion matrix extracted as a feature quantity, false positives were occasionally recorded when the direction of motion changed while using a gyro sensor. Table 3 summarizes the results.

Table 3. Accuracy dependence of feature value and state.

Feature value	Sate	Accuracy [%]
Mean	Idle	100
	RL	86.6
	Up & Down	99.6
Variance	Idle	100
	RL	96.9
	Up & Down	87.0
P-P	Idle	100
	RL	90.4
	Up & Down	99.6
P-P & Peak	Idle	100
	RL	87
	Up & Down	91.6

In the table sliding experiments, the speed and distance of sliding are important. We attempted to determine the movement of the table slide by learning three horizontal movement speeds: stationary, slow, and normal. The movement speed and trajectory were also calculated.

The results of constructing a decision tree with horizontal acceleration based on learning the horizontal motion in stationary, slow, and normal speed are states shown in Fig. 11.

```
F1_VAR_on_ACC_X <= 0.00150373
|  F1_VAR_on_ACC_X <= 1.19209e-007:
stable (65.0)
|  F1_VAR_on_ACC_X > 1.19209e-007: slow
(72.0)
F1_VAR_on_ACC_X > 0.00150373: fast (67.0)

Number of Leaves :    3
Size of the tree :    5
```

Fig. 11. Decision tree with horizontal acceleration.

The confusion matrix is shown in Fig. 12; the accuracy obtained was 100 %, although a slight variation was observed in the number of states.

```
===== Confusion Matrix =====
          stable    slow      fast
stable    65        0         0
slow      0         72        0
fast      0         0         67

Total Number of Instances        : 204
Correctly Classified Instances   : 204
Incorrectly Classified Instances : 0
Kappa Statistic: 0.333958
Accuracy: 100%
```

Fig. 12. Confusion matrix.

The trajectory obtained from the line when the sensor moved horizontally was calculated. The trajectory is computed using the imufusion Python package, which tracks the position of the sensors attached to the subject's foot while walking. The Fusion algorithm obtains a measure of acceleration in the Earth's coordinate system from the gyroscope and accelerometer data. The acceleration measurements

are then combined to obtain velocity measurements. The velocity measurements are corrected for drift using a zero-velocity detection algorithm and then integrated to obtain the position measurement. The Attitude and Heading Reference System algorithm was not used in this study because the parameters have not been optimized. Therefore, the accuracy cannot be considered inadequate.

Acceleration was used as the feature quantity for Subject A. The measurement results are shown in Fig. 13. It can be seen that slow (4) and normal (8) movement speeds are distinguished. A 0 value indicates a stationary state.

Fig. 14 shows the classification results when stationary and slow-moving speed states are differentiated. Stationary and slow-moving speeds often resulted in misclassification of stationary conditions.

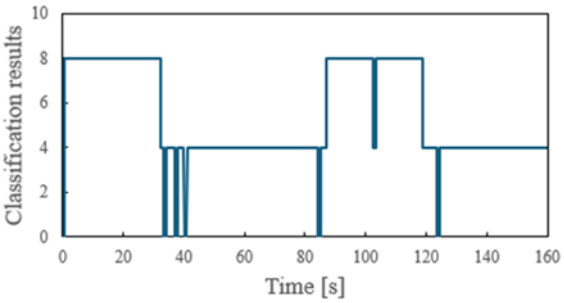

Fig. 13. Classification results between slow and normal movement speeds.

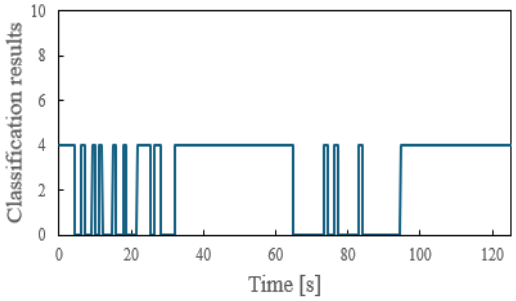

Fig. 14. Classification results between stationary and slow states.

Next, we measured the participants who were not involved in the creation of the teacher data and found a wide variation in judgments for the three conditions. The results are shown in Fig. 15.

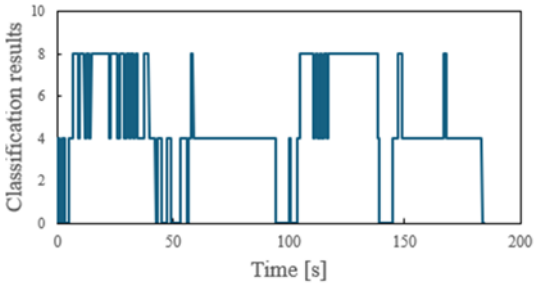

Fig. 15. Classification results on subjects who were not involved in the creation of the teacher data.

It is known that the actual speed and degree of movement are important in rehabilitation evaluation, and it is said to be important to obtain accurate trajectories [17-26]. The results of Subject A's horizontal movements are shown in Fig. 16: stopped for 10 s, moved left and right for 30 s at normal speed, stopped for 10 s, and moved left and right at a slower speed, calculated using imufusion [27-28].

The trajectory also calculated using imufusion is shown in Fig. 17. Although the trajectory has been shifted left and right due to insufficient correction, the motion reflects movement at normal speed. A change in movement speed caused a significant shift in the left-right direction.

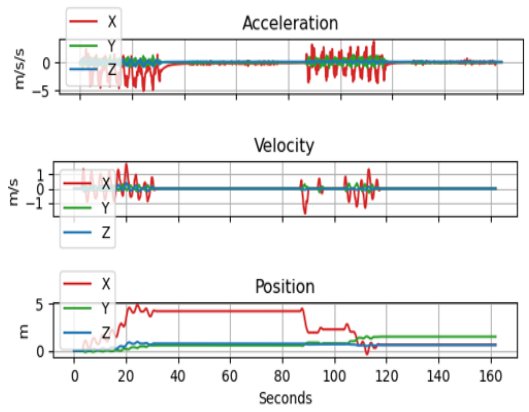

Fig. 16. Calculated velocity and position using acceleration with Subject A.

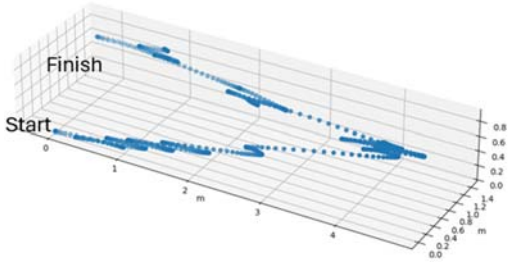

Fig. 17. Calculated trajectory calculated using imufusion with Subject A.

The results of the velocity and position calculations for Subject B are shown in Fig. 18.

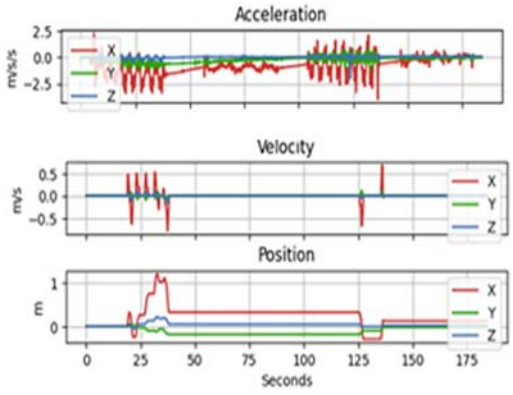

Fig. 18. Calculations of the velocity and position with Subject B.

The results of the trajectory calculations for Subject B are shown in Fig. 19. The movement pattern was the same as that of Subject A.

3.2. MEMS Board Connected via Bluetooth

Fig. 20 shows an example of the relationship between the sensor's face when facing up and the display on the smartphone screen.

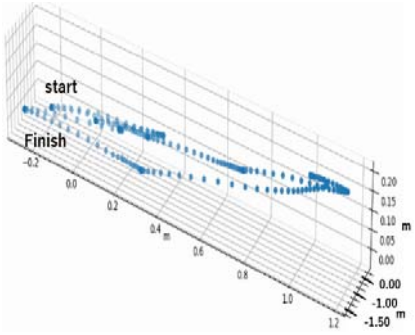

Fig. 19. Trajectory calculation by imufusion with Subject B.

Fig. 20. Example indication of which side is facing up.

As Fig. 20 shows, the screen display on the smartphone changes in response to the sensor's orientation, allowing the rotational motion of the sensor to be viewed in real time.

As Fig. 21 shows, the sensor box was lifted from rest for approximately 2 s and moved counter-clockwise in a parabolic trajectory, with each movement being stationary for approximately 2 s and the highest point being approximately 0.3 m high.

Fig. 21. Direction in which the sensor box was moved.

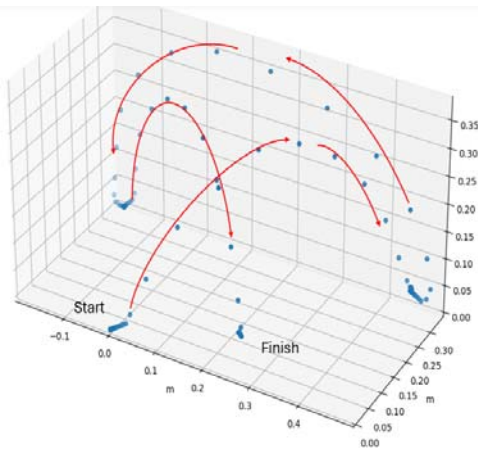

Fig. 22. Calculated sensor box trajectory.

4. Discussion

4.1. Reasons for Low Judgment in USB-connected Sensors

Accuracy was low when determining left-right movements, as shown in Table 3. This is believed to be due to the high accuracy from the confusion matrix resulting in large tree levels and sizes, enabling a more detailed classification. In the worst case, when only the peak values from the acceleration sensor were used, the accuracy was 52.2 %, with tree levels and sizes of (12, 23). By contrast, high accuracy was associated with larger tree levels and sizes. Accuracy was determined from a 10-s measurement. The higher accuracy obtained using only the accelerometer is thought to be due to the short measurement time of 10 s, during which the signal detected by the gyro sensor was negatively affected. Figs. 23 and 24 illustrate the change in judgment display over time from the starting point for left–right and up–down movements, respectively. The MEMS sensor detected three states: state 0, representing the idle state, state 4, representing the left/right horizontal movement, and state 8, representing the forward/backward vertical movement. We believe that the time required to achieve accurate detection immediately after the start of operation significantly affects accuracy. This is considered to be the reason for the occurrence of false readings.

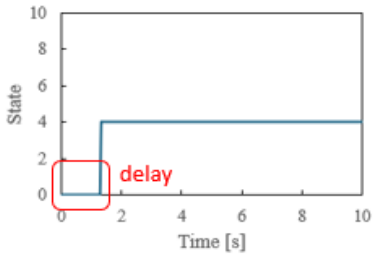

Fig. 23. RL states as a function of time.

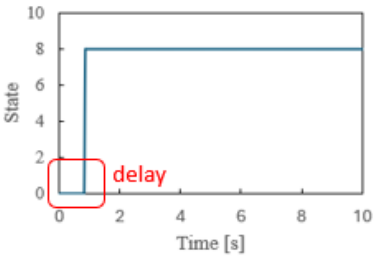

Fig. 24. Up and Down state as a function of time.

4.2. Reasons for Low Judgment in USB-connected Devices

The upward and downward directions in Fig. 18 correspond to the vertical direction, whereas the left and right directions correspond to the horizontal direction. As the swipe action in this study involved two directions, as illustrated in Fig. 2, investigating its feasibility was straightforward. The primary detection quantities were in the horizontal (left and right) and vertical (forward and backward) directions. The system was trained to detect an idle state where no movement occurred to determine whether it could accurately identify the actual movement states.

4.3. Trajectory

Numerous studies have been conducted on trajectory calculations. imufusion is said to provide accurate position information. However, in this study, errors accumulated, and large deviations occurred when the movement speed was slow. Because relatively accurate trajectories were obtained for the case shown in Fig. 22, where the movement speed was high, optimization of the parameters used in the calculation was considered necessary.

5. Conclusions

The ability to accurately detect horizontal motion indicates that accelerometers can be effectively attached to towels or skateboards used in rehabilitation to measure the process's effectiveness. The best conditions for feature extraction when using accelerometers as the sole sensor are peak-to-peak, alone, or in combination with peak values. This is consistent with decision-tree machine learning, which suggests that the simplest conditions are optimal. In this study, using a sensor box with Bluetooth connectivity, we demonstrated that more complex movements are possible and that trajectories can be obtained, albeit under specific conditions including movements corresponding to the 3-dimensional direction away from the table corresponding to the peg. We believe that the proposed MEMS board-based system has the potential to enhance the accuracy of rehabilitation effectiveness assessment when more complex movements are considered and when the proposed setup with skeletal recognition techniques measured using video recording are integrated.

Acknowledgements

This study was partially supported by JSPS KAKENHI (Grant Number: JP23K11207).

References

[1]. X. Liu, X. Zhang, B. Zhang, B. Zhou, Z. He, T. Liu, An IMU-based ground reaction force estimation method and its application in walking balance assessment, *IEEE Transaction on Neural System and*

Rehabilitation Engineering, Vol. 32, 2024, pp. 223-232.
[2]. E. Tijs, T. A. Matyas, Bilateral training does not facilitate performance of copying tasks in poststroke hemiplegia, *Neurorehabilitation and Neural Repair*, Vol. 20, 2006, pp.473-483.
[3]. L. Oujamaa, I. Relave, J. Froger, D. Mottet, J.-Y. Pelissier, Rehabilitation of arm function after stroke. Literature review, *Annals of Physical and Rehabilitation Medicine*, Vol. 52, 2009, pp. 269-293.
[4]. C. Brambilla, R. Marani, L. Romeo, M. L. Nicora, F. A. Storm, G. Reni, M. M. Malosio, T. O'Orazio, Azure Kinect performance evaluation for human motion and upper limb biomechanical analysis, *Helyon*, Vol. 9, 2023, e21606.
[5]. M. A. Murphy, A. Al-Shallawi, K. S. Sunnerhagen, A. Pandyan, Early prediction of upper limb functioning after stroke using clinical bedside assessment: a prospective longitudinal study, *Scientific Reports*, Vol.12, 2022, 22053.
[6]. G. Papagiannis, A. Trantafyllou,, K. G. Yiannopoulou, G. G. Georgoudis, et al., Hand dexterities assessment in stroke patients based on augmented reality and machine learning through a box and block test, *Scientific Reports*, Vol. 14, 2024, 10598.
[7]. M.-C. Jung, S.-J. Kim, J.-J. Rhee, D.-H. Lee, Electromyographic activities of the subscapularis, supraspinatus and infraspinatus muscles during passive shoulder and active elbow exercises, *Knee Surg. Sports Traumatol. Arthrosc.*, Vol. 24, 2016, pp. 2238-2243.
[8]. H. R. Fazeili, S. K. Venkatesh, Q. Peng, A virtual environment for hand motion analysis, *Procedia CIRP*, Vol. 78, 2018, pp. 127-132.
[9]. I. Pastor, H. A. Hayes, S. J. M. Bamberg, A feasibility study of an upper limb rehabilitation system using Kinect and computer games, in *Proceedings of the 34th Annual International Conference of Engineering in Medicine and Biology Society (EMBS'12)*, San Diego, USA, Aug. 28-Sppt. 1, 2012, pp. 1286-1289.
[10]. A. Rabin, E. Maman, O. Dolkart, E. Kazum, Z. Kozol, T. L Uhl, O. Chechil, Regaining motion among patients with shoulder pathology – are all exercise equal?, *Shoulder &Elbow*, Vol. 15, Issue 1, 2021, pp. 105-112.
[11]. N. D. Bruyn, L. Saene, L. Thijs, A. Van Gils, E. Ceulemans, B. Esser, C. Lafosse, Ma. Michielsen, H. Beyens, F. Schillebeechx, K. Alaerts, G. Verheyden, *Frontiers in Neurology*, Vol. 11, 2020, 597666.
[12]. K. Nagamune, et al., A development of wiping rehabilitation system using leap motion for patients with upper limb paralysis, in *Proceedings of the World Automation Congress (WAC'22)*, San Antonio, USA, 11-15 October 2022.
[13]. J. A. Cross, J. deVries, M. Mocarski, N. C. Ketchum, E. Compty, J. M. Fritz, C. S. Vetter, M. Krimmer, Electromyography of the shoulder musculature during passive rehabilitation exercises, *J. Shoulder and Elbow Arthroplasty*, Vol. 4, 2020, pp. 1-8.
[14]. Y. Uchida, E. Ohkubo, T. Funayama, A proposal for an evaluation method of table slide exercise using a MEMS sensor, in *Proceedings of the 10th International Conference on Sensors Engineering Electronics Instrumentation Advance (SEIA'24)*, Ibiza (Balearic Island), Spain, 25-27 September 2024, pp. 59-62.
[15]. MEMS Motion Sensor Eval Boards STEVAL-MKI109V3, https://www.st.com/en/evaluation-tools/steval-mki109v3.html
[16]. SensorTile.box, https://www.st.com/en/evaluation-tools/steval-mkboxpro.html
[17]. Y. Wu, H. Zhu, Q. Du, S. Tang, A pedestrian dead-reckoning system for walking and marking time mixed movement using an SHSs scheme and a foot-mounted IMU, *IEEE Sensors Journal*, Vol. 19, Issue 5, 2019, pp. 1661-1671.
[18]. S. Ikiziglu, S. Heydarov, Accuracy comparison of dimensionality reduction techniques to determine significant features from IMU sensor-based data diagnose vestibular system disorders, *Biomedical Signal Processing and Control*, Vol. 61, 2020, 101963.
[19]. L. Tang, M. Shushtari, A. Arami, IMU-based real-time estimation of gait phase using multi-resolution neural networks, *Sensors*, Vol. 24, 2024, 2390.
[20]. H. Uchitomi, Y. Hirove, Y. Miyake, Three-dimensional continuous gait trajectory estimation using single Shank-Worn internal measurement units and clinical walk test application, *Scientific Reports*, Vol. 12, 2022, 5368.
[21]. M. D. Ellis, Y. Lan, J. Yao, J. P.A. Dewald, Robotic quantification of upper extremity loss of independent joint control or flexion synergy in individuals with hemiparetic stroke: a review of paradigms addressing the effects of shoulder abduction loading, *J. of NeuroEngineering and Rehabilitation*, Vol. 13, 2016, 95.
[22]. E. Rabb, J. J. Steckenrider, Walking trajectory estimation using multi-sensor fusion and a probabilistic step model, *Sensors*, Vol. 23, 2023, 6494.
[23]. W. Zhang, D. Wei, H. Yuan, Novel drift reduction methods in foot-mounted PDR system, *Sensors*, Vol. 19, 2019, 3962.
[24]. J. Chen, G. Liu, M. Guo, Data fusion of dual foot-mounted ins based on human step length model, *Sensors*, Vol. 2, 2024, 1073.
[25]. Q. Wang, P. Markopoulos, B. Yu, W. Chen, A. Timmermans, Interactive wearable system for upper body rehabilitation: a systematic review, *J. of NeuroEngineering and Rehabilitation*, Vol.14 2004, 20.
[26]. Y. Yin, J. Zhang, M. Guo, X. Ning, Y. Wang, J. Lu, Sensor fusion of GNSS and IMU data for robust localization via smoothed error state Kalman filter, *Sensors*, Vol. 23, 2023, 3676.
[27]. xioTechnologies/Fusion, https://github.com/xioTechnologies/Fusion
[28]. xioTechnologies/Gait-Tracking, https://github.com/xioTechnologies/Gait-Tracking?tab=readme-ov-file

Sensors & Transducers, Vol. 267, Issue 4, December 2024, pp. 9-19

Sensors & Transducers

Published by IFSA Publishing, S. L., 2024
http://www.sensorsportal.com

Trial of Gait Analysis Using a Bilateral Gait Measurement System with Detailed Toe-tip Measurements

[1, *] Eiichi OHKUBO, [1] Yasutaka UCHIDA, [2] Tomoko FUNAYAMA and [3] Yoshiaki KOGURE

[1] Department of Life and Science, Teikyo University of Science, 2-2-1 Senju sakuragi, Adachi-ku Tokyo,125-0045, Japan
[2] Department of Occupational therapy, Teikyo University of Science, 2525, Yatsusawa, Uenoharashi, Yamanashi, 409-0193, Japan
[3] Professor Emeritus Teikyo University of Science, 2-2-1 Senju sakuragi, Adachi-ku Tokyo, 125-0045, Japan
[1] Tel.: +81369101010, fax: +81369103800
[*] E-mail:ohkubo@ntu.ac.jp

Received: 29 May 2024 / Revised: 3 December 2024 / Accepted: 17 December 2024
Published: 30 December 2024

Abstract: A prototype insole sensor capable of measuring the gaits of both feet was developed. Feature analysis was performed using data acquired from simultaneous measurements of both feet. In addition, a dataset of peak values and rates of change was created from the acquired data and its application in machine learning was investigated. The results of the analysis using random forests showed that the rate of change was better at detecting detailed movements at the measurement points. The significance of the data obtained from the toes was confirmed. Therefore, we conducted an additional study using an insole sensor with more toe measurement points. Analysis of the rate of change showed the possibility of classification using toe-tip data. Therefore, random forest and principal component analyses were used.

In this study, we demonstrated the usefulness of insoles for recording detailed individualized toe data. By accumulating and analyzing the data, we demonstrated the possibility of obtaining a guideline for the measurement location according to the subject's symptoms.

Keywords: Pressure sensors, Insole, Health condition change, Arduino, Bluetooth, Classification.

1. Introduction

With the advent of the super-aging society, the importance of preventive technologies in nursing and medical care has increased. In Japan, efforts to promote prevention before serious diseases occur, such as screening for metabolic syndrome, are being actively implemented to control rising medical costs [1]. Walking is fundamental to maintaining good health. As an essential activity in daily living, walking has been the focus of research aimed at linking its assessment to activities of daily living [2]. Gait analysis is being studied as a noninvasive method for evaluation individuals [3]. It is used not only for gait training in rehabilitation, but also for treatment evaluation, for example in Parkinson's disease [4, 5]. Traditionally, video analysis based on videography has been widely used for gait analysis. Advances in sensor technology have led to the use of 3D motion analysis systems [6] and mat-type pressure-sensitive sensors [7]. However, these methods are expensive and require large installation spaces. The insole sensor provides a simple measurement method. The position can be sensed by placing the insole sensor inside the

shoe. There are also research studies exploring the use of machine learning to estimate data from insole sensors [8]. In Japan, insole sensors that are inexpensive and easy to use are primarily designed for sports training, such as running and golf, rather than for rehabilitation purposes [9]. Some commercially available insole sensors are sized by cutting the entire insole at the same ratio for fine adjustments, while others are adjusted by cutting only the toe portion [10]. However, achieving uniform adjustments has proven challenging, with the proportions varying between the toe and heel sides.

Although the heel tends to be considered important because of the large amount of weight placed on it, we considered data other than the heel to be important parameters in the detection of gait disorders.

Therefore, we developed a prototype insole sensor that can perform measurements using an inexpensive general-purpose sensor and investigated the measurement points. We found that there were variations in the intensity of the measurement data other than at the heel, depending on the sensor position, confirming the importance of the sensor measurement point [11, 12].

Our previous system could not simultaneously measure both feet at the same time. We improved the system so that both feet could be measured simultaneously. Using the measurement data of both feet, we investigated the possibility of determining the sensor positions based on the characteristics of the subject's gait, symptoms, and treatment policy. Using the acquired data, we studied an analytical method for classifying the gait state using machine learning and presented the results at the recent SEIA 2024 conference [13].

This study describes the results of a trial run using an improved insole sensor capable of measuring toe conditions, addressing a new problem identified during the conference presentation.

The research was approved by the Ethics Committee of Teikyo University of Science.

2. Experience

2.1. Improvements to the Bilateral Gait Measurement System

An insole sensor that enables gait measurement of both feet is shown in Fig. 1. Four measurement locations were set up: toe, heel, outer, and inner.

The toe, inner, and outer sensors were placed 15 mm, 70 mm, and 80 mm from the toe, respectively. The heel sensor was placed 25 mm from the edge of the heel. The same insole sensors were used for the subjects measured in this study because their shoe sizes were 27 cm and 25 cm. An Arduino nano (hereinafter Arduino) was used as the microcomputer for control, and an FSR402 from Interlink electronics was used as the sensor device [14]. The transmitted data was sent using a recording Windows PC (hereafter PC) running a data recording program.

A voltage of 5 V was applied to the pressure sensor to convert the resistance change of the sensor into a voltage change. The voltage converted signal was input to the analog port of the Arduino. Since the analog port is a 10-bit conversion, the input value was decomposed into 1024 steps. The decomposed data is converted to the maximum value of 256 by quartering it to match the data acquired in the past.

Four sensors are measured in turn, and after the data from all the sensors are acquired, the data from the four sensors are sent to the computer as one data block with delimiters to improve the processing speed.

The data sampling interval is estimated to be about 50 milliseconds. The sampling frequency is estimated to be 20 Hz from the sampling interval.

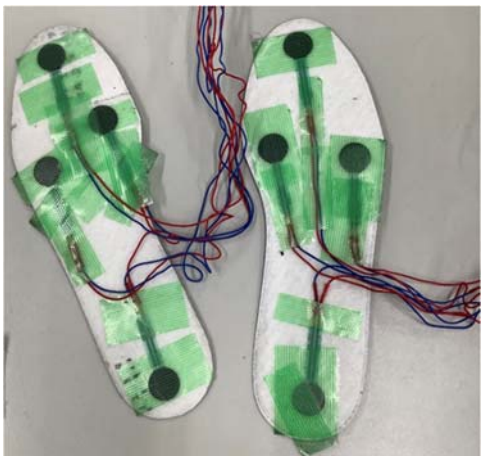

Fig. 1. Prototype insole sensor (bottom surface).

The system configuration is shown in Fig. 2.

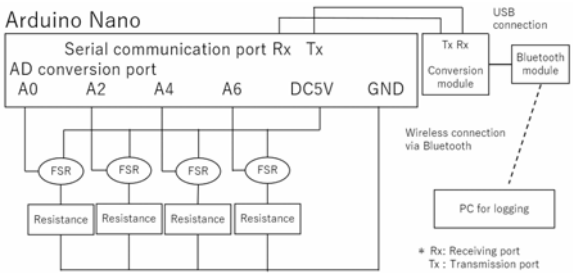

Fig. 2. System configuration.

A Bluetooth converter module acquires serial signals from the Arduino, which is placed on a 72 mm × 42 mm board with a 6F22 9 V battery. System components are sized to fit inside an adult shoe. The data acquisition interval of the PC is estimated to be about 0.1 sec maximum for one side based on the processing time of the Arduino and the delay caused by Bluetooth; data is recorded when the PC receives data from both sides. The devices on both

sides are not synchronized and send data to the PC independently.

The data received from the Arduino was recorded and stored in a Comma Separated Value (CSV) format file on the PC using a conversion program with processing. The elapsed time measured from the time of program operation on the PC was recorded in milliseconds, and the data was processed. The signals sent from the Arduino were recorded as one record in the CSV file as one set of data from both sides. An example of the data in the CSV file is shown in Table 1.

Table 1. Examples of recorded data.

time(s)	R toe	R out	R in	R heel	L toe	L out	L in	L heel	raw_R	raw_L
2.098	0	0	0	0	8	74	135	8	0 0 0 0	8 74 135 8
2.207	0	30	54	69	0	19	85	80	0 30 54 69	0 19 85 80
2.251	0	30	55	71	0	19	86	81	0 30 55 71	0 19 86 81
2.302	0	30	55	72	0	20	86	83	0 30 55 72	0 20 86 83
2.367	0	30	55	72	0	19	86	82	0 30 55 72	0 19 86 82

2.2. Improvements to the System with More Toe Measurement Points

To further analyze the toe data, we modified the insole sensors to include an additional toe measurement point and conducted additional experiments. The system configuration was modified to include two additional toe measurement points. A diagram of the modified system configuration is shown in Fig. 3.

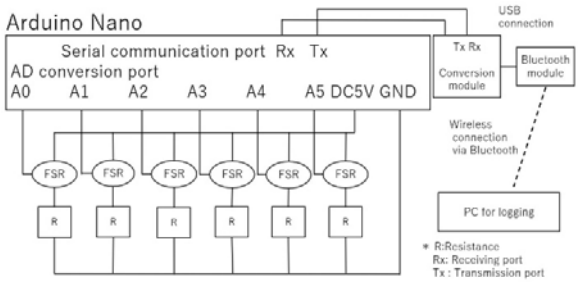

Fig. 3. System configuration after modification.

The Arduino used in this system comprised eight AD converters. As the number of measurement points increased to six, the port layout was changed to use six ports from A0 to A5. Because the assignment of the AD converters on the Arduino changed, the recording program running on the PC was also modified to correspond to the port assignment change. The circuit configuration, such as the sensor drive voltage, did not change. To avoid port-assignment errors when modifying the program, the elements in the raw data file were arranged in the same manner as in the AD conversion ports. An example of a modified data file is presented in Table 2.

Fig. 4 shows an enlarged view of the toe portion of the prototype insole. The distance from the toe to the center of the sensor was set at 10, 30, and 50 mm, with the 10 mm point representing the top of the toe and the 50 mm point representing the bottom of the toe. This configuration ensured that the pressure sensitive portions of the sensors did not overlap. If the same FSR402 was used, the flexible cable that received signals from the sensor and the sensor would overlap, and the pressure would not be applied correctly. Therefore, the FSR402 Shorttail, a model with the same sensing part but a shorter flexible cable, was used at the two additional locations.

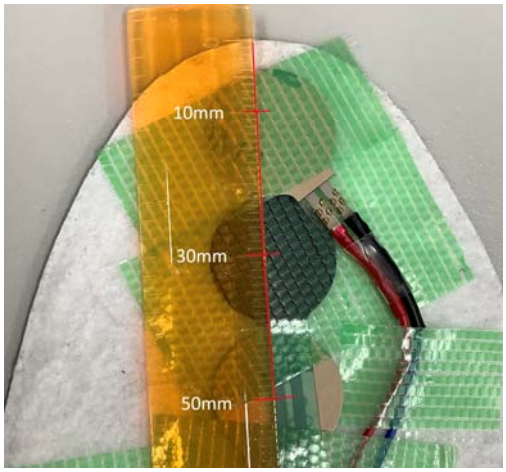

Fig. 4. Toe part improved on FSR402 (enlarged).

Table 2. Example of raw data file after modification.

time(s)	R toe	R out	R in	R heel	R toe top	R toe bottc	L toe	L out	L in	L heel	L toe top	L toe bottc	raw_R	raw_L
0.831	3	26	90	140	0	9	0	0	25	2	0	0	3 26 90 14	0 0 25 2 0 (
0.95	0	26	92	143	0	8	0	29	1	0	0	64	0 26 92 14	0 29 1 0 0 (
1.027	0	21	87	142	0	6	0	29	6	0	0	67	0 21 87 14	0 29 6 0 0 (
1.09	0	24	89	139	0	6	0	39	11	0	0	75	0 24 89 13	0 39 11 0 0
1.167	0	25	95	120	0	10	0	47	18	0	0	79	0 25 95 12	0 47 18 0 0

3. Results

3.1. Results of Bilateral Gait Measurements

Results of the experiment using data from healthy subjects are shown. A graph generated from the raw data is shown in Fig. 5. The transition of the acquired data waveforms indicated the shift in the load on both feet.

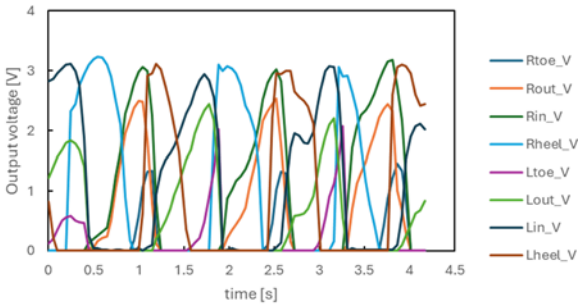

Fig. 5. Example of both feet (Right, Left) gait graph.

Gait feature extraction was performed to analyze the obtained data. Data were compared between normal walking and walking with a supporter attached to the subject's right knee to simulate a gait disorder. The data obtained were smoothed for feature extraction. Examples of the data from the right lateral sensor of the right foot, from which large features were obtained, are shown in Figs. 6 and 7. The vertical axis represents the standardized rate of change, and the horizontal axis represents the standardized sensor output voltage. The plotted data were cleansed, with the mean of the acquired data set to 0 and the standard deviation set to 1. Fig. 6 illustrates the feature extraction data in the normal state, with the center magnified.

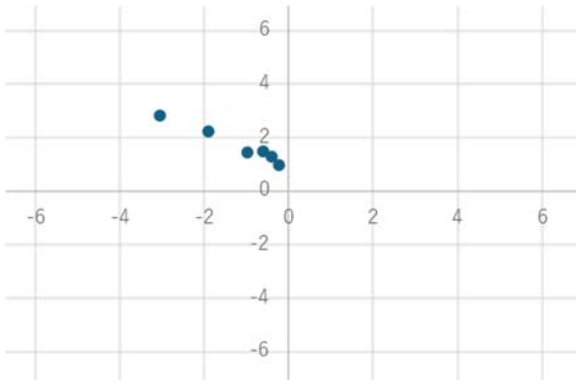

Fig. 6. Feature extraction (normal state).

Fig. 7 illustrates the feature extraction data in the right knee restriction state, with the center magnified.

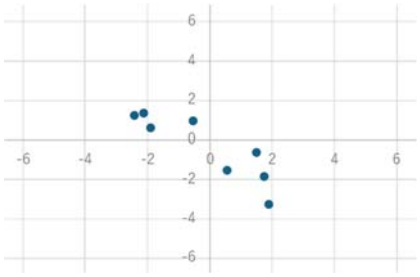

Fig. 7. Feature extraction (right knee restricted).

A comparison of Fig**.** 6 and 7 revealed that the set of plots tended to be divided between the normal and restricted states.

3.2. Increased Toe Measurement Results

As described in Section 3.2 a portion of Subject B's normal gait measurement data was clipped to generate a graph of the time variation of the input values to the AD converter. The results of all sensors on the right side are shown in Fig. 8; the results of the three sensor locations on the right toe are shown in Fig. 9; the results of all sensors on the left side are shown in Fig. 10; the results of three sensor locations on the left toe are shown in Fig. 11; the results of all sensors on both sides are shown in Fig. 12; the results of the three sensor locations on both toes are shown in Fig. 13.

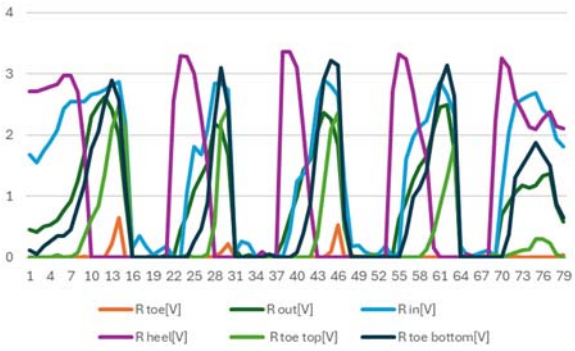

Fig. 8. Right side measurement data after modification.

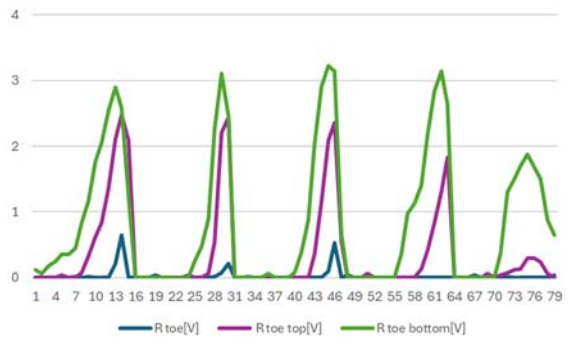

Fig. 9. Right side measurement data after modification (only 3 toe locations).

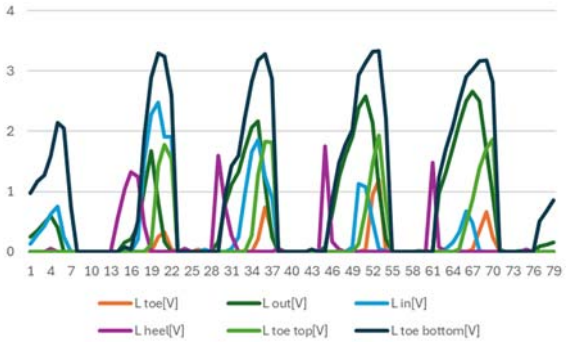

Fig. 10. Left side measurement data after modification.

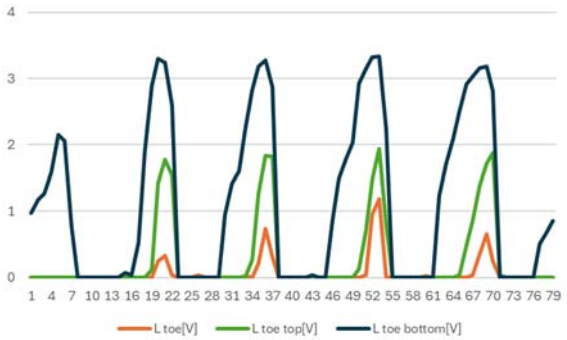

Fig. 11. Left side measurement data after modification (only 3 toe locations).

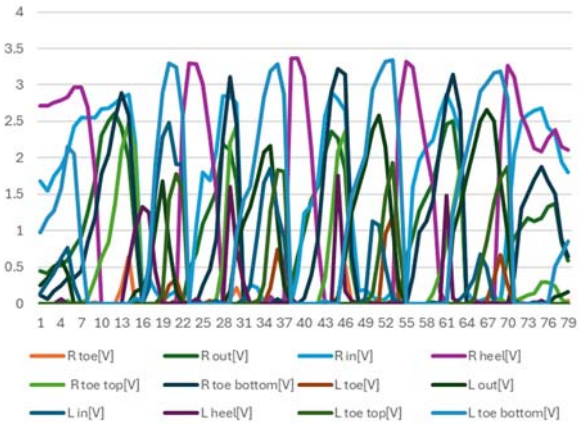

Fig. 12. Measurement data on both sides after modification.

By increasing the number of toe measurement points to three, we were able to confirm that we could measure motion at the tip of the toe (toe-top in the figure), the conventional toe, and the rear end of the toe (toe-bottom in the figure). In addition, the measurement results at the three locations were not the same and measurement results for individual sensor positions could be obtained.

4. Discussion

The collected data were further examined for classification using machine learning. This study employed Random Forest analysis to discriminate between sensors that were expected to have specific characteristics. The data used were the peak values for each sensor extracted from the raw data of the sensor values via from two healthy subjects, and the data based on which the rate of change per hour was calculated for each sensor.

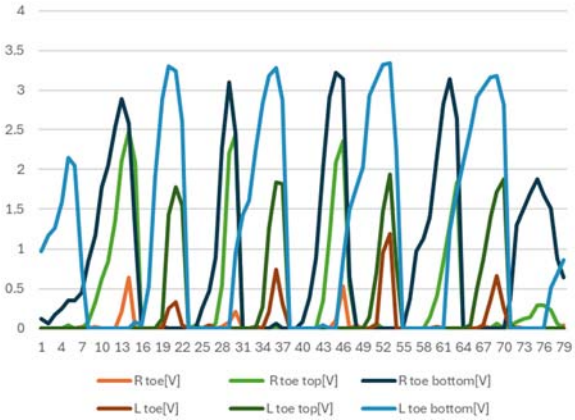

Fig. 13. Measurement data on both sides after modification (only 3 toe locations).

Herein, three measurement conditions were established. (1) normal gait data, (2) gait data with right knee restriction, and (3) gait data with left knee restriction.

The analysis was performed in Python using an analysis program based on Scikit-learn [15], a machine-learning library.

Elements with "-G" in the element names in the figures below indicate the rate of change (rate of change per hour). Elements without "-G" in their element names in the plots indicate the peak value data.

4.1. Analysis by Peak Value and Rate of Change

The peak value and rate of change datasets for Conditions (1), (2), and (3) were analyzed for the two subjects. The results are shown in Fig. 14.

The top eight elements were left heel, left inside-G, left heel-G, right heel, left toe-G, right heel-G, right outside, and right outside-G. There were four heel data points: one inside, one toe, and two outside the heel.

It was confirmed that the order of appearance of the left foot components was high, regardless of the restricted foot. The toes considered important were ranked lower than expected. The reason for the high ranking of the heel data was considered to be that it was a location wherein a greater load was applied compared to the other three locations.

The ratio of peak to rate of change for the top eight elements was 3 for the peak and 5 for the rate of change. Moreover, the ratio of the rate of change was

slightly higher; however, the ratios were almost the same.

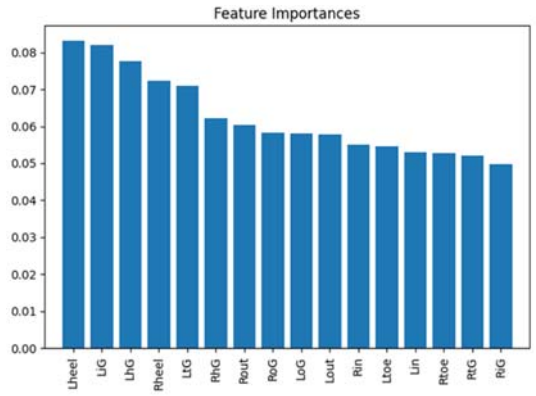

Fig. 14. Results of peak value and rate of change analysis.

4.2. Peak Value Analysis

To examine the existence of a difference between the peak value and rate of change, analyses were performed separately for the rate of change and peak value.

The peak value datasets for conditions (1), (2), and (3) were analyzed. The results of this analysis are shown in Fig. 15. Fig. 15 presents the results of the sensor peak value analysis in the following order of increasing values: left heel, right heel, right outside, left outside, right inside, left inside, right toe, and left toe. The results analyzed based on the peak values exhibited a higher ranking of heel values.

Moreover, a relatively high load on the heel and low load on the toe influenced the order of appearance. This confirmed that a greater load applied to the heel influenced the magnitude of the sensor value.

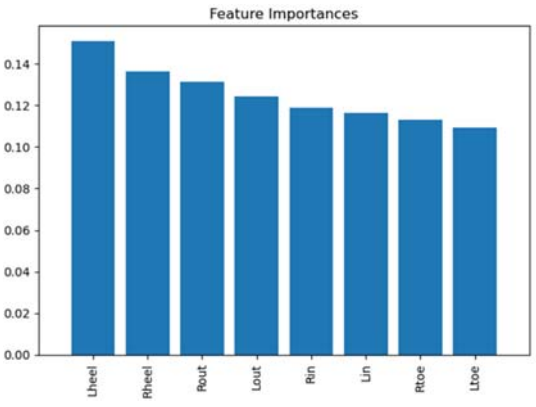

Fig. 15. Analysis results of sensor peak values.

4.3. Analysis by Rate of Change

The rate of change dataset for conditions (1), (2), and (3) was analyzed. The results are presented in Fig. 16.

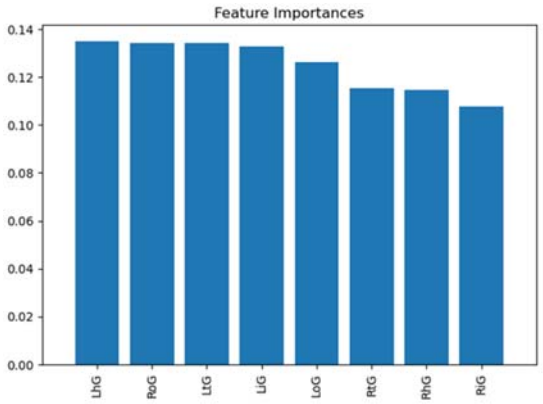

Fig. 16. Result of sensor rate of change analysis.

Fig. 16 shows the results in the order of increasing value: left heel, right outside, left toe, left inside, left outside, right toe, right heel, and right inside. Independent of the restricted foot, the component values of the left heel, Left toe, and Left inside were high. In contrast to the peak value results, the toe component had a higher rank. By examining the rate of change, we determined that the toe data buried in the peak values could be detected.

4.4. Subject Differences Analysis

To confirm the subject differences, the peaks and rates of change of the data for conditions (1), (2), and (3) were analyzed separately for each subject. The results of the data analysis of Subject A (male in his 40s, foot size 27 cm) are shown in Fig. 17. Fig. 17 shows that the four highest values were for the left heel-G, left inside, left inside-G, and left heel. The component value of Left was large, regardless of the restricted foot.

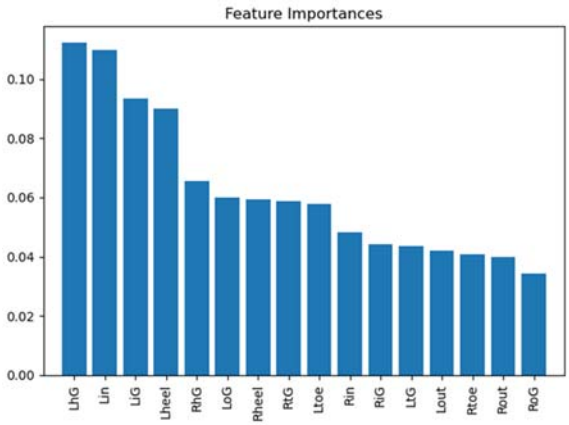

Fig. 17. Analysis results for Subject A.

Fig. 18 shows the results of the data analysis for Subject B (male in his 60 s, foot size 25 cm).

As evident, the top four highest values were for the right outside, left inside, left inside-G, and left toe. The

component values of the left and left toes were large, regardless of the restricted leg.

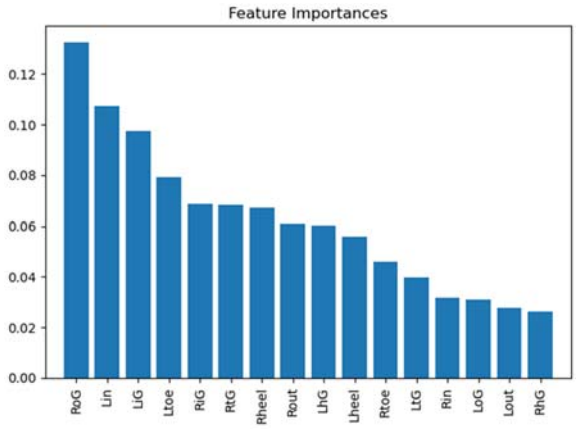

Fig. 18. Analysis results for Subject B.

A comparison of Figs. 17 and 18 revealed that the top four components were different, although the left-side value was high. Further, the composition ratio of the sensor values varied among subjects. In addition, it was possible for each subject to be authenticated according to its frequency of occurrence.

4.5. After Modification

From Section 4.5, the results of the improved toe measurement section will be discussed.

4.5.1. Comparison Using Peak Values at Three Toe Locations after Modification

Peak values were obtained from the data at the three toe locations. Fig. 19 shows the relationship between the sensor position and the average peak value, and Fig. 20 shows the relationship between the sensor position and the maximum peak value. The vertical axis of the graph represents the voltage of the sensor and the sensor position represents the distance from the tip to the center of the sensor, as shown in Fig. 4.

From Figs. 19 and 20, a difference in output was observed at the tip of the toe depending on the limiting condition, with the output value being relatively high. The output value at the rear end of the toe(toe-bottom) was consistently high, but showed minimal variation across different limiting conditions. The central part of the toe showed the largest difference depending on the constraint state; however, the output values obtained were low. Therefore, we considered that data from the tip of the toe, which could not be measured previously, would be more suitable for analysis.

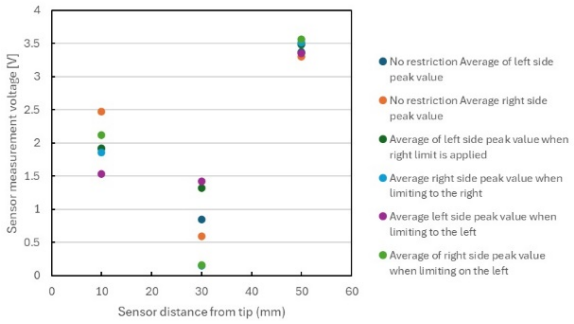

Fig. 19. Relationship between sensor position and average peak value.

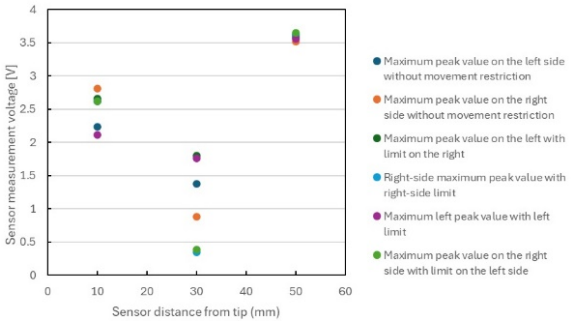

Fig. 20. Relationship between sensor position and maximum peak value.

4.5.2. Examining State Discrimination by Rate of Change of Sensor Values

Figs. 21 through 23 show examples of the rate of change of sensor values obtained at the six locations. Fig. 21 shows an example of a recording of a normal walk. Fig. 22 shows an example recording with the left leg restricted. Fig. 23 shows an example recording with the right leg restricted. This section describes the lines in the figures in Figs. 21-23. The blue line in the illustration indicates the heel, the purple line indicates the top of the toe, the red line indicates the toe, the green line indicates the bottom of the toe, the yellow line indicates the inside of the foot, and the yellow-green line indicates the outside of the foot.

Fig. 21 is compared to Fig. 22 and Fig. 23. In Fig. 22, the left toe bottom (green in the figure) and right toe inside (yellow in the figure) were not synchronized in the unrestricted condition. In Fig. 23, near-synchronous movement between the right toe-bottom and right inside was evident. Although the sample size was is small, we observed a tendency for the toes and insides of the restricted foot to be misaligned in their timing of landing on the ground.

4.5.3. Analysis with Toe Top Data

Using the analysis results of the previous section, the toe data were converted to toe-top data (referred to as toe-top in the figure) and analyzed using a random

forest with the rate of change of the sensor. The results are presented in Fig. 24.

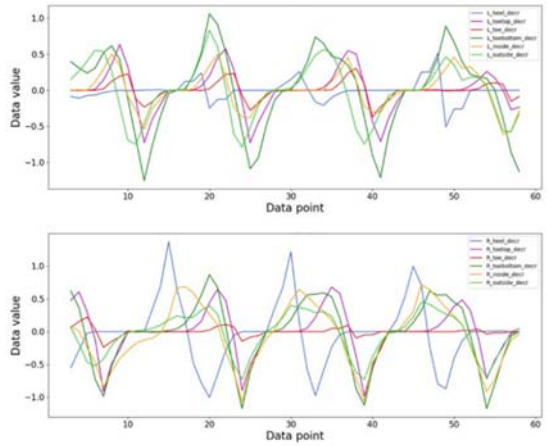

Fig. 21. Percentage change variation of left and right loads for unrestricted measurements (top: left foot, bottom: right foot).

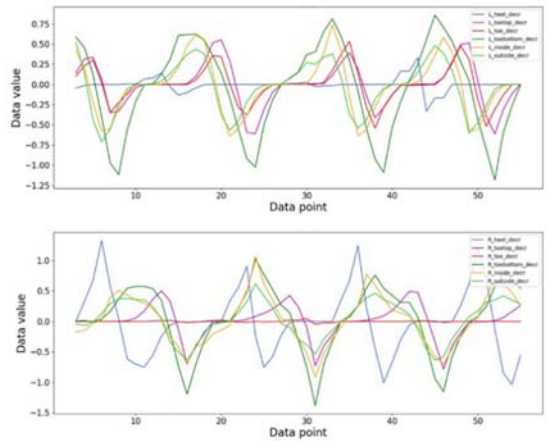

Fig. 22. Variation in rate of change of left and right loads with restriction on the left foot (top: left foot, bottom: right foot).

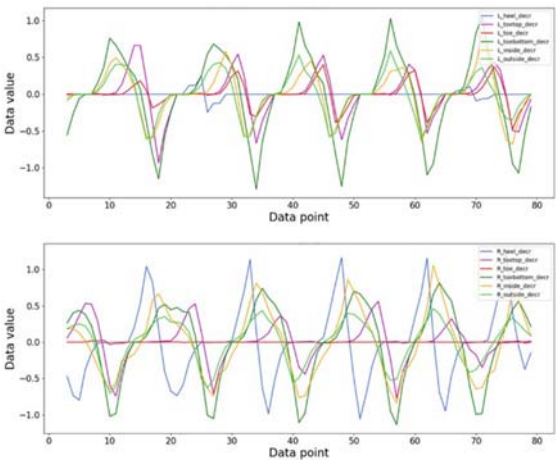

Fig. 23. Variation in rate of change of left and right loads with restriction on the right foot. (top: left foot, bottom: right foot).

Fig. 24 shows the results in order of increasing values: right toe top-G(RttG), left heel-G(LhG), left toe top-G(LttG), right heel-G(RhG), left outside-G(LoG), right inside-G(RiG), right outside-G(RoG), left inside-G(LiG), and right outside-G(RoG), and left inside-G(LiG). Regardless of the restricted foot, the toe and heel component values were high on both feet. The analysis results of the sensor peak values are shown in Fig. 25.

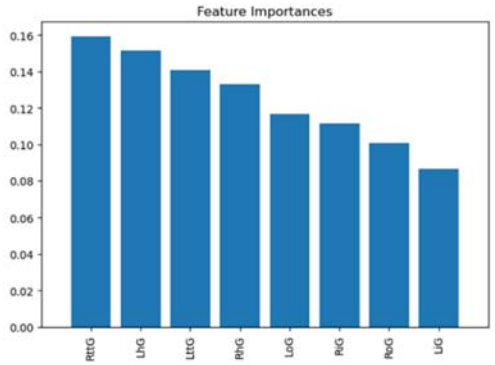

Fig. 24. Results of analysis of sensor change rate.

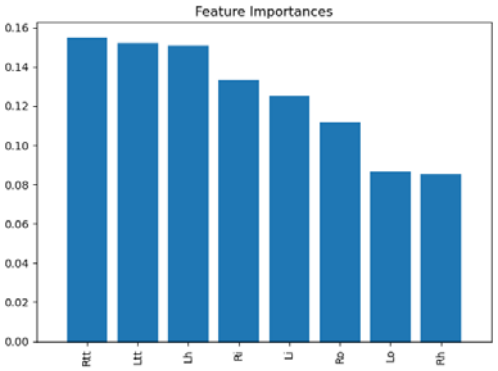

Fig. 25. Analysis results of sensor peak values.

Fig. 25 shows, in order of increasing value, right toe top (Rtt), left toe top (Ltt), left heel (Lh), right inside (Ri), left inside (Li), right outside (Ro), left outside (Lo), right heel (Rh). The top two toe component values for both feet were notably high.

The toe-top component values were judged to be higher than those of the conventional toe from Figs. 29 and 30, suggesting that the toe-top data were useful for discrimination.

4.5.4. Principal Component Analysis by Rate of Change

Principal component analysis was performed based on the results of the random forest analysis described in the previous section. The results of the principal component analysis using sensor change rates are shown in Figs. 26 to 29.

Fig. 26 shows that the first principal component was focused on the right toe (RttG), and the second principal component was focused on the left heel (LhG).

Elements 1-8 are the same as those in Fig. 24. The top four elements in Fig. 27 have cumulative contribution ratios exceeding 0.9, which indicates that the toe and heel factors are significant.

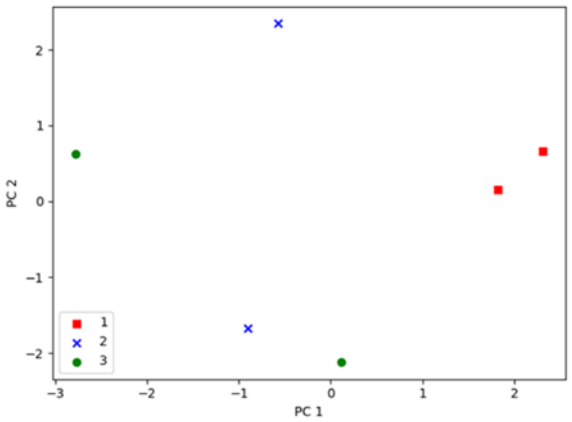

Fig. 26. Contribution of observables using sensor change ratio.

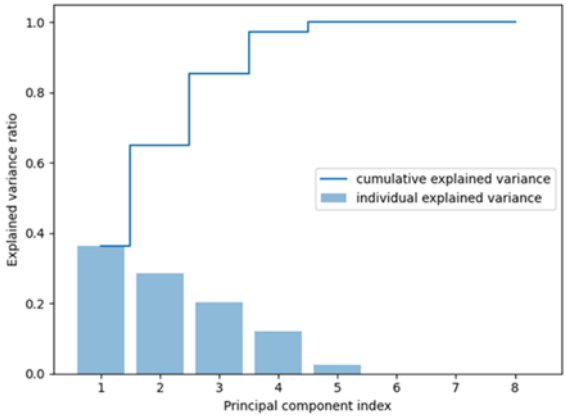

Fig. 27. Contribution and cumulative contribution ratio using sensor rate of change.

Fig. 28 shows the results of the principal component analysis on the supervised data. Although there were some errors, we can see that the three-factor classification was been implemented. Fig. 29 shows the results of classification using the test data. It can be observed that elements 2 and 3 were erroneous, but element 1 was successfully classified.

4.5.5. Principal Component Analysis by Peak Values

Similarly, Figs. 30-33 show the results of the principal component analysis using the peak value data. Elements 1-8 are the same as those shown in Fig. 25.

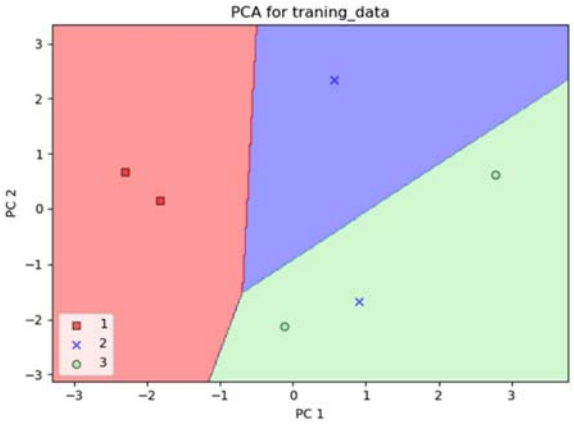

Fig. 28. Classification results using supervised data with sensor change rate.

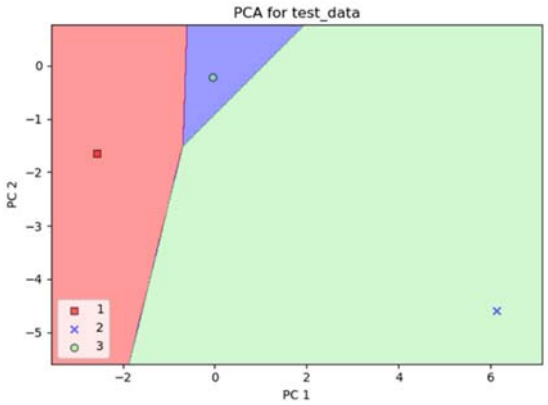

Fig. 29. Classification results based on test data using sensor change rate.

In Fig. 30 shows that the first principal component is focused on the left heel (Lh), and the second principal component is focused on the right toe (Rtt).

Fig. 31, the cumulative contribution ratio exceeds 0.8 for the top three factors, indicating that the toe and heel factors are significant.

Fig. 32 shows the results of the principal component analysis on the supervised data. Although there were some errors, it is evident that the three-factor classification was implemented.

Fig. 33 shows the results of classification using the test data. It can be observed that the classification of the three elements was performed without error.

5. Conclusion

Simultaneous measurement of both feet is now possible using this improved system.

From the acquired data, it is now possible to perform an analysis using features based on the data from both feet. For example, differences in gait state were observed by comparing external measurement data. By obtaining and analyzing the rate of change and peak values from the acquired data, we investigated the possibility of extending the analysis

to machine learning. The results of the analysis using random forest revealed that the toe sensor output was small in this measurement, as shown in the waveform in Fig. 5. We believe that the sensor value has a significant impact on the results of the peak value analysis. It was necessary to investigate whether the toe sensor position was optimal. From the comparison of the data used in the analysis, it appears that the rate of change captures the change during walking, even though the value is small compared to the peak value. This suggests that analysis by the rate of change may lead to the analysis of more detailed information compared to peak values. The results of the first measurement at one location indicated that the toe sensor data might be useful. We then analyzed the data using an insole with additional toe measurement points and demonstrated the possibility of classification by principal component analysis using data from the tip of the toe and between the toes. Although the data presented in this study were from two subjects, the possibility of discriminating between the subjects was found. This finding may lead to an accurate analysis of subject's gait characteristics.

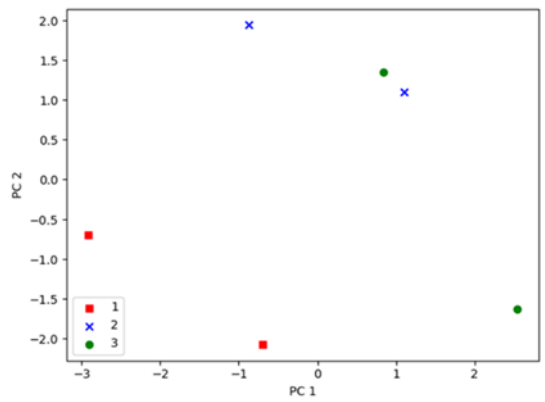

Fig. 30. Contribution of observables using peak values.

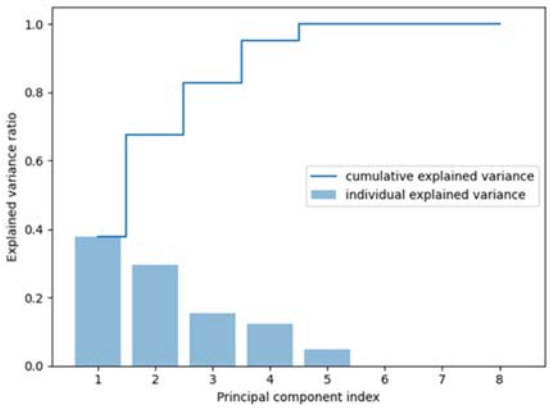

Fig. 31. Contribution ratio and cumulative contribution ratio using peak values.

In this study, we demonstrated the usefulness of insoles that can record detailed toe data tailored to each subject. Further study of the analysis method may enable the classification of the subject's gait condition and provide guidelines for measurement locations according to the subject's symptoms.

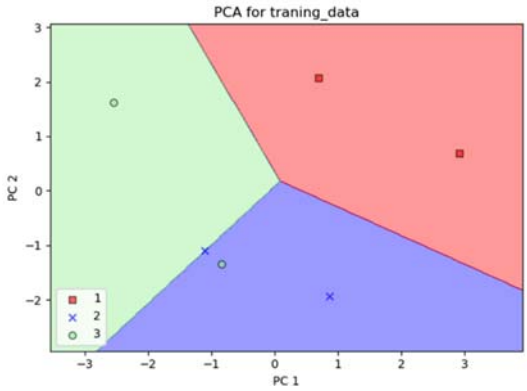

Fig. 32. Classification results with supervised data using peak values.

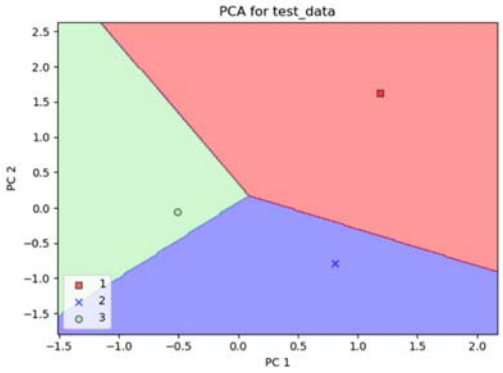

Fig. 33. Classification results from test data using peak values.

Acknowledgements

This study was supported by JSPS KAKENHI, Grant Numbers JP20K11924 and JP23K11207.

References

[1]. T. Kohro, Y. Furui, N. Mitsutake, R. Fujii, H. Morita, S. Oku, K. Ohe, R. Nagai, The Japanese national health screening and intervention program aimed at preventing worsening of the metabolic syndrome, *International Heart Journal*, Vol. 49, Issue 2, 2008, pp. 193-203.

[2]. M. Tago, N. E. Katsuki, S. Yaita, et al., High inter-rater reliability of Japanese bedriddenness ranks and cognitive function scores: a hospital-based prospective observational study, *BMC Geriatr.*, Vol. 21, 2021, 168.

[3]. B. Gunaydin, et.al., Multifractal detrended fluctuation analysis of insole pressure sensor data to diagnose vestibular system disorders, *Biomedical Engineering Letters*, Vol. 13, 2023, pp. 637-448.

[4]. M. Plotnik, N. Giladi, J. M. Hausdorff, Bilateral coordination of walking and freezing of gait in Parkinson's disease, *European Journal of Neuroscience*, Vol. 27, 2008, pp. 1999-2006,
[5]. J. M. Hausdorff, J. D. Schaafsma, Y. Balash, A. L. Bartels, T. Gurevich, N. Giladi, Impaired regulation of stride variability in Parkinson's disease subjects with freezing of gait, *Experimental Brain Research*, Vol. 149, 2003, pp. 187-194.
[6]. 3D motion capture system "VICON", https://www.vicon.com/
[7]. Tekscan Pressure Sensitive Mats, https://www.tekscan.com/versatile-pressure-sensing-mats
[8]. A. Kammoun, P. Ravier, O. Buttelli, Comparison of the accuracy of ground reaction force component estimation between supervised machine learning and deep learning methods using pressure insoles, *Sensors*, Vol. 24, Issue 16, 2024, 5318.
[9]. Toyoda Gosei, Feelsole, https://www.toyodagosei-led.jp/en/feelsole/
[10]. Moticon OpenGO, https://moticon.com/opengo/sensor-insole-sizes
[11]. Y. Uchida, T. Funayama, E. Ohkubo, Y. Kogure, Feature value classification based on the position difference of pressure sensors installed in insoles and their outputs, *Sensors & Transducers*, Vol. 263, Issue 4, 2023, pp. 12-20.
[12]. T. Funayama, Y. Uchida, Y. Kogure, D. Souma, R. Kimura, Exploring the assessment of steps using insoles with four-part pressure sensors, *Sensors & Transducers*, Vol. 263, Issue 4, 2023, pp. 21-28.
[13]. E. Ohkubo, Y. Uchida, T. Funayama, Y. Kogure, Prototype of bilateral gait measurement system and its initial analysis, in *Proceedings of the 10th International Conference on Sensors and Electronic Instrumentation Advances (SEIA'2024)*, Spain, 25-27 September 2024, pp. 39-43.
[14]. Interlink FSR-402, https://www.interlinkelectronics.com/fsr-402
[15]. Scikit-learn Project, https://scikit-learn.org/stable/

Sensors & Transducers, Vol. 267, Issue 4, December 2024, pp. 20-33

www.sensorsportal.com

Sensors & Transducers

Published by IFSA Publishing, S. L., 2024
http://www.sensorsportal.com

Land Use / Land Cover Change Classification and Measurement in the Middle Rio Grande Region, USA – Mexico Using Remote Sensing and Geographic Information Systems

[1, *] Omar BELHAJ, [2] Stanley MUBAKO, [1] Craig TWEEDIE, [1] Raed ALDOURI, [3] Elhadi HADIA, [1] William HARGROVE and [1] Alex MAYER

[1] University of Texas at El Paso, 500 West University Avenue, 79968, El Paso, Texas, USA
[2] California Department of Water Resources 715 P St., 6th Floor, Sacramento, CA 95814 C: 916-873-4784
Libyan Center for Sustainable Development Research, Khoms, Libya
[1] Tel.: 9152749938
E-mail: obelhaj@miners.utep.edu

Received: 10 June 2024 / Revised: 21 November 2024 / Accepted: 5 December 2024
Published: 30 December 2024

Abstract: Development and its expansion in dryland environments are experiencing climate warming and land-use/land cover change, impacting ecosystems and their sustainability and resiliency. Remote sensing (RS) and Geographic Information Systems (GIS) technologies provide opportunities to analyze land use/ landcover (LULC) change trends at local to regional scales over the past few decades. This study applied RS and GIS techniques to identify and measure land-use/ land-cover change in the Middle Rio Grande River Basin. A novel classification process is applied to assess land use and land-cover change between 1994 and 2015 in the Middle Rio Grande Region (MRGR) on the US- Mexico border, between San Antonio, New Mexico and Presidio, Texas, and Ojinaga, Chihuahua, which includes the cities of El Paso, Texas, Ciudad Juárez, Chihuahua, and Las Cruces, New Mexico. Results show that the native land cover has declined and is being replaced by urban development and agricultural expansion. Metropolitan areas across the region increased by 45 % from ~1.59 percent of the total study area in 1994 to more than 2.9 percent in 2015. The majority of expansion occurred around the major metropolitan areas of El Paso, Ciudad Juárez, and Las Cruces. Other land-use changes included a decrease in agricultural land cover and a loss of wetlands, possibly as a result of a reduction in streamflow. Possible impacts of these land-use/ land-cover changes on water resources include a shortage of water allocations for agriculture and ecosystems and the transfer of some water allocations to city land developers, as Hargrove et al. [1] demonstrated. Metropolitan planners, farmers, and other stakeholders will likely find the study valuable for planning water conservation measures, preparing for future water supply and treatment infrastructure growth, and monitoring groundwater availability and quality as urban populations grow.

Keywords: Development, Sustainability, Resiliency, Infrastructure, Land use, Land cover.

1. Introduction

Land resources encounter severe challenges worldwide, especially in arid and semi-arid regions, which occupy about one-third of the global land [2, 3]. Landcover degradation, soil erosion, water depletion, and ecosystem deterioration are some land resource changes [4-13]. A range of change drivers influences

land resource changes at different space and time scales, such as population growth, human activities, and climate change. These drivers put massive pressure on land resources and create uncertainty in these resources 'availability, long-term sustainability, and resiliency [14-18].

Land use and land cover (LULC) are two terms used separately to describe the earth's surface features and human interactions with these [19-25]. While land use states how humans have used the land, land cover indicates the biophysical characteristics of the earth's surface [19, 21-24, 26, 27]. The LULC change is possibly the most significant challenge to land resources and sometimes the most rapid in many places [28-31]. The LULC change carried various consequences on local, regional, and global scales. Amongst the intensive consequences of the LULC change is the extinction of native species when land use is changed from a comparatively undisturbed state to more intensive uses such as farming, livestock grazing, and selective tree harvesting [28, 29, 32-35]. The LULC changes result from the interaction of a wide variety of factors like human activities, agriculture, deforestation, animal grazing, and urbanization [32, 35-40]. Also, many indirect factors, such as technological, political, economic, cultural, demographic, and social factors, cause land use/ land cover change [36, 32, 37, 41]. Extensive data on the Earth's surface is required to monitor and analyze land use/land cover changes. Earlier, this information was created worldwide, mostly by conventional land recognition methods such as field surveys and on-site human-made observations, which required time, cost, and effort [42-44].

Modern LULC change studies typically use remotely sensed imagery, which provides excellent data sources from which information about LULC can be extracted and analyzed with various techniques and data sets [15, 30, 45-47]. Chang et al. [48] and Mubako et al. [49] demonstrated that remote sensing data and geographic information systems are valuable transboundary information sources and can be used to implement proficient cross-border studies. Remote sensing and geographic information technologies can help stakeholders map where changes occur, understand development patterns and seasonal land changes over time, and assess current activities and policies. They can also help expect and plan for future changes. Zhang et al. [9] demonstrated that medium spatial resolution imagery such as Landsat images are still the most significant data sources for urban land-cover classification, especially considering the free availability of this imagery, suitable spectral resolutions, and swath extent.

The Middle Rio Grande Region (MRGR) is a dryland ecosystem situated in the southwestern US-Mexico borderlands (50-52]. This region covers the area from southern New Mexico to far west Texas in the US and northern Chihuahua in Mexico. This region encompasses the three fast-growing cities of Las Cruces, New Mexico, El Paso, Texas, and Ciudad Juarez, Chihuahua, and is populated by more than two million people [49, 53]. The Rio Grande region faces enormous challenges with its resources, which significantly pressure these resource uses because of competition between stakeholders in areas such as agriculture, livestock raising, municipalities, industry, and wildlife [54, 49]. The Rio Grande River is the fourth largest river in North America and runs through the region from north to south. This river starts as a snow-fed stream high in the San Juan Luis Valley in southern Colorado and ends in the Gulf of Mexico. The Rio Grande River comprises the main surface water reservoirs in southern New Mexico, the Elephant Butte Reservoir and Caballo Reservoir. The Rio Grande River is one of the most significant water sources in southern New Mexico, far west Texas in the US, and northern Chihuahua in Mexico. It provides intensive agriculture practices for their irrigation needs. It also supplies the human communities and the ecosystems throughout the basin with their water needs [51, 55-58].

This MRGR contains various land use/ land cover features and practices and experiences massive changes over time due to disruptive human activities and natural conditions [57]. Urbanization is one of the region's most influential contributors to land use/ land cover change. It continues to grow, especially near the urban centers of Las Cruces, New Mexico, El Paso, Texas, and Juárez, Mexico [55]. A study conducted by Mubako et al. [49] on 4288 km^2 (1655 sq. miles) in the MRGR that included most areas of the three main cities in the region (Las Cruces, El Paso, and Ciudad Juarez) stated that the urban areas grew about 8 % in this area of interest in the 25 years 1990-2015 by taking important areas from agricultural lands and other vegetation. The agricultural lands and other vegetation areas decreased by about 11 % in this period.

The central aim of this study is to identify and measure LULC change in the MRGR. The study uses Landsat-based remote sensing and land cover classification to measure changes in the land use practices and land cover features in this region for 21 years from 1994 to 2015 (Fig. 1).

2. Data and Methodology

2.1. Study Area

This study's selected area of interest lies along the US – Mexico border. It includes the Middle Rio Grande basin from Magdalena and San Antonio, New Mexico, in the north to the entrance of the Rio Conchos from Mexico in the south. The area of interest is located between north latitudes 34.06000000 and 29.38166667 and west longitudes 107.85694444 and 104.21555556 (Fig. 1). The total study area is ~36,988 km^2 (14281 sq. miles) and includes six water sub-basins. The study area consists of different terrain features. This region covers the area from southern New Mexico to far west Texas in the US and the northern Mexican state of Chihuahua.

The region encompasses the three fast-growing cities of Las Cruces, New Mexico; El Paso, Texas; and Ciudad Juarez, Chihuahua, with a population of more than two million [18, 49].

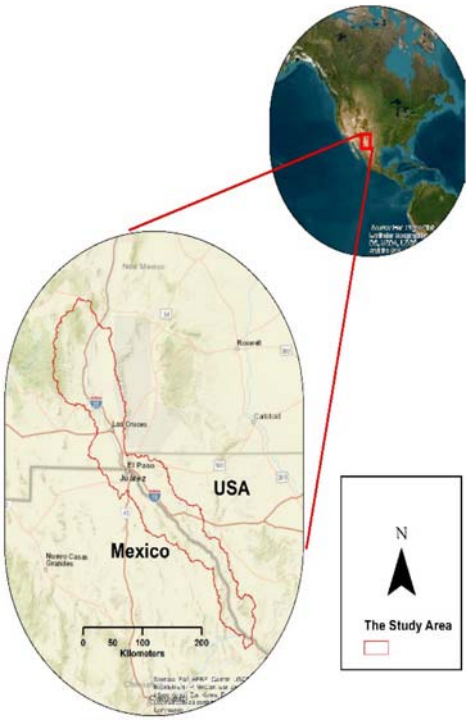

Fig. 1. The Study Area.

2.2. Materials and Methods

The following workflow is shown in Fig. 2 reflects the remote sensing and geographic information system procedures applied in this study to perform the work and get the best results.

The processes started with downloading and preparing Landsat data. Atmospheric data correction is applied, imagery is clipped to the extent of the study area, and minimum noise fraction transforming is completed to reduce the inherent spectral dimensionality and noise within multispectral data. After data preparation processes had been accomplished, image classification was performed using several applications and tools. The classification was performed using ArcGIS 10.8.1, ArcGIS Online, ENVI 5.4, Microsoft Excel, and Google Earth Professional.

2.2.1. Landsat Data Preparation

Eight multispectral Landsat scenes cover the study area shown in Fig. 1. (Path/Row): 031/039, 031/040, 032/038, 032/039, 033/037, 033/038, 034/036, and 034/037. As shown in Fig. 1 these images were downloaded from the U.S. Geological Survey (USGS) GloVis website (http://GloVis.usgs.gov/) for 1994, 2000, 2005, 2010, and 2015. Each scene had less than 10 percent cloud cover. The scenes used for the study area were chosen from Landsat 5 Thematic Mapper (TM) and Landsat 8 Operational Land Imager (OLI), as shown in Appendix (1). In fact, Landsat 5 Thematic Mapper (TM) and Landsat 8 Operational Land Imager (OLI) collect data with a spatial resolution of 30 meters in the visible, near-IR, and SWIR wavelength regions [59]. The scenes were acquired between the second half of May and the first week of July, considered the "leaf-on" season in this area [18, 49, 60-62]. Substantial procedures were performed on the scenes to prepare them for classification, including mosaicking the eight scenes in one image and clipping a final image to the study area boundaries.

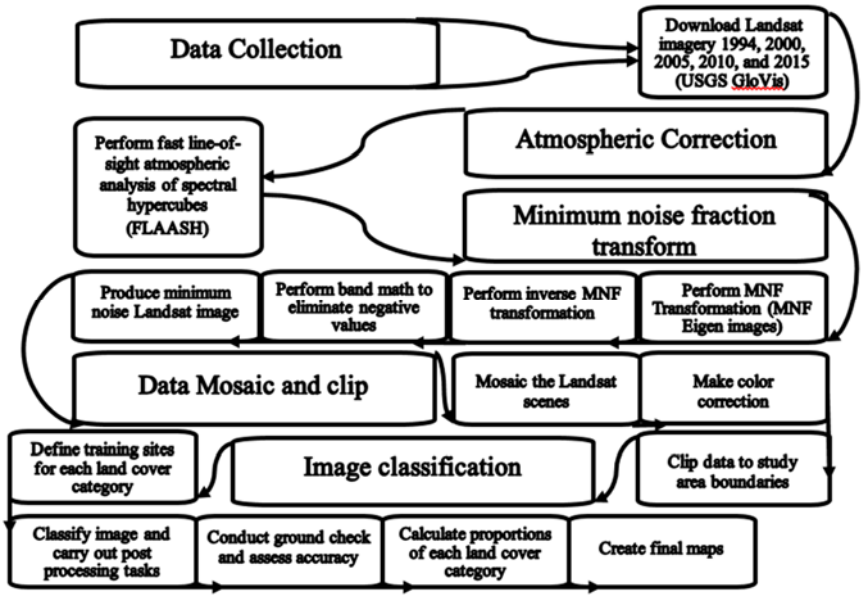

Fig. 2. The flowchart shows the RS&GIS proposed methods used in the study.

2.2.2. Atmospheric Correction

Kumar et al. [63] tested log residuals, flat field correction, IARR (Internal average relative reflectance), QUAC (Quick atmospheric correction), and FLAASH (Fast Line-of-Sight Atmospheric Analysis of Spectral Hypercubes) atmospheric correction methods. The results showed that FLAASH is the most efficient atmospheric correction method compared to the other methods.

Chakouri et al. [64] tested two physical atmospheric corrections, FLAASH and ATCOR (Atmospheric & Topographic Correction), compared to the DOS (Dark Object Subtraction) image-based method. The researchers found that the FLAASH provided the most accurate Bottom of Atmosphere BOA reflectance estimation.

Mruthyunjaya et al. [65] applied ATCOR and FLAASH atmospheric correction modules. The FLAASH provided the most accurate Bottom of Atmosphere BOA reflectance estimation. They found that the variation in aerosol optical depth AOD using the FLAASH method did not impact the identification of bare soil pixels coverage, which corresponded to 82.4 % of the study area, while a variation in water vapor using the ATCOR method provided a variation of bare soil pixels coverage from 75.04 to 84.04 %. They recommend using the FLAASH AC method to provide BOA reflectance values from Earth Observing-1 Hyperion Hyperspectral data before soil organic carbon mapping while using the ATCOR module needs careful selection of water vapor parameter before applying the method.

Therefore, we have chosen the FLAASH method to perform the atmospheric corrections. Specific steps were implemented in the ENVI 5.4 application for the five years chosen for the study. These steps included radiometric calibration to determine reflectance at the top of the atmosphere, fast line-of-sight atmospheric analysis of spectral hypercubes (FLAASH) for water vapor, and moisture correction to determine surface reflectance.

2.2.3. Minimum Noise Fraction Transform

To reduce the number of bands for processing hyperspectral remote sensing data and to improve processing efficiency, a minimum noise fraction (MNF) linear transformation process was used to transform the study area images for all analysis years [66-68]. This technique, widely applied in remote sensing, is implemented in ENVI 5.4 software [67] and reduces the inherent spectral dimensionality and noise within multispectral data. The final minimum noise fraction Landsat images were approved for classification based on both eigenvalue plots of the ground objects and visual inspection of the images.

2.2.4. Combined Classification

A newly developed object-based classification method was tested in combination with a pixel-based classification method [69, 70]. The object-based method has been shown to have greater accuracy and produce a more robust classification than the pixel-based method when using high-resolution imagery [71-76]. Object-based techniques create an image object via image segmentation and classify the images according to objects rather than pixels [77]. However, it has been shown that pixel-based land cover classification may sometimes outperform the classification accuracy results for specific land cover categories [77, 78]. Combining both methods produces optimal results [70].

The combined classification method comprises many steps that start with supervised or unsupervised classification and infiltrate the results based on the homogeneity of surface features to segment and attain the boundaries of surface features into more authentic products [75, 77] This study adopted such a generalized approach and started by implementing a supervised classification utilizing a maximum likelihood format [79-83]. Supervised classification uses the spectral information contained in individual pixels to generate land cover classes. The method requires the collection of training samples created in the study area, which are then used to derive spectral signatures of pixels in an image. It requires, therefore, prior knowledge of LULC types in the study area. Pixel signatures are generated and stored in signature files, and each pixel's digital numbers (DN) are converted to radiance values [49, 84, 85]. The interactive supervised classification module used to classify the minimum noise images is found in ArcGIS 10.8.1 software. The module was applied for the five years of analysis, 1994, 2000, 2005, 2010, and 2015, using the six broad land use categories defined in Table 1. Spectral signatures of the training samples were first analyzed using statistical methods.

According to Gao and Liu [86], a satisfactory spectral signature minimizes confusion between different land-use categories that need to be mapped. The whole region of interest was classified by assigning each image pixel to the training sample category of the match's highest probability. On average, 150 training samples were created for each land use category using the Landsat 1994_TM imagery since this was the year with the least developed land. A minimum of 500 pixels for each training sample category was used.

After producing the preliminary classified maps, field visits were made to designated features and places in the study area to find similarities and differences between the classified features on maps and their actual appearance and locations on the ground. Coordinates and information about the visited locations were collected. Other inquiry points were assigned to places familiar to our team. They were checked through high-resolution images downloaded for New Mexico and Texas states from their websites and used historical image visualization in Google Earth Professional. The chosen points were matched with the classified maps, and the misclasses were assigned to be recognized at the ultimate classification

step. Reclassification procedures were processed to correct the misclassified sites depending on the object-based features of these sites shown on the high-resolution images. Therefore, final classified maps that carried more accurate results have been created. These procedures were applied to the five maps created in the study: 1994, 2000, 2005, 2010, and 2015.

Table 1. Description of Land use/ Land cover classification categories used in the study.

Land use / Land cover	Description
Agriculture	Cultivated crops, trees, plants, and pastures
Developed Open space	Sports fields and courts, parks, picnic areas, and building yards
Developed area	Urban development constructions, buildings, concrete, and roads
Water	Open waterbodies in natural and human-made surface waterbodies
Evergreen Forest	Green trees on mountains and hills in the study area
Shrubs	Barren land, mountains, grass, and scrub/shrub features in the area

2.2.5. Finalizing Classification Mapping

Finalizing classifications of remotely sensed imagery is a balance between achieving outstanding quality classified final maps and the potential loss of essential map details through the unnecessary use of generalization tools [49, 87]. Therefore, the majority filter procedure was not applied to protect the isolated and small regions in the reclassified maps, which are real features in the study area. In addition, a boundary-cleaning filter was applied to these maps to smooth the boundaries and improve their layout. These steps were done through a series of geoprocessing tools in the Spatial Analyst Extension of ArcGIS 10.8.1.

2.2.6. Accuracy Assessment

The validity of classifications was confirmed by calculating multiple metrics indicative of the mapped accuracy of the classification. Classification accuracy was performed for individual land use categories and the total classification by creating a confusion matrix [29, 45, 49]. Six statistics were calculated: (1) overall accuracy, which represents the proportion of all correct classifications; (2) Kappa coefficient, a measure of the agreement of accuracy in classification assessment; (3) user accuracy, which calculates the probability that a classified pixel is correct on the ground; (4) producer accuracy, which is the probability that a pixel of a particular land-use type is assigned the correct land use category; (5) omission error, which represents specific categories that were omitted when they exist on the ground; and (6) commission error, which represents categories that were identified as existing on the ground when in fact they do not [45, 49].

3. Results and Discussion

3.1. Land Use / Land Cover Measurement and Change Trends

After producing the final classified maps, the areas of individual classes were calculated for the study area. This process was executed through the feature attributes related module in ArcGIS 10.8.1 for the five sample years. The final results are given in Table 2 and Fig. 3.

Table 2. Land use / land cover change 1994-2015.

Year	Land use / land cover category area (km^2)					
	Agriculture	Developed open space	Developed area	Water	Evergreen forest	Shrubs
1994	1245	29	589	241	1663	33221
2000	1190	33	768	185	1749	33063
2005	1125	36	933	122	2126	32646
2010	1111	40	1022	135	2155	32525
2015	1091	40	1078	106	1148	33825

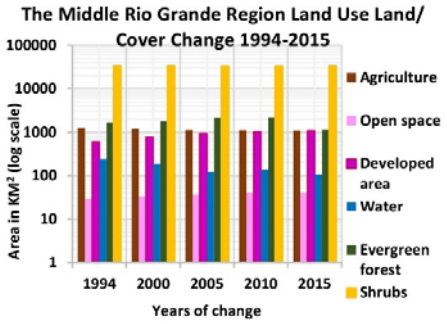

Fig. 3. The Middle Rio Grande Region LULC change 1994-2015.

The results showed many changes in the study area's land use/ land cover classes. Agriculture lands decreased from 1245 km^2 (3.37 percent) of the total study area in 1994 to 1091 km^2 (2.97 percent) in 2015. This is attributed mainly to the intensification of developing activities and the reduction of cultivation practices related to water use, and a shift from cotton and alfalfa production, with some production of chili peppers, vegetables, vineyards, and orchard crops to more profitable crops such as pecans for the analysis period [1]. The open space areas, including parks, sports fields and courses, and green areas, in cities and considered human-friendly development increased

following the urban growth from 29 km^2 (0.08 percent) in 1994 to 40 km^2 (0.11 percent) in 2015. The proportion of developed areas, including urban areas and other types of construction within the study area, increased over time from 589 km^2 (1.59 percent) in 1994 to 1078 km^2 (2.94 percent) in 2015. The increase happened primarily around the central three urban cities of cities El Paso (Texas, USA), Las Cruces (New Mexico, USA), and Ciudad Juárez (Chihuahua, Mexico). However, many along the Middle Rio Grande Region scattered minor cities, towns, communities, and neighborhoods, contributing to the urban expansion through the growth of urbanization in these cities, towns, communities, and neighborhoods.

The areal extent of surface water decreased from 241 km^2 (0.65 percent) in 1994 to 122 km^2 (0.33 percent) in 2005. Surface water increased in 2010 to 135 km^2 (0.36 percent). In contrast, surface water decreased to 106 km^2 (0.29 percent) in 2015, a total decrease of the surface water area of over 56 percent for the 21 years 1994-2015. Elephant Butte and Caballo's large reservoirs comprised the majority of the surface water extent and were located in the northern part of the study area. They are also considered the primary source of surface water in the southern part of the region.

Evergreen forest cover is restricted to some marginal zones in the region and almost in the northern part of the Magdalena Mountains, San Mateo Mountains, and Black Range. The areas of evergreen forests increased from 1663 km^2 (4.5 percent) in 1994 to 2155 km^2 (5.83 percent) of the total area in 2010. However, these areas decreased to 1148 km^2 (3.1 percent) in 2015 due to fires that burned significant parts of these forests. Records indicated several fires, the largest silver fire in 2013, which burned about 138,705 acres in the Black Range, New Mexico. Also, the San Mateo Mountains fire in 2015 burned 17,843 acres [88, 89]. Shrublands covers were the most dominant land cover in the study area for each of the time periods studied. The shrublands class lost important lands in many parts across the region. The results showed that shrublands covered 33221 km^2 (89.82 percent) in 1994 and shrunk to 32525 km^2 (78.93 percent) in 2010. This component gained some areas to 33225 km^2 (90.56 percent) in 2015 due to forest fires and surface water area reduction. The changes in LULC 1994-2015 are shown in Figs. 4-8.

3.2. Results Validation

3.2.1. Accuracy Assessment

For the study area, five maps were classified for 1994, 2000, 2005, 2010, and 2015. An accuracy assessment was applied using several extension tools in ArcGIS 10.8.1 to validate the classification results, focusing on analysis years 2005, 2010, and 2015. We got their high-resolution images these three years from Texas and New Mexico. 2005, 2010, and 2015 images support in-ground checks of classification results. Also, field visits were made to New Mexico and Texas areas to support the ground check of classification results. However, Google Earth was used in the ground check in Mexico, the part that I could not check in the field because of the restrictions on border movement. The classification quality is oriented in a confusion matrix that is widely used to present accuracy assessment information in remote sensing [49, 88]. About 520 points were used for each classified map (year). A stratified random sampling method was applied for validation. The method assigned sampling points according to the proportion area of each class in the study area. An overall accuracy of 99 percent was obtained in 2005, 2010, and 2015. Subjectivity in interpreting classification results, fuzzy boundaries between land use categories, and uncertainty in the supervised classification algorithm in assigning land use categories to mixed pixels are all possible sources of intrinsic uncertainty and error that could have been propagated in this type of study. Calculating the Kappa statistics, which account for classification agreements owing to chance, is an alternative approach to measuring classification accuracy. The Kappa coefficient was 0.96 for three years, statistically supporting the classification's overall accuracy. For all land use/ land cover categories, the producer accuracy ranged from 88.2 percent to 100 percent for the three years, and user accuracy went from 90 to 100 percent. Detailed assessment results are presented in Tables 3, 4, and 5.

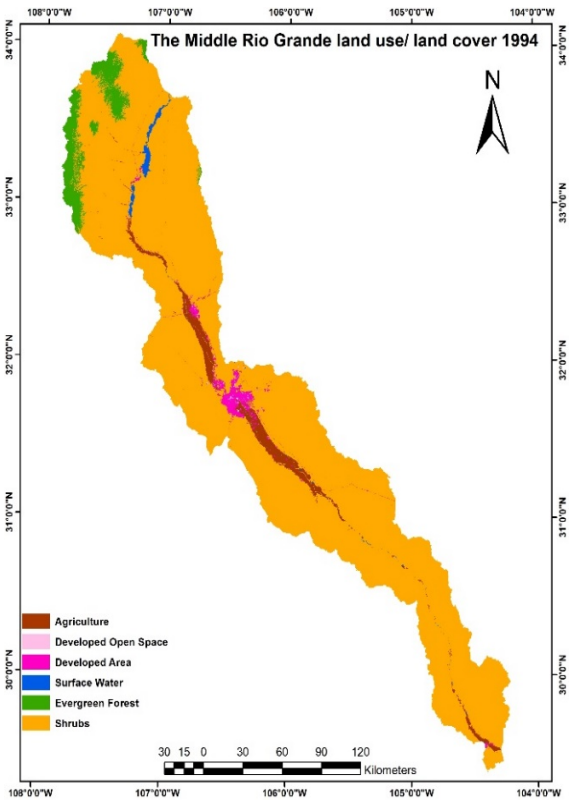

Fig. 4. The Middle Rio Grande Region LULC 1994.

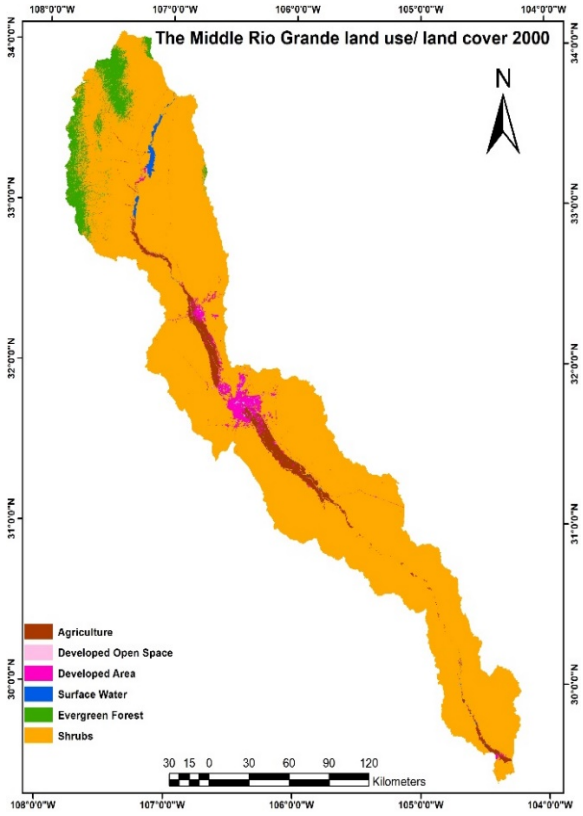

Fig. 5. The Middle Rio Grande Region LULC 2000.

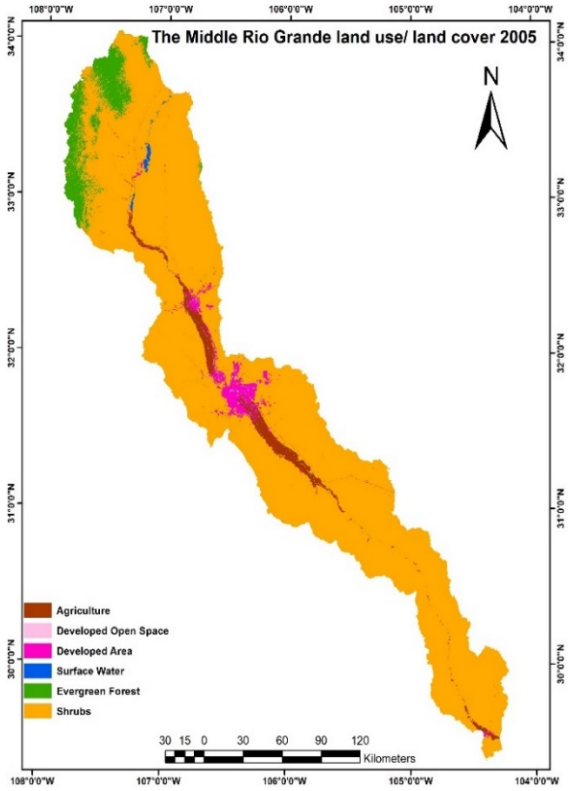

Fig. 6. The Middle Rio Grande LULC 2005.

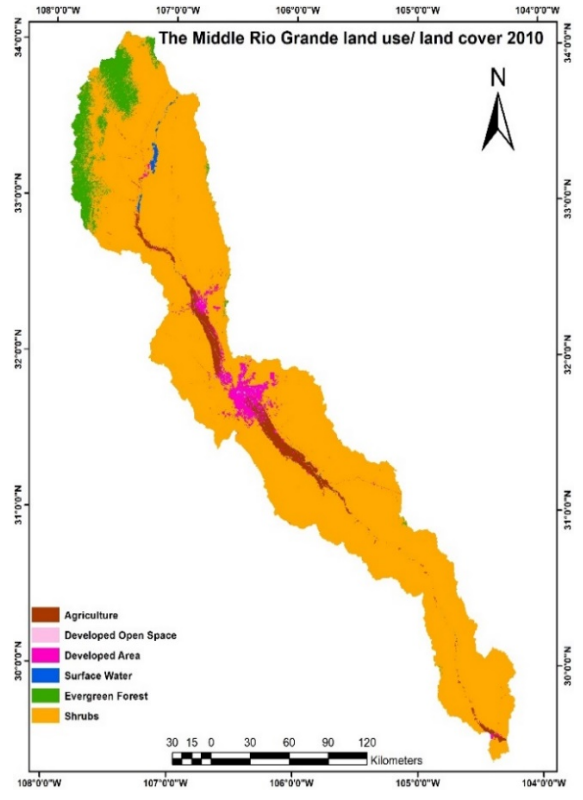

Fig. 7. The Middle Rio Grande LULC 2010.

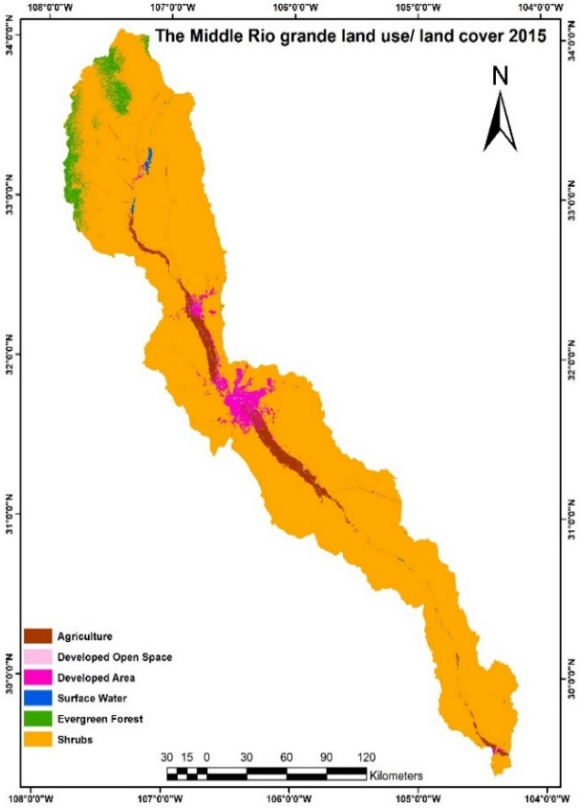

Fig. 8. The Middle Rio Grande LULC 2015.

Table 3. Confusion matrix showing classification accuracy for the 2005 map.

Classified	Ground truth								
	Agriculture	Open space	Developed area	Water	Evergreen Forest	Shrubs	Total ground	User's accuracy %	The error of commission %
Agriculture	14	0	0	0	0	1	15	93.33	6.67
Open space	0	10	0	0	0	0	10	100	0
Developed area	1	0	12	0	0	0	13	92.31	7.69
Water	0	0	0	10	0	0	10	100	0
Evergreen Forest	0	0	0	0	26	3	29	89.66	10.34
Shrubs	0	0	0	0	1	440	441	99.77	0.23
Total classified	15	10	12	10	27	444	518		
Producer accuracy %	93.33	100	100	100	96.30	99.1			
The error of omission %	6.67	0	0	0	3.70	0.90			
Overall accuracy %	98.84								
Kappa coefficient	0.96								

Table 4. Confusion matrix showing classification accuracy for the 2010 map.

Classified	Ground truth								
	Agriculture	Open space	Developed area	Water	Evergreen Forest	Shrubs	Total ground	User's accuracy %	The error of commission %
Agriculture	15	0	0	0	0	1	16	93.75	6.25
Open space	0	9	0	0	0	0	9	100	0
Developed area	0	0	14	0	0	0	14	100	0
Water	0	0	0	10	0	0	10	100	0
Evergreen Forest	0	0	0	0	29	3	32	90.625	9.375
Shrubs	0	1	0	0	0	436	437	99.77	0.23
Total classified	15	10	14	10	29	440	518		
Producer accuracy %	100	90	100	100	100	99.09			
The error of omission %	0	10	0	0	0	0.91			
Overall accuracy %	99								
Kappa coefficient	0.96								

Table 5. Confusion matrix showing classification accuracy for the 2015 map.

Classified	Ground truth								
	Agriculture	Open space	Developed area	Water	Evergreen Forest	Shrubs	Total ground	User's accuracy %	The error of commission %
Agriculture	15	0	0	0	0	0	15	100	0
Open space	0	10	0	0	0	0	10	100	0
Developed area	0	0	14	0	0	1	15	93.33	6.67
Water	0	0	0	10	0	0	10	100	0
Evergreen Forest	0	0	0	0	15	1	16	93.75	6.25
Shrubs	0	0	1	0	2	451	454	99.34	0.66
Total classified	15	10	15	10	17	453	520		
Producer accuracy %	100	100	93.33	100	88.24	99.56			
The error of omission %	0	0	6.67	0	11.76	0.44			
Overall accuracy %	99								
Kappa coefficient	0.96								

As Mubako et al. [49] mentioned, overall classification accuracy and accuracy for all classes greater than 75-85 percent is acceptable. That accuracy assessment compromises the ideal and the affordable [18, 49]. Wickham et al. [89] recommended an acceptable overall classification accuracy between 84-85 percent for most satellite data classification studies to evaluate the National Standard Land Cover Database (NLCD) classification system. The coarse 30 m spatial resolution of the Landsat images utilized in the study also contributed to classification errors. Two or even more spectral classes were frequently recorded inside one pixel using this low-resolution data, which obviously influenced classification accuracy. Errors were experienced when performing the accuracy assessment with some pixels for some classes. Therefore, our results classification errors are partly due to impure training samples that captured mixed land use categories. Accurate reference data is essential for testing classification accuracy [90]. Therefore, accuracy errors were calculated as part of the assessment. The results showed that commissions' errors were not over 10 % for some classes, and the errors of omissions were not over 12 % for some individual classes.

3.4. Discussion

The US-Mexico border Middle Rio Grande Region is dryland covering ~36988 km^2 (14281 sq miles). We studied this region to measure land use/ land cover and find their changes for 21 years (1994-2015) by using remote sensing and geographic information systems. The study divided the period into five years: 1994, 2000, 2005, 2010, and 2015.

The results showed significant changes in land use / land cover features during the study period 1994-2015. The open space areas increased by about 27 percent. The developed area across the area of interest increased by 45 percent in 21 years between 1994-2015 by winning important extents from agricultural and shrublands, and the most growth occurred around the metropolitan areas of El Paso (Texas, USA), Las Cruces (New Mexico, USA), and Ciudad Juárez (Chihuahua, Mexico). The shrublands increased by about 1 percent. On the other hand, the agricultural land decreased by about 12 percent. Surface water decreased by more than 55 percent in this period. The evergreen forests decreased by about 30 percent.

The study results presented that the MRGR, like other drylands, faces serious challenges, such as water reduction and competitive demand growth amongst sectors such as agriculture and domestic use. Shrubs and native plants are disturbed naturally during climate change, such as temperature increases, and human activities, such as urbanization growth and construction expansion. However, there are similarities and differences in changes between the MRGR and the other drylands. The effect of the change on the area depends on the location and management of this area. A study in the Kathmandu Valley, Nepal, for the period 1989-2016 showed similarities in LULC changes with the MRGR. The results showed that urban areas expanded up to 412 % in the last three decades, and most of this expansion occurred with the conversions of 31 % of agricultural land. The majority of the urban expansion happened during 1989–2009, and it is still growing along the major roads in a concentric pattern, significantly altering the cityscape of the valley [91]. Another study in the Zayandehrood ecologic sub-basins of Central Iran Asia also showed similarities in LULC changes with the MRGR. The results revealed that from 1985 to 2016, residential areas doubled, and industrial areas increased at the expense of rangelands. The study also revealed cropland expansion at the expense of rangelands, cropland abandonment, and contraction of croplands due to residential and industrial development [92]. Also, a study focused on Palapye, a predominantly dryland agricultural region in eastern Botswana, Africa, aimed to analyze LULC change and divided the period into two intervals (1986-2000, 2000-2014). This study showed similarities in LULC changes with the MRGR. The results showed that cropland was a vibrant losing category in the first time interval, while it was a clear gaining category during the second time interval. Cropland expanded into shrublands in the southwestern part of the study area. The built-up category was active in gains during the second time interval as it targeted grasslands and shrublands [93]. On the other hand, and through good management, a study in Karoo drylands, South Africa, revealed that more than 95 **%** of the Karoo is comprised of land classified as Natural, which has been relatively stable since 1990. An analysis of repeat photographs shows that vegetation cover has either remained unchanged or has increased at most locations. However, the Karoo drylands appear less degraded than they were in the mid-twentieth century [94].

LULC changes in the MRGR have many implications for the region. Reducing snowpack in the headwaters of the Rio Grande River causes a growing water supply deficit and failure to sustain the competing demands of different sectors even though these demands for surface water stay the same in aggregate [1]. It increases the pressure on the reservoirs of surface water used as a water source for various uses. For example, this appears clearly in the Elephant Butte Reservoir, the primary surface water source in the MRGR. Its capacity since 2011 fluctuated between 3-25 % of the total capacity [95, 96]. Rising soil and water salinity and growing constraints on using these resources for agricultural production, drinking, and various environmental needs. Relying on the growth of groundwater to provide the necessary water supplies for various uses and the pressure and negative impacts on this limited to nonrenewable water resource also face many serious problems, such as depletion and quality deterioration [1]. The loss of grasslands, shrublands, and forests to urban development can lead to the loss

of natural habitats and ecological diversity, a higher risk of flooding due to increased surface runoff in paved urban areas, and increased water pollution from point and non-point sources, such as new industries waste facilities. When considering outdoor recreation, the loss of natural landscapes may decrease tourism income associated with water-dependent natural ecosystems [49].

This change in LULC raises some critical questions that need an answer, such as what is the extent of LULC change in this region? What is the change limit for cities such as El Paso and Ciudad Juarez? How does this change affect sustainability and the region's future? Do we need to stop this change, control it, or adapt to the new situation? What are the implications of the change?

3.5. Conclusion

Remote sensing and geographic information systems technologies across boundary tools for cooperation and research were used to visualize, measure, and assess LULC change in the MRGR, a dryland environment in the USA and Mexico borderlands. This region faces significant natural consequences associated with LULC change from one type to another, especially in relation to sustainable water management.

The results from the study showed many changes in LULC. For instance, the developed area across the area of interest increased by 45 percent in 21 years between 1994-2015, and the most growth occurred around the metropolitan areas of cities El Paso (Texas, USA), Las Cruces (New Mexico, USA), and Ciudad Juárez (Chihuahua, Mexico). Surface water decreased by more than 55 percent in the period 1994-2015. The dominant shrublands in the area of interest have changed and have lost areas and parts to the urban and agriculture and gained others from forests and a reduction in surface water cover.

This study's findings stand as an excellent view for visualizing and understanding spatial and temporal environmental change in this region and helping stakeholders on different levels and responsibilities to balance development requirements and protect dynamic ecosystems.

Future research is recommended on monitoring LULC change in the region on a macro scale that can cover the cities and the local areas to understand the effect of development on natural resources such as shrublands and forests. Conservation of environmental flows by controlling human actions that disrupt the resources. This study provides a detailed assessment of the driving forces behind the trends and patterns of LULC change.

The study's results reveal the requirement to change land use policies to include guidelines and regulations that can help maintain the resources, such as restricting water consumption and changing agriculture practices towards less water use produce.

Abbreviations and Acronyms

SR: Remote Sensing;
GIS: Geographic Information Systems;
LULC: Land Use / Land Cover;
MRGR: Middle Rio Grande Region;
FLAASH: Fast Line-of-Sight Atmospheric Analysis of Spectral Hypercubes;
BOA: Bottom of Atmosphere;
NLCD: National Standard Land Cover Data Base;
USGS: U.S. Geological Survey;
TM: Thematic Mapper;
OLI: Operational Land Imager;
IARR: Internal Average Relative Reflectance;
QUAC: Quick Atmospheric Correction;
ATCOR: Atmospheric and Topographic Correction;
DOS: Dark Object Subtract;
MNF: Minimum Noise Fraction;
DN: Digital Numbers.

Acknowledgments

This study was made possible through support from the National Institute of Food and Agriculture, U.S. Department of Agriculture, under award number 2015-68007-23130. The opinions in this paper are those of the authors and do not necessarily reflect the USDA's views. The authors would like to acknowledge valuable comments and inputs from various collaborators on the USDA-NIFA project.

References

[1]. W. Hargrove, J. Heyman, A comprehensive process for stakeholder identification and engagement in addressing wicked water resources problems, *Land*, Vol. 9, Issue 4, 2020, 119.

[2]. K. Liu, X. Li, S. Wang, G. Zhou, Past and the future adverse response of terrestrial water storages to increased vegetation growth in drylands, *npj Climate and Atmospheric Science*, Vol. 6, Issue 1, 2023, 113.

[3]. A. M. El Kenawy, Hydroclimatic extremes in arid and semi-arid regions: status, challenges, and future outlook, in Hydroclimatic Extremes in the Middle East and North Africa, *Elsevier*, 2024, pp. 1-22.

[4]. P. H. Verburg, K. Neumann, L. Nol, Challenges in using land use and land cover data for global change studies, *Global Change Biology*, Vol. 17, Issue 2, 2011, pp. 974-989.

[5]. K. Biro, B. Pradhan, M. Buchroithner, F. Makeschin, Land use/land cover change analysis and its impact on soil properties in the northern part of Gadarif region, Sudan, *Land Degradation & Development*, Vol. 24, Issue 1, 2013, pp. 90-102.

[6]. N. N. Omoyo, J. Wakhungu, S. Oteng'i, Effects of climate variability on maize yield in the arid and semi-arid lands of lower eastern Kenya, *Agriculture & Food Security*, Vol. 4, Issue 1, 2015, 8.

[7]. J. Heo, J. Yu, J. R. Giardino, H. Cho, Water resources response to climate and land-cover changes in a semi-arid watershed, New Mexico, USA, TAO:

Terrestrial, *Atmospheric and Oceanic Sciences*, Vol. 26, Issue 4, 2015, 463.
[8]. L. Zhu, H. Gong, Z. Dai, T. Xu, X. Su, An integrated assessment of the impact of precipitation and groundwater on vegetation growth in arid and semiarid areas, *Environmental Earth Sciences*, Vol. 74, Issue 6, 2015, pp. 5009-5021.
[9]. C. Zhang, Y. Chen, D. Lu, detecting fractional land-cover change in arid and semiarid urban landscapes with multitemporal Landsat Thematic mapper imagery, *GIScience & Remote Sensing*, Vol. 52, Issue 6, 2015, pp. 700-722.
[10]. J. Yin, F. He, Y. J. Xiong, G. Y. Qiu, Effects of land use/land cover and climate changes on surface runoff in a semi-humid and semi-arid transition zone in Northwest China, *Hydrology and Earth System Sciences*, Vol. 21, Issue 1, 2017, pp. 183-196.
[11]. C. R. Randklev, T. Miller, M. Hart, J. Morton, N. A. Johnson, K. Skow, C. Robertson, A semi-arid river in distress: Contributing factors and recovery solutions for three imperiled freshwater mussels (Family Unionidae) endemic to the Rio Grande basin in North America, *Science of the Total Environment*, Vol. 631, 2018, pp. 733-744.
[12]. M. A. Abdel Rahman, An overview of land degradation, desertification and sustainable land management using GIS and remote sensing applications, *Rendiconti Lincei, Scienze Fisiche e Naturali*, Vol. 34, Issue 3, 2023, pp. 767-808.
[13]. N. Liliwirianis, N. N. M. Isa, M. N. Suratman, Land resources and its degradation in Asia: its control and management, in Land and Environmental Management through Forestry, *Wiley*, 2023, pp. 23-45.
[14]. A. O. Arowolo, A. K. Bhowmik, W. Qi, X. Deng, Comparison of spatial interpolation techniques to generate high□resolution climate surfaces for Nigeria, *International Journal of Climatology*, Vol. 37, 2017, pp. 179-192.
[15]. A. Halefom, A. Teshome, E. Sisay, I. Ahmad, Dynamics of land use and land cover change using remote sensing and GIS: a case study of Debre Tabor Town, South Gondar, Ethiopia, *Journal of Geographic Information System*, Vol. 10, Issue 02, 2018, 165.
[16]. M. A. Boggie, D. P. Collins, J. P. Donnelly, S. A. Carleton, Land use, anthropogenic disturbance, and riverine features drive patterns of habitat selection by a wintering waterbird in a semi-arid environment, *PloS One*, Vol. 13, Issue 11, 2018.
[17]. Q. Shen, Y. Ma, Did water diversion projects lead to sustainable ecological restoration in arid endorheic basins? lessons from long-term changes of multiple ecosystem indicators in the Lower Heihe River Basin, *Science of The Total Environment*, Vol. 701, 2020, 134785.
[18]. O. S. Belhaj, Land use/land cover change patterns and trends in two dryland regions, PhD Thesis, *The University of Texas at El Paso*, 2022.
[19]. C. Liping, S. Yujun, S. Saeed, Monitoring and predicting land use and land cover changes using remote sensing and GIS techniques – A case study of a hilly area, Jiangle, China, *PloS One*, Vol. 13, Issue 7, 2018.
[20]. O. Stromann, A. Nascetti, O. Yousif, Y. Ban, Dimensionality reduction and feature selection for object-based land cover classification based on Sentinel-1 and Sentinel-2 time series using Google Earth Engine, *Remote Sensing*, Vol. 12, Issue 1, 2020, 76.
[21]. S. Merdas, N. Boulghobra, T. Mostephaoui, M. Belhamra, H. Fadlaoui, Assessing land use change and moving sand transport in the Western Hodna Basin (central Algerian steppe ecosystems), *Forestist*, Vol. 69, Issue 2, 2019, pp. 87-96.
[22]. V. R. Rajeswari, S. N. Reddy, Change detection analysis using landsat multi-temporal imagery and GIS techniques: a case study for Tirupati, South India, *Journal on Image Processing*, Vol. 6, Issue 2, 2019, 34.
[23]. J. Sun, S. Ongsomwang, Multitemporal land use and land cover classification from time-series landsat datasets using harmonic analysis with a minimum spectral distance algorithm, *ISPRS International Journal of Geo-Information*, Vol. 9, Issue 2, 2020, 67.
[24]. M. Dagnachew, A. Kebede, A. Moges, A. Abebe, Land use land cover changes and its drivers in Gojeb river catchment, Omo Gibe Basin, Ethiopia, *Journal of Agriculture and Environment for International Development (JAEID)*, Vol. 114, Issue 1, 2020, pp. 33-56.
[25]. R. Pacheco Quevedo, A. Velastegui-Montoya, N. Montalván-Burbano, F Morante-Carballo, O. Korup, C. Daleles Rennó, Land use and land cover as a conditioning factor in landslide susceptibility: a literature review, *Landslides*, Vol. 20, Issue 5, 2023, pp. 967-982.
[26]. P. H. Verburg, K. Neumann, L. Nol, Challenges in using land use and land cover data for global change studies, *Global Change Biology*, Vol. 17, Issue 2, 2011, pp. 974-989.
[27]. W. Tesfaye, E. Elias, B. Warkineh, M. Tekalign, G. Abebe, Modeling of land use and land cover changes using Google Earth engine and machine learning approach: implications for landscape management, *Environmental Systems Research*, Vol. 13, Issue 1, 2024, 31.
[28]. A. C. Guzha, M. C. Rufino, S. Okoth, S. Jacobs, R. L. B. Nóbrega, Impacts of land use and land cover change on surface runoff, discharge, and low flows: Evidence from East Africa, *Journal of Hydrology: Regional Studies*, Vol. 15, 2018, pp. 49-67.
[29]. K. Islam, M. Jashimuddin, B. Nath, T. K. Nath, Land use classification and change detection by using multi-temporal remotely sensed imagery: The case of Chunati wildlife sanctuary, Bangladesh, *The Egyptian Journal of Remote Sensing and Space Science*, Vol. 21, Issue 1, 2018, pp. 37-47.
[30]. O. S. Belhaj, S. T. Mubako, Land use land cover change and urban growth in Khoms District, Libya, 1976-2015, *International Journal of Applied Geospatial Research (IJAGR)*, Vol. 11, Issue 2, 2020, pp. 42-58.
[31]. S. Li, Y. Cao, J. Liu, S. Wang, Simulating land use change for sustainable land management in China's coal resource-based cities under different scenarios, *Science of The Total Environment*, Vol. 916, 2024, 170126.
[32]. A. O. Arowolo, A. K. Bhowmik, W. Qi, X. Deng, Comparison of spatial interpolation techniques to generate high-resolution climate surfaces for Nigeria, International Journal of Climatology, Vol. 37, 2017, pp. 179-192.
[33]. P. K. Langat, L. Kumar, R. Koech, M. K. Ghosh, Monitoring of land use/land-cover dynamics using remote sensing: a case of Tana River Basin, Kenya, *Geocarto International*, Vol. 36, Issue 13, 2019, pp. 1470-1488.

[34]. M. Fushimi, G. N. de Lima, V. Capoane, Changes in land use and cover and their environmental impacts in the Cerrado of Mato Grosso Do Sul, Brazil, *Sustainability*, Vol. 16, Issue 10, 2024, 4266.

[35]. B. T. Edosa, M. D. Nagasa, Spatiotemporal assessment of land use land cover change, driving forces, and consequences using geospatial techniques: The case of Naqamte city and hinterland, Western Ethiopia, *Environmental Challenges*, Vol. 14, 2024, 100830.

[36]. B. A. Miheretu, A. A. Yimer, Land use/land cover changes and their environmental implications in the Gelana sub-watershed of Northern Highlands of Ethiopia, *Environmental Systems Research*, Vol. 6, Issue 1, 2018, 7.

[37]. A. T. Testfaw, A. Pfaff, R. E. G. Kroner, S. Qin, R. Medeiros, M. B. Mascia, Land-use and land-cover change shape the sustainability and impacts of protected areas, *Proceedings of the National Academy of Sciences*, Vol. 115, Issue 9, 2018, pp. 2084-2089.

[38]. M. S. Khan, S. Ullah, T. Sun, A. U. Rehman, L. Chen, Land-use/land-cover changes and its contribution to urban heat island: a case study of Islamabad, Pakistan, *Sustainability*, Vol. 12, Issue 9, 2020, 3861.

[39]. Y. A. Bununu, A. Bello, A. Ahmed, Land cover, land use, climate change and food security, *Sustainable Earth Reviews*, Vol. 6, Issue 1, 2023, 16.

[40]. K. Ashwini, B. S. Sil, A. A. Kafy, H. A. Altuwaijri, H. Nath, Z. A. Rahaman, Harnessing machine learning algorithms to model the association between land use/land cover change and heatwave dynamics for enhanced environmental management, *Land*, Vol. 13, Issue 8, 2024, 1273.

[41]. B. Abbasnezhad, J. B. Abrams, S. J. Wenger, The Impact of Projected Land Use Changes on the availability of ecosystem services in the Upper Flint River Watershed, USA, *Land*, Vol. 13, Issue 6, 2024, 893.

[42]. P. C. Pandey, N. Koutsias, G. P. Petropoulos, P. K. Srivastava, E. Ben Dor, Land use/land cover in view of earth observation: data sources, input dimensions, and classifiers – a review of the state of the art, *Geocarto International*, Vol. 36, Issue 9, 2019, pp. 957-988.

[43]. O. Belhaj, S. Mubako, R. Aldouri, C. Tweedie, W. Hargeove, A. Mayer, E. Hadia, measuring land use/land cover change in the Middle Rio Grande Region, USA-Mexico using remote sensing and geographic information systems, *Sensors and Electronic Instrumentation Advances*, Vol. 162, 2024.

[44]. N. Abid, M. Eman, G. Kovács, F. Shafait, M. Liwicki, Multi-UCL: multi-class unsupervised curriculum learning for image scene classification case study: earth observation, *TechRxiv*, September 06, 2024.

[45]. A. Butt, R. Shabbir, S. S. Ahmad, N. Aziz, Land use change mapping and analysis using remote sensing and GIS: A case study of Simly watershed, Islamabad, Pakistan, *The Egyptian Journal of Remote Sensing and Space Science*, Vol. 18, Issue 2, 2015, pp. 251-259.

[46]. N. A. Kadhim, A. K. Hussein, A. S. Jaber, A. A. Abojassim, Land use and land cover change detection using satellite images for the Kufa District, Najaf, Iraq, *Journal of XI an University of Architecture & Technology*, Vol. 12, Issue 3, 2020, 3632.

[47]. G. A. Afuye, L. Nduku, A. M. Kalumba, C. A. G. Santos, I. R. Orimoloye, V. N. Ojeh, P. Sibandze, Global trend assessment of land use and land cover changes: A systematic approach to future research development and planning, *Journal of King Saud University-Science*, Vol. 36, Issue 7, 2024, 103262.

[48]. Y. Chang, K. Hou, X. Li, Y. Zhang, P. Chen, Review of land use and land cover change research progress, *IOP Conference Series: Earth and Environmental Science*, Vol. 113, Issue 1, 2018, 012087.

[49]. S. Mubako, O. Belhaj, J. Heyman, W. Hargrove, C. Reyes, Monitoring of land use/land-cover changes in the arid transboundary Middle Rio Grande Basin using remote sensing, *Remote Sensing*, Vol. 10, Issue 12, 2018, 2005.

[50]. F. A. Ward, J. F. Booker, A. M. Michelsen, Integrated economic, hydrologic, and institutional analysis of policy responses to mitigate drought impacts in Rio Grande Basin, *Journal of Water Resources Planning and Management*, Vol. 132, Issue 6, 2006, pp. 488-502.

[51]. Z. Sheng, Impacts of groundwater pumping and climate variability on groundwater availability in the Rio Grande Basin, *Ecosphere*, Vol. 4, Issue 1, 2013, 5.

[52]. O. Olofinsao, J. Wang, R. P. Berrens, Reuse of treated municipal wastewater in drylands: multi-sector optimization analysis for Middle Rio Grande case study, https://papers.ssrn.com/sol3/Delivery.cfm/4932099.pdf?abstractid=4932099&mirid=1

[53]. W. L. Hargrove, J. M. Heyman, A. Mayer, A. Mirchi, A. Granados-Olivas, G. Ganjegunte, D. Gutzler, The future of water in a desert river basin facing climate change and competing demands: A holistic approach to water sustainability in arid and semi-arid regions, *Journal of Hydrology: Regional Studies*, Vol. 46, 2023, 101336.

[54]. L. F. Nava, C. Brown, K. Demeter, F. Lasserre, M. Milanés-Murcia, S. Mumme, S. Sandoval-Solis, Existing opportunities to adapt the Rio Grande/Bravo Basin water resources allocation framework, *Water*, Vol. 8, Issue 7, 2016, 291.

[55]. A. Szynkiewicz, D. M. Borrok, G. K. Ganjegunte, G. Skrzypek, L. Ma, M. S. Rearick, G. B. Perkins, Isotopic studies of the Upper and Middle Rio Grande, Part 2 – Salt loads and human impacts in South New Mexico and West Texas, *Chemical Geology*, Vol. 411, 2015, pp. 336-350.

[56]. H. D. A. Sanchez, Determining sources of nitrate in the semi-arid Rio Grande using nitrogen and oxygen isotopes, MD Thesis, *University of Tennessee*, 2017.

[57]. C. R. Randklev, T. Miller, M. Hart, J. Morton, N. A. Johnson, K. Skow, C. Robertson, A semi-arid river in distress: Contributing factors and recovery solutions for three imperiled freshwater mussels (Family Unionidae) endemic to the Rio Grande basin in North America, *Science of the Total Environment*, Vol. 631, 2018, pp. 733-744.

[58]. C. Cox, L. Jin, G. Ganjegunte, D. Borrok, V. Lougheed, L. Ma, Soil quality changes due to flood irrigation in agricultural fields along the Rio Grande in western Texas, Applied Geochemistry, Vol. 90, 2018, pp. 87-100.

[59]. Landsat – Earth Observation Satellites, Ver. 1.2, April 2020, Fact Sheet, *U.S. Geological Survey*, 2016.

[60]. O. S. Belhaj, S. T. Mubako, R. E. Aldouri, C. E. Tweedie, W. L. Hargrove, E. A. Hadia, Determination of change in surface waterbodies in the middle Rio Grande basin by modified normalized difference water index (MNDWI) 1994-2020, *Journal of Eco. & Enviro. Sci. and Tech.*, Vol. 4, Issue 2, 2022, pp. 67-80.

[61]. D. G. Dye, B. R. Middleton, J. M. Vogel, Z. Wu, M. Velasco, Exploiting differential vegetation

Phenology for satellite-based mapping of semiarid grass vegetation in the Southwestern United States and Northern Mexico, *Remote Sensing*, Vol. 8, Issue 11, 2016, 889.

[62]. N. Aboagye, Twenty-five years (1995-2020) of land cover changes in the Northern Rio Grande Corridor, New Mexico, MD Thesis, *New Mexico State University*, 2024.

[63]. M. V. Kumar, K. Yarrakula, Comparison of efficient techniques of hyper-spectral image preprocessing for mineralogy and vegetation studies, *Indian Journal of Geo-Marine Sciences*, Vol. 46, 2017, May 2017, pp. 1008-1021.

[64]. M. Chakouri, R. Lhissou, A. El Harti, S. Maimouni, Z. Adiri, Assessment of the image-based atmospheric correction of multispectral satellite images for geological mapping in arid and semi-arid regions, *Remote Sensing Applications: Society and Environment*, Vol. 20, 2020, 100420.

[65]. P. Mruthyunjaya, A. Shetty, P. Umesh, C. Gomez, Impact of atmospheric correction methods parametrization on soil organic carbon estimation based on Hyperion hyperspectral data, *Remote Sensing*, Vol. 14, Issue 20, 2022, 5117.

[66]. L. K. Sharma, R. K. Verma, AVIRIS-NG hyperspectral data analysis for pre-and post-MNF transformation using per-pixel classification algorithms, *Geocarto International*, Vol. 37, Issue 7, 2022, pp. 2083-2094.

[67]. B. Liu, Y. Li, P. Chen, X. Zhu, Extraction of oil spill information using decision tree based minimum noise fraction transform, *Journal of the Indian Society of Remote Sensing*, Vol. 44, Issue 3, 2016, pp. 421-426.

[68]. H. Wang, G. Yu, J. Cheng, Z. Zhang, X. Wang, Y. Xu, Fast hyperspectral image classification with strong noise robustness based on minimum noise fraction, *Remote Sensing*, Vol. 16, Issue 20, 2024, 3782.

[69]. J. Aguirre-Gutiérrez, A. C. Seijmonsbergen, J. F. Duivenvoorden, optimizing land cover classification accuracy for change detection, a combined pixel-based and object-based approach in a mountainous area in Mexico, *Applied Geography*, Vol. 34, 2012, pp. 29-37.

[70]. Y. Chen, Y. N. Zhou, Y. Ge, R. An, Y. Chen, Enhancing land cover mapping through integration of pixel-based and object-based classifications from remotely sensed imagery, *Remote Sensing*, Vol. 10, Issue 1, 2018, 77.

[71]. C. Cleve, M. Kelly, F. R. Kearns, M. Moritz, Classification of the wildland-urban interface: A comparison of pixel-and object-based classifications using high-resolution aerial photography, *Computers, Environment and Urban Systems*, Vol. 32, Issue 4, 2008, pp. 317-326.

[72]. P. Corcoran, A. Winstanley, Using texture to tackle the scale problem in land-cover classification, in Object-Based Image Analysis, *Springer*, Berlin, Heidelberg, 2008, pp. 113-132.

[73]. F. Hájek, Process-based approach to automated classification of forest structures using medium format digital aerial photos and ancillary GIS information, *European Journal of Forest Research*, Vol. 127, Issue 2, 2008, pp. 115-124.

[74]. H. Costa, G. M. Foody, D. S. Boyd, Supervised methods of image segmentation accuracy assessment in land cover mapping, *Remote Sensing of Environment*, Vol. 205, 2018, pp. 338-351.

[75]. H. Lu, L. Ma, X. Fu, C. Liu, Z. Wang, M. Tang, N. Li, Landslides information extraction using object-oriented image analysis paradigm based on deep learning and transfer learning, *Remote Sensing*, Vol. 12, Issue 5, 2020, 752.

[76]. D. K. Behera, G. S. Pujar, R. Kumar, S. K. Singh, A comprehensive approach towards enhancing land use land cover classification through machine learning and object-based image analysis, *Journal of the Indian Society of Remote Sensing*, 2024.

[77]. G. Shivakanth, P. S. Tanwar, Review on conventional and advanced classification approaches in remote sensing image processing, *Int. J. Comput. Sci. Eng*., Vol. 6, 2018, pp. 871-879.

[78]. D. Flanders, M. Hall-Beyer, J. Pereverzoff, Preliminary evaluation of eCognition object-based software for cut block delineation and feature extraction. *Canadian Journal of Remote Sensing*, Vol. 29, Issue 4, 2003, pp. 441-452.

[79]. M. Gutierrez, E. Johnson, Temporal variations of natural soil salinity in an arid environment using satellite images, *Journal of South American Earth Sciences*, Vol. 30, Issue 1, 2010, pp. 46-57.

[80]. J. S. Rawat, V. Biswas, M. Kumar, Changes in land use/cover using geospatial techniques: A case study of Ramnagar town area, district Nainital, Uttarakhand, India, *The Egyptian Journal of Remote Sensing and Space Science*, Vol. 16, Issue 1, 2013, pp. 111-117.

[81]. C. E. Churches, P. J. Wampler, W. Sun, A. J. Smith, Evaluation of forest cover estimates for Haiti using supervised classification of Landsat data, *International Journal of Applied Earth Observation and Geoinformation*, Vol. 30, 2014, pp. 203-216.

[82]. M. S. Boori, V. Voženílek, K. Choudhary, Land use/cover disturbance due to tourism in Jeseníky Mountain, Czech Republic: A remote sensing and GIS-based approach, *The Egyptian Journal of Remote Sensing and Space Science*, Vol. 18, Issue 1, 2015, pp. 17-26.

[83]. J. S. Rawat, M. Kumar, Monitoring land use/cover change using remote sensing and GIS techniques: A case study of Hawalbagh block, District Almora, Uttarakhand, India, *The Egyptian Journal of Remote Sensing and Space Science*, Vol. 18, Issue 1, 2015, pp. 77-84.

[84]. J. R. Jensen, Introductory Digital Image Processing: A Remote Sensing Perspective, 2005, *Prentice-Hall Inc*., 2005.

[85]. J. B. Campbell, R. H. Wynne, Introduction to Remote Sensing, *Guilford Press*, 2011.

[86]. J. Gao, Y. Liu, Determination of land degradation causes in Tongyu County, Northeast China via land cover change detection, *International Journal of Applied Earth Observation and Geoinformation*, Vol. 12, Issue 1, 2010, pp. 9-16.

[87]. K. Keranen, R. Kolvoord, Making Spatial Decisions Using GIS and Remote Sensing: A Workbook, *Esri Press*, 2014.

[88]. US Forest Service, Red Canyon Fire, The Magdalena Ranger District, https://www.fs.usda.gov/ publications?forestgrassland=10230&publication_topic=All&topic=All&year=all

[89]. New Mexico Fire Information, The Magdalena Ganger District Fires. Silver Fire, San Mateo Mountains. https://nmfireinfo.com/

[90]. A. Tilahun, B. Teferie, Accuracy assessment of land use land cover classification using Google Earth, *American Journal of Environmental Protection*, Vol. 4, Issue 4, 2015, pp. 193-198.

[91]. J. D. Wickham, S. V. Stehman, L. Gass, J. Dewitz, J. A. Fry, T. G. Wade, Accuracy assessment of NLCD

2006 land cover and impervious surface, *Remote Sensing of Environment*, Vol. 130, 2013, pp. 294-304.
[92]. R. Martin, L. Brabyn, C. Beard, Effects of class granularity and cofactors on the performance of unsupervised classification of wetlands using multi-spectral aerial photography, *Journal of Spatial Science*, Vol. 59, Issue 2, 2014, pp. 269-282.
[93]. A. Ishtiaque, M. Shrestha, N. Chhetri, Rapid urban growth in the Kathmandu Valley, Nepal: Monitoring land use land cover dynamics of a Himalayan city with landsat imageries, *Environments*, Vol. 4, Issue 4, 2017, 72.
[94]. B. Mazloum, S. Pourmanafi, A. Soffianian, A. Salmanmahiny, A. V. Prishchepov, The fate of rangelands: Revealing past and predicting future land□cover transitions from 1985 to 2036 in the drylands of Central Iran, *Land Degradation & Development*, Vol. 32, Issue 14, 2021, pp. 4004-4017.
[95]. F. O. Akinyemi, G. Mashame, Analysis of land change in the dryland agricultural landscapes of eastern Botswana, *Land Use Policy*, Vol. 76, 2018, pp. 798-811.
[96]. M. Timm Hoffman, A. Skowno, W. Bell, S. Mashele, Long-term changes in land use, land cover and vegetation in the Karoo drylands of South Africa: implications for degradation monitoring, *African Journal of Range & Forage Science*, Vol. 35, Issues 3-4, 2018, pp. 209-221.
[97]. A. V. Vaisvil, Natal source and the influence of environmental stressors on the timing and persistence of largemouth bass reproduction in Elephant Butte Reservoir, PhD Thesis, *New Mexico State University*, 2019.
[98]. N. T. Townsend, Evaluating Future Reservoir Storage in the Rio Grande Using Normalized Climate Projections and A Water Balance Model, University of New Mexico UNM Digital Repository, Earth and Planetary Sciences ETDs, https://digitalrepository.unm.edu/eps_etds/259

Published by International Frequency Sensor Association (IFSA) Publishing, S. L., 2024 (http://www.sensorsportal.com).

Sensors & Transducers, Vol. 267, Issue 4, December 2024, pp. 34-48

www.sensorsportal.com

Sensors & Transducers

Published by IFSA Publishing, S. L., 2024
http://www.sensorsportal.com

Assessment of the Planar Low Power Discrete *npnp* Structure Radiation Hardness Under γ-irradiation Taking into Consideration Non-linear Change of the Holding Current Probability

Sergey BYTKIN
Department of Electronics, Information Systems and Software Development of Engineering Educational and Scientific Institute named after U. M. Potebnja of Zaporizhzhya National University, Zaporizhzhya, pr. Sobornyj, 226, Ukraine
Tel.: +38 (096)7128400
E-mail: sergey.bytkin@gmail.com

Received: 13 March 2024 / Revised: 10 November 2024 / Accepted: 11 December 2024
Published: 30 December 2024

Abstract: The radiation degradation of the npnp thyristor radiation-sensitive characteristic, holding current, $I_{holding}$, considered. As the dose of γ-irradiation (Φ_γ) increased, the distribution of the $I_{holding}$ shows pulsating change (quasi-periodicity) in quantity and amplitude of peaks (extremes) of $I_{holding}$ in a wide range of Φ_γ. The investigated thyristors samples show real radiation hardness only up to 200 mSv. At $200 \le \Phi_\gamma \le 1000$ mSv $I_{holding}$ ***S***-shape degradation was observed. From a practical point of view, using such a low-power discrete planar npnp thyristor in the range of $1000 \le \Phi_\gamma \le 7 \cdot 10^3$ mSv is advisable. For the range of approximately $6 \cdot 10^3 \le \Phi_\gamma \le 1 \cdot 10^5$ mSv it's difficult to forecast the value of the $I_{holding}$ (heavy risk zone). $\Phi_\gamma \ge 1 \cdot 10^5$ mSv may be considered a failure zone of the devices. The evaluation method was proposed for a realistic assessment of the radiation resistance of discrete devices. It includes the construction of approximating $I_{holding}$ dose dependence using results of experimental measurements and calculations to find laminar (smooth) and chaotic (jagged) phases of degradation. The laminar phase will show the ranges of real radiation hardness (no changes of the holding current) and predictable changes of device parameters under irradiation. The beginning of the chaotic phase indicates the end of the reliable npnp structure operation and the possibility of soon device failure. Obtained experimental results agree with previously received theoretical approaches of other authors.

Keywords: Low power npnp structure, γ-irradiation, Bimodal distribution, Probability, Radiation hardness, Heavy risk zone, Failure, Phases of the holding current degradation, Realistic assessment of the radiation resistance of discrete devices.

1. Introduction

A severe nuclear power plant (NPP) accident can release significant radiation from the reactor core [1]. For example, the Chornobyl disaster exposed a substantial fraction of core material to the environment. The exposed reactor created γ-radiation; the highest dose was about 300 Sv/h. Similarly, the Fukushima disaster also released many radioactive substances into the environment due to hydrogen explosions and fire damage to the containment structures. In Feb. 2017 the level of radiation was estimated to be up to 530 Sv/h. So, the design of radiation-hardening methodologies, as well as rad-hardened analysis techniques are not a luxury, but necessary, to ensure the reliable operation of the special equipment (post-accident monitoring systems (PAMs), mobile military robots) to work in harsh environmental conditions during decommissioning processes in the event of an accident. Approach, based on the rad-hardened components employed for special-purpose equipment manufacturing can be excessively expensive due to special semiconductor materials used, technology complexity in the production processes, and most of all, the small size of the market supporting such devices. Another approach is to rely on regular commercial off-the-shelf (COTS) devices with high vulnerability to radiation.

Experience in the use of "extreme robotics" in the external conditions of a radiation accident, for example, during cleaning of the destroyed reactor from highly radioactive elements, debris of the structure, fuel residues etc. (γ-background level up to ≈3000 Roentgen per hour (R/hour), in some places, radiation levels up to ≈10^4 R/hour), showed the possibility of decontamination using a mobile robot, on which all drives were made electromechanical [2]. Control systems were made on very humble relay elements. It is not possible for complicated intelligent robotic systems [3, 4]. Therefore, the radioactive shielding protection of the radiation-sensitive robot components is now considered the key technology of robot efficiency in severe radiation ambiance. Still, protecting the mobile platform and manipulator sufficiently increases the robot's weight, thus affecting its motion flexibility [5] near the destroyed reactor, creating the risk of lodging. Reducing the thickness of protection enhances robot survivability in hazardous radiation environments. For highly complex work, it is necessary to use solid-state relays (SSRs), because of various features that mechanical relays do not incorporate [6]. SSRs are immune to the shock and vibrations at levels, normally encountered [7]. This facility employs semiconductor switching elements, transferring the signals at high frequency. Most DC solid-state switching devices commonly use power transistors, whereas, for an AC SSR, the switching device is either a triac or back-to-back thyristors instead of the usual mechanical normally open contact relays [8]. Thyristors are preferred due to their high voltage and current capabilities. Theoretically, it is necessary to increase the radiation hardness of electronic components to complete the equipment to eliminate accidents at nuclear power stations with an element component base operating at γ-irradiation with an intensity of up to 10 R/s and an integral dose of up to 10^6R [9]. This is a technologically complex task [10]. The radiation-hardening methodology, Rad-Hard-By-Process (RHBP), employs modified manufacturing processes to improve their ability to withstand radiation. The cost of developing new RHBP became prohibitively expensive; as a result, there are no widely used industrial technologies [11]. That's why creating new approaches to radiation hardness improvement is stably relevant.

2. The Purpose of the Work

The evolution of the structure of radiation damage of the irradiated objects (and semiconductor devices, of course) is also accomplished, under certain stationary irradiation conditions radiation defects density self-organizing [12]. Many experimentally observed phenomena that correspond to self-organization, such as self-oscillations of conductivity, non-monotonous dose dependence of microhardness, non-monotonous dose dependence of creep, oscillations of the size of vacancy voids, etc. due to the probability of their sensitive characteristics changing to much higher or lower values than expected before irradiation.

Therefore, it is necessary to consider the possibility of self-oscillation, for example, of the thyristor characteristics for the secure operation of nuclear facilities. For the confident operation of discrete devices in a hazardous radiation environment, it is necessary to consider the possibility of the most thyristor radiation-sensitive characteristic – holding current ($I_{holding}$) – self-oscillation.

The possibility of applying theoretical concepts of self-organization in the analysis of experimental data obtained by irradiation of low-power npnp thyristors was proposed in [13]. Shown, that as the dose of γ-irradiation (Φ_γ) increased, the distribution of the $I_{holding}$ shows pulsating change (quasi-periodicity) in quantity and amplitude of peaks (extremes) of $I_{holding}$ in a wide range of Φ_γ. At the same time, this work did not investigate the dependence of the reproducibility of experimental results on the radiation dose, i.e. dispersion of $I_{holding}$. It is also necessary to describe the calculation methods that allow reflection the specific features of the thyristor degradation (laminar (smooth) and chaotic (jagged) phases).

Thus, the purpose of the present work was to receive details of the npnp structure $I_{holding}$ radiation degradation to find possible ties with radiation-induced self - organization processes.

3. Devices (*npnp* Structures), Method of Measurement

The description (vertical structure, package, geometric dimensions) of the used experimental low-power thyristors is given in [14].

Measurements were carried out by [15]. The isotope Americium-241 (the half-life 432.6 years) with the following main parameters: energy of γ-quanta E = 59.5 keV; photon flux density at a distance of 1 m from the center of the working surface $(7.0\pm2.1)\cdot10^4$ s^{-1} cm^{-2}; maximum activity of the source 2.24 Ku used as a source of γ-radiation [16].

4. Results of Experiment

4.1. Quasi-periodic Change in the Numerical Value of the Holding Current Probability of a Low-power npnp Thyristorunder γ-Irradiation

The results of the holding current measurements were analyzed using Statistica 10 [17]. The nonlinear relationship between Φ_γ and the number of peaks with different forms and amplitude was experimentally observed (Fig. 1). Formulas of used distribution density functions (e is the base of the natural logarithm (2.71), π is the constant Pi (3.14) are in the cells with

histograms in Fig. 1. It was discovered that as the dose of γ-irradiation increased, the distribution of the thyristor sample selection distribution modes, and the amplitude of the peaks of $I_{holding}$, did not change monotonically.

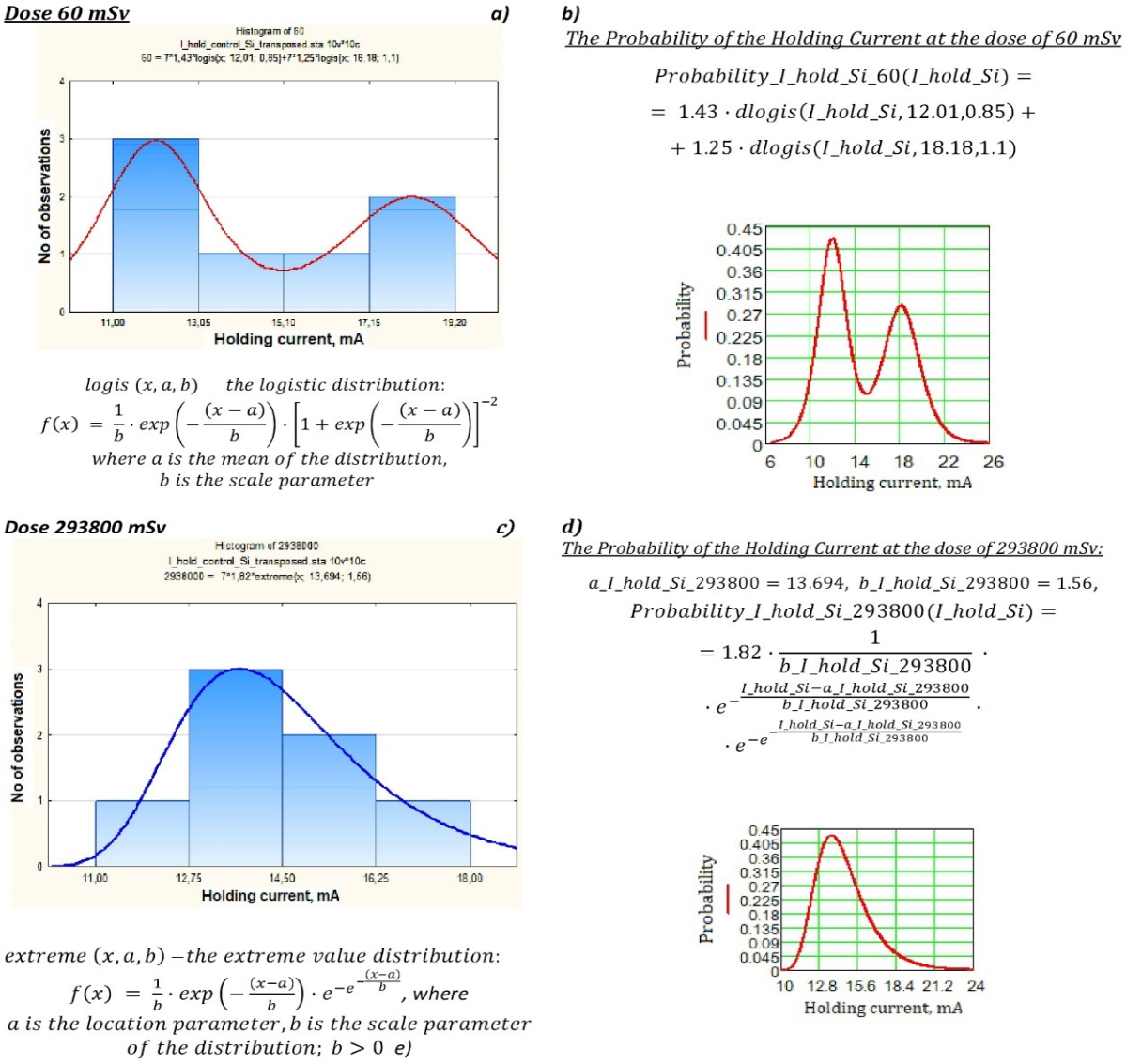

Fig. 1. Examples of the Distributions of Numerical Values of the Holding Current at Different γ-irradiation Doses.

With an increase in the radiation dose, there is a periodic increase/decrease in the probability of $I_{holding}$ in a wide range of numerical values, Fig. 2.

This phenomenon is characteristic of irradiation of solids [18] (including, in our opinion, npnp crystal structures of silicon discrete low-power thyristors), which in this case are the so-called open flow-type system. The energy flux of γ - irradiation, which does not dampen in a certain interval, maintains conditions in the irradiated sample far from thermal equilibrium. As a result of radiation exposure, the structure of the semiconductor material of the irradiated thyristor is disrupted due to the formation of radiation defects. As the radiation dose accumulates, the structure of radiation damage in Si becomes more complex. The phenomena occur due to various interrelated processes, among which it is often impossible to single out several dominant ones (the phenomenon of synergy). Mobile defects (vacancies, first of all) can form clusters (in particular, clusters of divacancies) and bind into electrically active complexes (A-, E-, K-centers) with impurity atoms. As a result, their spatially ordered concentration distribution (stratification) is formed, which depends on the radiation dose (which, in turn, depends on the exposure time).

Each accumulated radiation dose probably corresponds (to some extent) to an *individual* [14] distribution of impurity-defective complexes. At the same time, it is logical to assume that there is a quasi-periodic reproduction of the structure of the recombination regions of the npnp structure created by

radiation exposure. This partly causes a "pulsating" change in the probability of the numerical value of the thyristor holding current during irradiation.

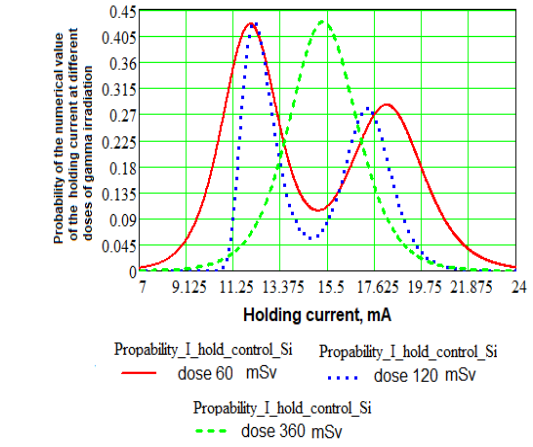

(a)

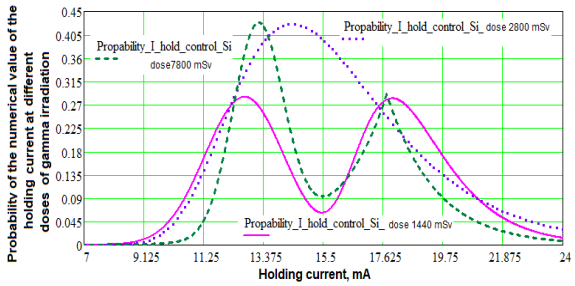

(b)

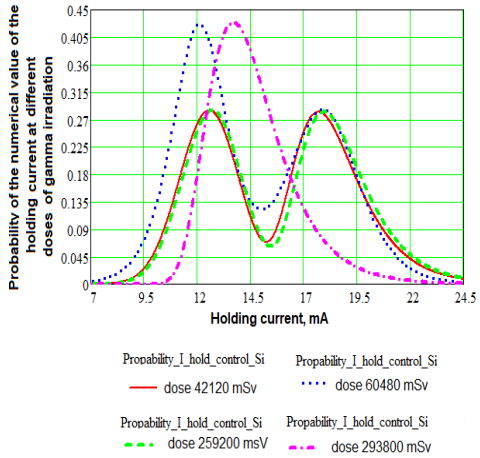

(c)

Fig. 2. Quasi-periodic change in the probability of the numerical value of the $I_{holding}$ under γ-irradiation.

So, the evolution (change) of the dependence of probability fluctuations of the $I_{holding}$ in a wide range of radiation doses can be considered a reflection of the self-organization of complexes of radiation defects.

In other words, at certain doses of γ-irradiation, the distribution of the $I_{holding}$ becomes more *homogeneous* (Fig. 2(a)) Φ_γ = 360 mSv; b) 2800 mSv; c) 293800 mSv); it may reflect the similar distribution of impurity-defective complexes in the irradiated Si single crystal on which the npnp structure is formed.

From a practical point of view, the shape of the resulting oscillations of the $I_{holding}$ is consistently reproducible, albeit at different Φ_γ values (Fig. 3).

For certain doses, *modes*, most likely values of peaks of Holding Currents *probabilities,* are in relatively narrow intervals of the numerical values of the $I_{holding}$.

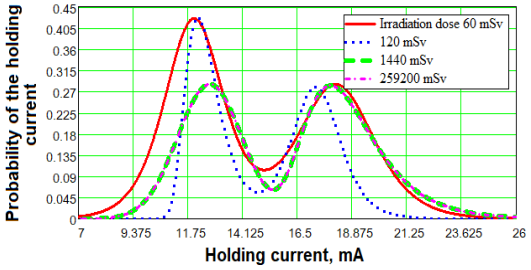

(a)

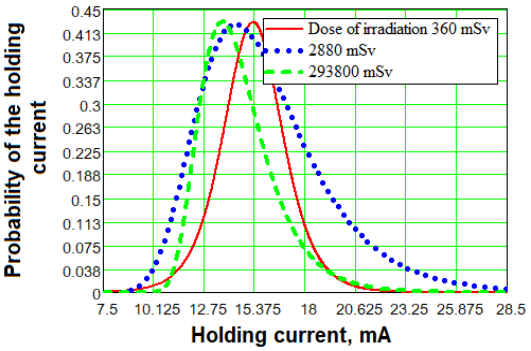

(b)

Fig. 3. The probabilities of different numerical values of $I_{holding}$, grouped by the shape of their probability distributions; a) −bimodal; b) −unimodal distributions.

Self-organization can also be understood as periodic (similar to pulsating) associated with an increase in Φ_γ, a change in the number and amplitude of peaks of the $I_{holding}$, observed at different doses of radiation (Fig. 4, Left axis**)**. In addition, there is a periodic change in the difference (**Δ**) (Fig. 4, Right axis) numerical values of peak amplitudes, including **Δ** = 0 observed for the same defined values Φ_γ, in which the distribution of the $I_{holding}$ is unimodal.

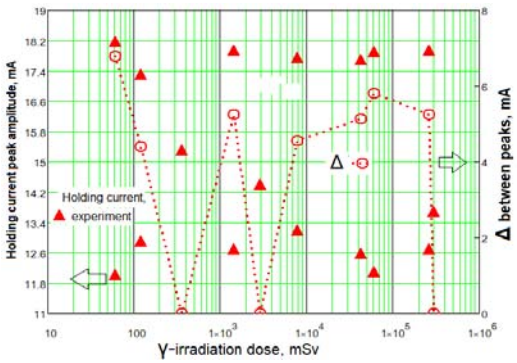

Fig. 4. Pulsating change in the amplitude of peaks (extremes) of $I_{holding}$ in a wide range of Φ_γ.

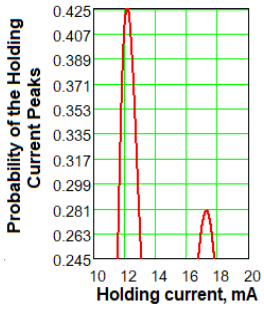

Fig. 5. A pronounced difference in the amplitudes of the left (extreme distribution) and right (logistic) extremes (peaks) of the Holding Current at $\Phi_\gamma = 120$ mSv.

The same calculations were made for every value of the *probability of $I_{holding}$ peak* at different Φ_γ, Fig. 6.

$$I\_hold\_peaks\_control\_Si := \begin{pmatrix} 60 & 12.01 & 0.4206 \\ 60 & 18.18 & 0.2842 \\ 120 & 12.9 & 0.425 \\ 120 & 17.3 & 0.281 \\ 360 & 15.3 & 0.429 \\ 1440 & 12.7 & 0.285 \\ 1440 & 17.95 & 0.283 \\ 2880 & 14.4 & 0.425 \\ 7800 & 13.185 & 0.428 \\ 7800 & 17.75 & 0.292 \\ 42120 & 12.57 & 0.2855 \\ 42120 & 17.7 & 0.2824 \\ 60480 & 12.1 & 0.419 \\ 60480 & 17.9 & 0.286 \\ 259200 & 12.7 & 0.285 \\ 259200 & 17.95 & 0.282 \\ 293800 & 13.694 & 0.43 \end{pmatrix}$$

$\Phi\gamma := I\_hold\_peaks\_control\_Si^{\langle 0 \rangle}$ **[mSv]**

$I\_hold\_peaks\_Si := I\_hold\_peaks\_control\_Si^{\langle 1 \rangle}$ **[mA]**

$Prob\ I\ hold\ peaks\ Si := I\ hold\ peaks\ control\ Si^{\langle 2 \rangle}$

Fig. 6. Experimental results for visualization of the value of the probability of $I_{holding}$ peaks at different Φ_γ

Increasing the radiation dose Φ_γ in the studied range leads to a decrease in the likelihood of $I_{holding}$ peaks with a high amplitude, and, accordingly, an increase in the possibility of peaks with a lower amplitude of $I_{holding}$ when enlarged Φ_γ. For certain ranges of Φ_γ, the effect of the maximum of $I_{holding}$ peaks probabilities exists, Fig. 7.

Using MathCAD shows ***two*** numerical values of Φ_γ, in which the so-called "effect of small doses" [19] is observed, Fig. 8.

Reduced probability of high-amplitude currents means longer (increased) lifetimes of minority charge carriers τ_p in the wide thyristor n-base after irradiation by $\Phi_\gamma \approx 4.2\ 10^4$ mSv. Data in [20, p. 55] confirms that the relatively low *increase* in τ_p leads to a significant *decrease* in $I_{holding}$. The physical cause of the increase in τ_p is the transition of the crystal to an equilibrium state, which is considered to be when irradiated with small doses of γ-quanta. This is accompanied by a significant change in their electrophysical properties: an increase in the lifetime and mobility of charge carriers. Observed in a certain range of ionizing radiation doses, τ_p increases significantly due to the ordering of the structure of the crystal lattice of silicon. This is possible only by releasing the energy stored in the crystal [21].

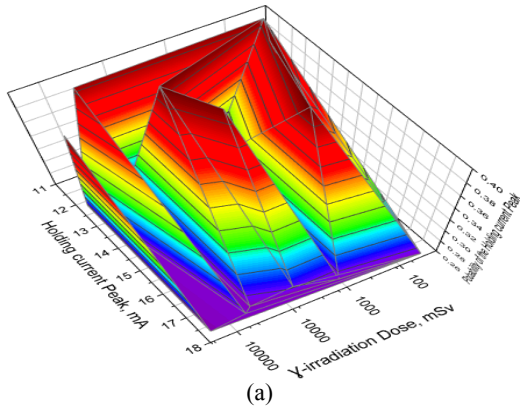

(a)

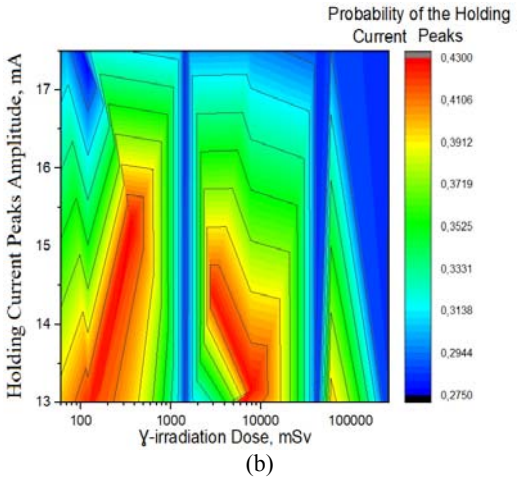

(b)

Fig. 7. The probabilities of different ranges of numerical values of $I_{holding}$ peaks, grouped by γ-irradiation doses (Origin PRO); a) 3d visualization, b) contour plot.

The process of energy storage is simplistically considered as the process of increasing the internal energy of a physical system (e.g., npnp structure), regardless of how this energy was increased (added), including, obviously, as a result of the diffusion technology of the thyristor.

According to the authors of the cited works, the effect's physical essence lies in the relaxation of energy stored in the form of defects in the crystal. Heat is released due to the annihilation of defects in the crystal lattice of a solid body during its transition to an equilibrium state in the irradiation process.

At $\Phi_\gamma \approx 4.2\ 10^4$ mSv ("small dose") there is a decrease in the probability of observing amplitude hold-current peaks range 13.6…18 mA ("high currents") from 0.411 to 0.304 or by ≈ 25.8 % (better seen in Fig. 9).

For the peaks of $I_{holding}$ with the amplitudes 12…13.5 mA ("low currents") the reduction in their probability at this radiation "small dose" is about

2.14 % (from probability ≈ 0.42 to 0.411) or almost an order of magnitude less than for the "high currents". Range ≈ $6 \cdot 10^4 \leq \Phi_\gamma \leq 1.8 \cdot 10^5$ mSv is relatively homogeneous in terms of a smooth change (decrease) in the probability of $I_{holding}$ in the range 12…18 mA. The most probable value of holding current in the range $10 \ldots 2.5 \cdot 10^5$ mSv is $I_{holding}$ = 13.5 mA (probability of this holding current ≈ 0.42…0.304 changes in a wide range, but the line $I_{holding} \approx$ const ≈ 13.5 mA practically connects the mountaintops of the "canyon" regions, i.e. the regions of holding current, in which a pronounced instability of the probabilities of the $I_{holding}$ peaks is observed. It may be considered, in this case, as the border between "high" and "low" amplitude values of the holding current.

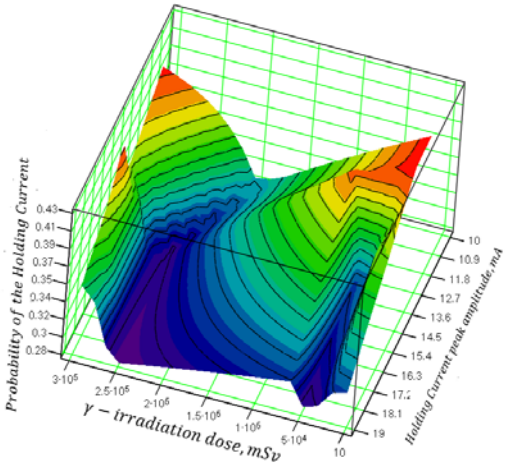

Fig. 8. Probabilities of Different Numerical Values of the Holding Current Peaks at Different γ-irradiation Doses; 3d visualization.

For $I_{holding} \geq 13.5$ mA, i.e., in the region with a less ordered structure, a **decrease in the probability of the amplitude of hold-current peaks is observed once more** at $\Phi_\gamma \approx 2.47\ 10^5$ mSv, Fig. 9. This dose is in the usually considered range of "low doses" of irradiation, ($10^4 \ldots 10^5$R ≈ 100…1000 Sv = $1 \cdot 10^5 \ldots 1 \cdot 10^6$ mSv).

So, the dose $\Phi_\gamma \approx 4.2\ 10^4$ mSv may be considered *"ultra-low"*. This effect for the thyristor sample under consideration is manifested in the range of amplitudes of the holding current peaks $13.5 \leq I_{holding} \leq 18$ [mA]. Observation of the "low-dose effects" concerning peak amplitudes of $I_{holding}$ allows reasonable selection of the criterion for rejection of npnp structures for sampling before radiation resistance tests. There is no point in testing knowingly unstable devices [22] with $I_{holding} > 13.5$ mA under the influence of γ- radiation.

4.2.2. Effect of γ-irradiation Dose on all Current Values of $I_{holding}$

There is an alternation of extremes (zones of max and min values of $I_{holding}$) forming an inhomogeneous quasi-periodic surface of the response of the thyristor holding current to the increasing dose of γ-radiation (Fig 10 a), b)). This can be represented especially clearly in the contour graph, Fig. 10 c).

The resulting contour graph is qualitative and makes it possible to visualize the possibility of *quasi-periodic recurrence* of $I_{holding}$, especially in the 11…18 mA range. At the same time, the probability of observation $I_{holding} < 11$ mA from a practical point of view, is negligibly low. The probability of $I_{holding} > 18$ mA is much more probable (Fig. 10 c)).

Visualizing the change of $I_{holding}$ using MathCAD [23] makes it possible to determine the radiation resistance limit for the device under study, i.e. dose of Φ_γ, in which there is a sharp change (deterioration) in the criterion parameter, $I_{holding}$. In this case, it is $\Phi_\gamma \approx 4.5 \cdot 10^4$ mSv.

The data provided in Fig. 1 and 2 were used to construct the relevant surface. They were reduced to a matrix, Fig. 11 a), and the surface was built using standard Mathcad technology, Fig. 11 b).

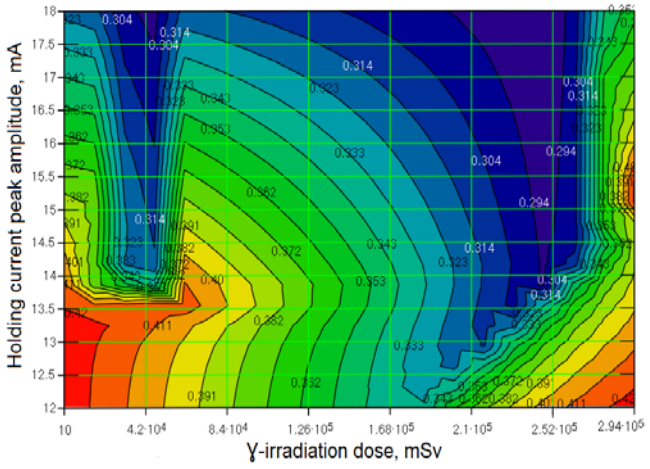

Fig. 9. Probabilities of Different Numerical Values of the Holding Current Peaks at Different γ-irradiation Doses; contour plot.

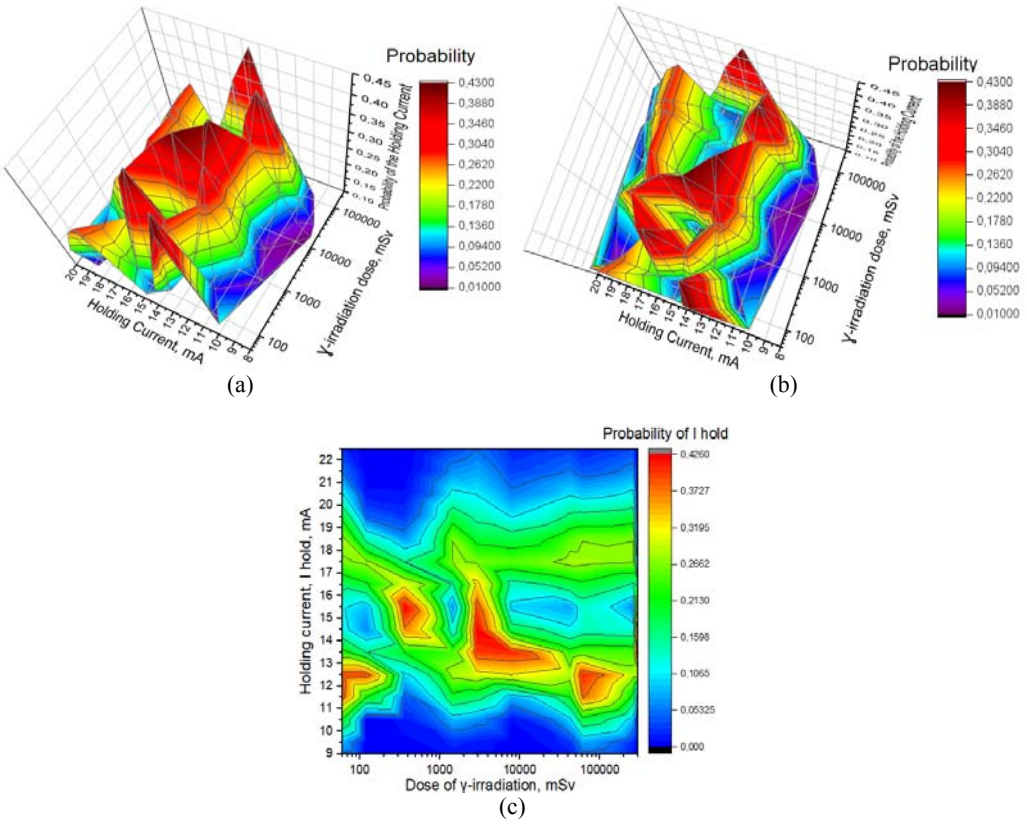

Fig. 10. Quasi-periodic Process of the radiation degradation of the planar npnp structure Holding Current (Iholding) under γ-irradiation; a, b) 3d visualization, c) contour plot.

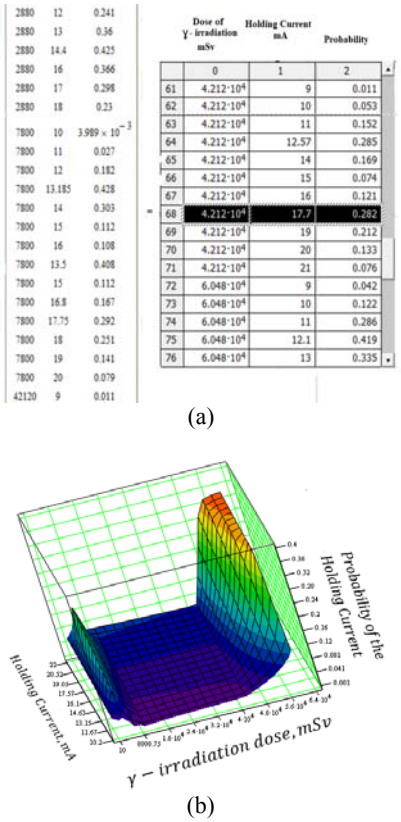

Fig. 11. Increase the likelihood of growth of npnp structure $I_{holding}$ with an increase in the dose of γ-irradiation; a) a fragment of the matrix and a table with data. The range of data for analysis (b)) selected by the *submatrix* command.

The predicted (calculated) numerical value of $I_{holding}(\Phi_\gamma)$ does not make practical sense as a consequence of the repeatability of numerical values of the holding current at different doses of radiation, but the probability of the Holding Current dependence on the dose of γ-irradiation is easily determined (Fig. 12).

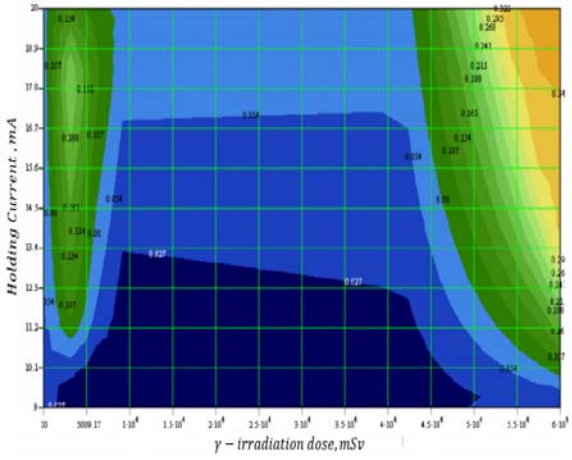

Fig. 12. Nonlinear Probability Change of the holding current, reflecting various Regularities of $I_{holding}$ (Φ_γ) degradation with an increase in the dose of γ-irradiation.

For example, when $(\Phi_\gamma) \approx 4500$ mSv the probability of the holding current $I_{holding} = 17.8$ mA is

0.188, and the probability of 11.3 mA is equal to 0.107 or about 1.7 times less.

To design the device, it is logical to use the numerical value $16.7 \le I_{holding}(4500\ mSv) \le 18.9$ [mA]. For higher doses ($\Phi_\gamma \approx 1 \cdot 10^4 \ldots 4.5 \cdot 10^4$ mSv), it is possible to consider approximately that the Probability of the Holding Current Range changes *stepwise* (Table 1):

Table 1. "Stepwise" Dependence of the Probability of the holding current in the Dose range of γ-irradiation. $\Phi_\gamma = 5 \cdot 10^4 \ldots 6 \cdot 10^4$ mSv.

No.	Range of Holding Current, $I_{holding}$, mA	Probability of the Holding Current Range
1.	9.0…13.4	0.027
2..	13.4…16.8	0.054
3	16.8…20.0	0.08

The studied npnp structure has a truly high radiation resistance in the dose range $1 \cdot 10^4 \le \Phi_\gamma \le 4.25 \cdot 10^4$ [mSv]. In this dose range, the numerical values of the holding current vary in a range approximately equal to $16.9 \le I_{holding}(1 \cdot 10^4 \le \Phi_\gamma \le 4.25 \cdot 10^4\ [mSv]) \le 20.0$ [mA], the probability of these holding currents changes from 0.054 up to 0.08.

At the other doses of γ-irradiation ($\Phi_\gamma \ge 4.5 \cdot 10^4$ mSv and $\Phi_\gamma \le 1 \cdot 10^4$ mSv) the probability of $I_{holding}$ may be an order of magnitude higher (Fig. 12).

From the point of view of assessing the degradation of the npnp structure Holding Current, when $I_{holding}(\Phi_\gamma)$ approaching the maximum value, of interest, is the visualization of the probability of the holding current in the range $5 \cdot 10^4 \le \Phi_\gamma \le 6 \cdot 10^4$ [mSv], Fig. 13.

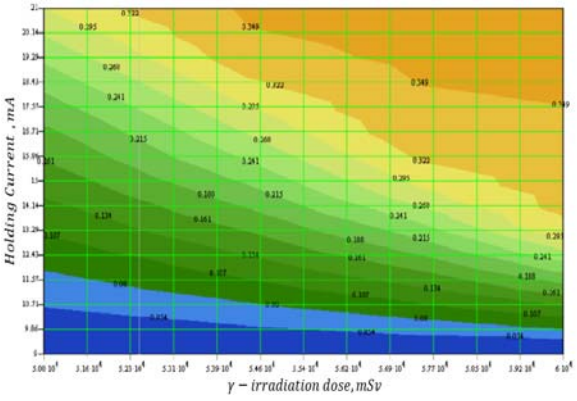

Fig. 13. Probability Increase Feature of $I_{holding}$ ("spiral staircase") when approaching the dose Φ_γ, at which the maximum of Holding Current is achieved.

The probability distribution of numerical values of the Holding Current in the entire studied range of Φ_γ (Fig. 14) indicates the possibility of the existence of various degradation mechanisms of the $I_{holding}$ at different doses of γ-irradiation. This fact is reflected by two intersecting surfaces.

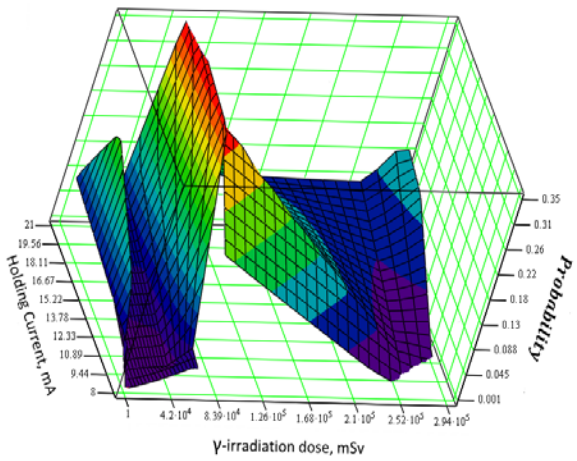

Fig. 14. Visualizing of numerical probabilities of the Holding Current in everything under study range of Φ_γ..

With an accuracy, sufficient for a practical assessment of the radiation resistance of the thyristors of the type under consideration, it is possible to consider, that at $\Phi_\gamma \approx (5.88 \mp 0.7) \cdot 10^4$ mSv there will be a sufficient increase in the probability of $I_{holding}$ = 21 mA (up to 0.349) compared to the likelihood of a "***boundary value"*** of $I_{holding} \approx 13.8$ mA (0.323), Fig. 15 a).

This value can be considered "borderline" due to the stability of the high probability of holding currents in the "yellow" and "dark-yellow" zones from 0,323 to 0,349. The probability of holding currents less than 13.8 mA ("green" zones with different shades) is significantly lower, equal to 0,296…0,215 and there are no areas with stable probability. Compared to the ***min*** value of $I_{holding}$ $(5.88 \mp 0.7) \cdot 10^4$ mSv) = ***9*** mA, the probability of which is 0.054, the probability of the ***max*** value $I_{holding}$ $((5.88 \mp 0.7) \cdot 10^4)$ mSv) = ***21*** mA at this dose significantly increase up to 0.349 (≈ ***5.46*** times).

This phenomenon is also observed at lower γ-irradiation doses but is less pronounced. For example, at $\Phi_\gamma = 3.68 \cdot 10^4$ mSv **probability** ***P*** (21 mA) = 0.08, ***P*** (9 mA) = 0.027. This means that the probability of the *max* value of $I_{holding}$ exceeds the *min* value by ≈ 2.96 times. For ***max*** $\Phi_\gamma = 2.94 \cdot 10^5$ mSv (Fig. 15 b)) the probability of $I_{holding} \le 11$ mA is negligibly small and equal to $2.878 \cdot 10^{-4}$. The experimental observation of such confinement currents is practically impossible. Therefore it is logical to consider, that $I_{holding} \approx 11$ mA with a probability of 0.027 is the minimum possible holding current at this dose.

The **P**robability of the max value **P**(21mA) = 0.135, therefore the probability of the ***max*** value $I_{holding} \approx 21$ mA exceeds the ***min*** value of $I_{holding} \approx 11$ mA approximately ***5*** times: $\left(\frac{0,135}{0,027} = 5\right)$;

The same is true for $I_{holding} \approx 12.74$ mA with the same probability. The Holding Currents in the other ranges have a probability ≠ 0 (Table 2).

Table 2. Dependence of the probability of the holding current at the dose range of γ-irradiation $\Phi_\gamma \approx 3 \cdot 10^5$ mSv.

No.	Range of Holding Current, $I_{holding}$, mA	Probability of the Holding Current
1	8.97…10.855	$2.878 \cdot 10^{-4}$
2	10.855…12.74	0.027
3	12.74…14.24	0.054
4	14.24…15.75	0.081
5	15.75…17.25	0.1
6	17.25…20.645	0.135

Due to the ***difference*** of zero of holding current probability in the range No 2…6, it may be measured. This means, that the degradation processes, occurring in the thyristor during irradiation, are stochastic.

A sign of stochastic radiation degradation of $I_{holding}$ at $\Phi_\gamma \approx 3 \cdot 10^5$ mSv is a gradual increase in the probability of reaching its max value (≈ 21 mA is the probability of the event 13.5 %) and extremely low probability ($2.878 \cdot 10^{-4}$) of $I_{holding} \leq 11$ mA ("red zone" in Fig. 15, b).

Reaching the $I_{holding}$ ***max*** value is also possible with $2.32 \cdot 10^4 \leq \Phi_\gamma \leq 2.57 \cdot 10^4$ [mSv], it's the practical failure of the device, but the probability of the event is only ≈ 8 %. The most dangerous dose at which failure is likely ≈ 35 % of the npnp thyristors is $\Phi_\gamma = (5.88 \mp 0.7) \cdot 10^4$mSv.

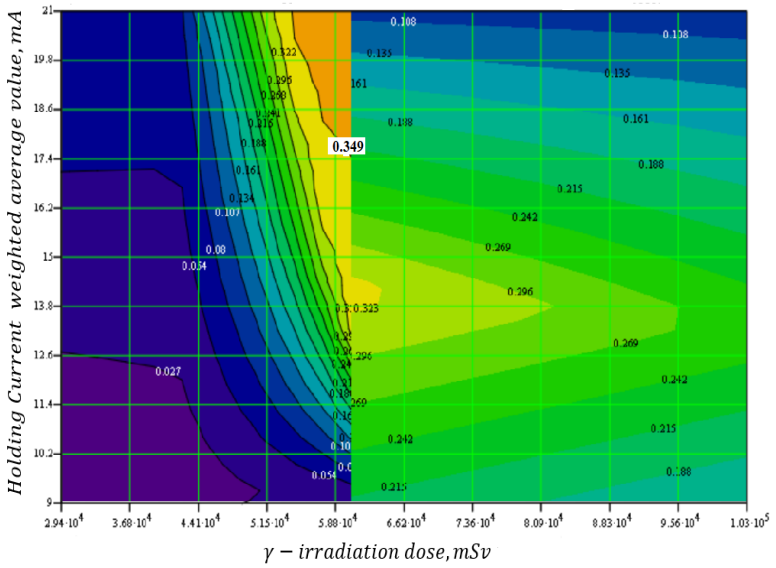

(a)

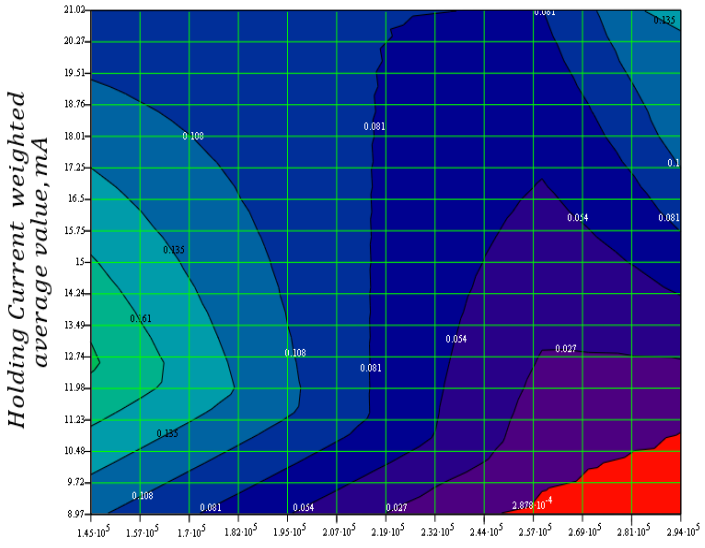

(b)

Fig. 15. Changing the probability of numeric values of the Holding Current at different doses of γ- radiation.

4.3. Statistical Estimates of Distribution Parameters, Describing the Holding Current ($I_{holding}$) Changes of the Thyristors (Low-power npnp Structure) under γ-irradiation at Different Doses

The specific feature of calculating the expected value and variance of the $I_{holding}$ for bimodal distributions (for example, for Φ_γ = 7800 mSv), is the calculation of the coefficients for the terms of the probability density functions of the numerical values of the $I_{holding}(\Phi_\gamma)$.

Let's calculate the probability density function of the holding current at a certain radiation dose, in this case at Φ_γ = 7800 mSv. Used (Fig. 16) probability distribution of Holding Current numerical values in the range 9…26 mA.

A brief description of the proposed methodology for calculating the coefficients of distribution peaks in MathCAD is as follows. Using the approach, proposed in [24, p.28], the probability density of the holding current ($I_{holding}$) numerical values at a given radiation dose may be expressed in the bimodal form (two peaks), formulas (1), (2):

$$f_{probability_{density}} = k_{left_{peak}} \cdot \cdot f_{left\_peak\_I_{holding}\_probability\_density} \cdot + \ldots + + k_{right\_peak} \cdot \cdot f_{right\_peak\_I_{holding}\_probability\_density}, \quad (1)$$

$$k_{right\_peak} + k_{right\_peak} = 1 \quad (2)$$

Calculated the integral likelihood (integral probability) of observing the experimental values of the holding current for thyristors on the control silicon in the entire studied range of $I_{holding}(\Phi_\gamma)$, i.e. from 9 to 26 mA (3) (the *denominator*).

Results of the k_{left_peak} and k_{right_peak} calculations are in the same cells.

The Denominator (the same for both peaks) =

$$= \int_9^{26} Probability\_I\_hold\_Si\_7800(I\_hold\_Si) \cdot \cdot dI\_hold\_Si, \quad (3)$$

Similarly the integral probabilities of the *first* (left) (4), (5) and *second* (right) (6), (7) peaks were calculated (the ***numerators***).

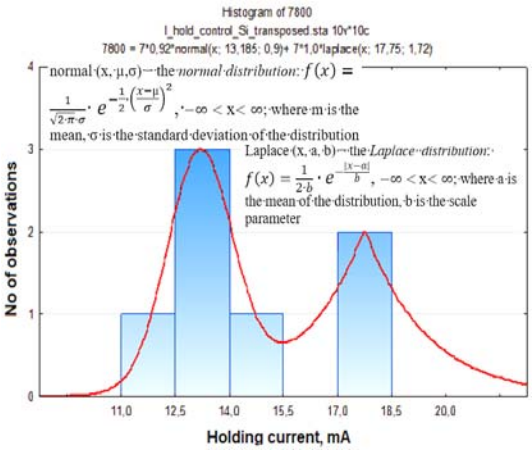

Probability of the Iholding at Φ_γ = 7800 mSv in the range 9...26 mA:

$$a\_I\_hold\_7800 = 17.75 \qquad b\_I\_hold\_7800 = 1.72$$

$$Probability\_I\_hold\_Si\_7800\ (I\_hold\_Si) = = 0.92 \cdot dnorm(I\_hold\_Si, 13.185, 0.9) + + 1.0 \frac{1}{2 \cdot b\_I\_hold\_Si\_Z800} \cdot e^{\frac{-|I\_hold\_Si - a\_I\_hold\_Si\_7800|}{b\_I\_hold\_Si\_7800}}$$

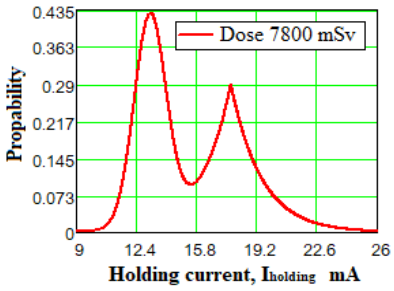

Fig. 16. Sequence for calculating in MathCAD the probability density of the holding current bimodal probability distribution, a) Histogram and distribution function of $I_{holding}$(7800 mSv); b) formula for calculating the Holding Current Probability of Numerical Values in the range 9…26 mA at the same Φ_γ; c) visualization of the probability of $I_{holding}$ in the same range.

*The Nominator (**left peak**)*:

$$0.92 \cdot \int_9^{26} dnorm(I\_hold\_Si), 13.185, 0.9) \cdot \cdot dI\_hold\_Si \quad (4)$$

The coefficient of the left peak:

$$\frac{\int_9^{26} 0.92 \cdot dnorm(I\_hold\_Si), 13.185, 0.9) \cdot dI\_hold\_Si}{\int_9^{26} Probability\_I\_hold\_Si\_7800(I\_hold\_Si) \cdot dI\_hold\_Si} = = \mathbf{0,481} \quad (5)$$

*The Nominator (**right peak**)*:

$$\int_9^{26} \frac{1}{2 \cdot b\_I\_hold\_Si\_7800} \cdot \left(e^{\frac{-|I\_hold\_Si - a\_I\_hold\_Si\_7800|}{2 \cdot b\_I\_hold\_Si\_7800}}\right) \cdot \cdot dI\_hold\_Si \quad (6)$$

The coefficient of the right peak:

$$\frac{\int_9^{26} \frac{1}{2 \cdot b\_I\_hold\_Si\_7800} \cdot \left(e^{\frac{-|I\_hold\_Si - a\_I\_hold\_Si\_7800|}{2 \cdot b\_I\_hold\_Si\_7800}}\right) \cdot dI\_Si}{\int_9^{26} Probability\_I\_hold\_Si\_7800(I\_hold\_Si) \cdot dI\_hold\_Si} = = \mathbf{0.519} \quad (7)$$

Then the density of the probability distribution for $I_{holding}$ at Φ_γ = 7800 mSv may be expressed as (8).

$$f_{probability\_density} = \\ =0.481 \cdot dnorm(I\_hold\_Si, 13.185, 0.9) + 0.519 \frac{1}{2 \cdot b\_I\_hold\_Si\_7800} \cdot e^{\frac{-|I\_hold\_Si - a\_I\_hold\_Si\_7800|}{2 \cdot b\_I\_hold\_Si\_7800}} \quad (8)$$

Calculation of the numerical values of the standard parameters, characterizing the resulting distributions, was carried out [25]: weighted average value $\tilde{X}$ (mathematical expectation, M[X]) experimental results of measurements of the holding current of samples set of npnp thyristors and dispersion D[X] of this physical quantity, where $x \equiv I_{holding}(\Phi_\gamma)$ is a holding current value in the measurement interval, $\varphi(x) \equiv f(I_{holding}(\Phi_\gamma))$ is a density of the probability distribution, formulas (), ().

$$\tilde{X} = M[X] = \int_{-\infty}^{\infty} x\varphi(x)dx, \quad (9)$$

$$D[X] = \int_{-\infty}^{\infty} (x - M[X])^2 \varphi(x)dx, \quad (10)$$

Application example of $f_{probability\_density}$ *of* $I_{holding}(\Phi_\gamma)$ *usage* to calculate Holding Current distribution parameters (**M_7800** is a mathematical expectation of I_hold_Si at Φ_γ = 7800 mSv, **D_7800** is the Holding Current Dispersion), depicted in Listing 1 a), b).

Calculated $I_{holding}(\Phi_\gamma)$ weighted average values and weighted average deviation (square root of dispersion) are in Fig.17, a), b).

a) *Weighted average value of* $I_{holding}$ *at* $\Phi_\gamma = 7800$ *mSv, M_7800:*

$$M\_7800 = \int_9^{26} \left(0.481 \cdot dnorm(I\_hold\_Si, 13.185, 0.9) + 0.519 \frac{1}{2 \cdot b\_I\_hold\_Si\_7800} \cdot e^{\frac{-|I\_Si - a\_I\_hold\_Si\_7800|}{2 \cdot b\_I\_hold\_Si\_7800}}\right) I\_hold \cdot dI\_hold = 15.554\ [mA],$$

b) *Holding Current Dispersion at* $\Phi_\gamma = 7800$ *mSv, D_7800:*

$$D\_7800 = \int_9^{26} \left(0.481 \cdot dnorm(I\_hold\_Si, 13.185, 0.9) + 0.519 \frac{1}{2 \cdot b\_I\_hold\_Si\_7800} e^{\frac{-|I\_Si - a\_I\_hold\_Si\_7800|}{2 \cdot b\_I\_hold\_Si\_7800}}\right) \left(I_{hold_{Si}} - M_{7800}\right)^2 \cdot dI\_hold,$$

$$Weighted\ average\ deviation\ \sqrt{D\_7800} = 2.943\ [mA]$$

Listing 1. Calculation example in Mathcad of the Holding Current ($I_{holding,\ mA}$) weighted average value at Φ_γ = 7800 mSv (a)) and its dispersion (b)

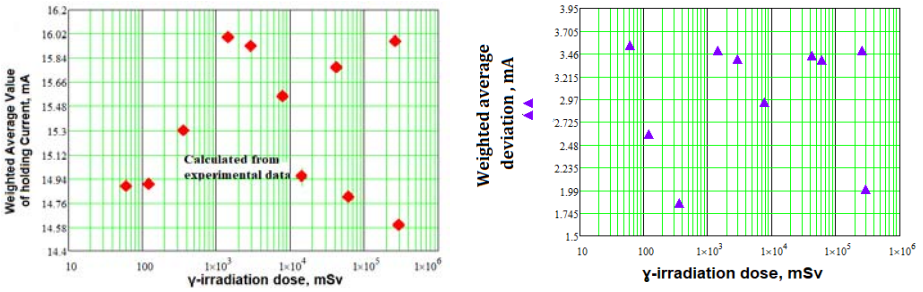

(a) (b)

Fig. 17. Dose dependence of the $I_{holding}(\Phi_\gamma)$ weighted average value, a) weighted average deviation (square root of dispersion), b) calculated from experimental data.

From the authors' [26, p. 38] point of view, based on the analysis of publications, concerning the so-called "complex" problems of radiation physics, caused by the combination of nonlinearity and strong non-equilibrium of processes during the irradiation of objects of various natures, in *the seemingly complete disorder* of an object (the supposedly *chaotic distribution of numerical values of the holding current, weighted average deviation*), the properties of the hidden order can be manifested.

So, one of the main tasks of modeling was identifying ranges of the γ-irradiation doses which allowed description by an analytic dependence (curve) of experimental $I_{holding}(\Phi_\gamma)$ dependence and the same for holding current dispertion.

5. Quantitative Dependencies, Describing the Holding Current ($I_{holding}$) Degradation at Different γ-irradiation Doses over the Entire Range of Radiation Doses

5.1. Modeling the Dose Dependence of the Holding Current, $I_{holding}(\Phi_\gamma)$

The possibilities of Origin PRO were used to simulate the change in the holding current during irradiation [27]. For example, the results of the calculations of $I_{holding}(\Phi_\gamma)$ at $60 \leq \Phi_\gamma \leq 2000$ mSv are shown in Fig. 18.

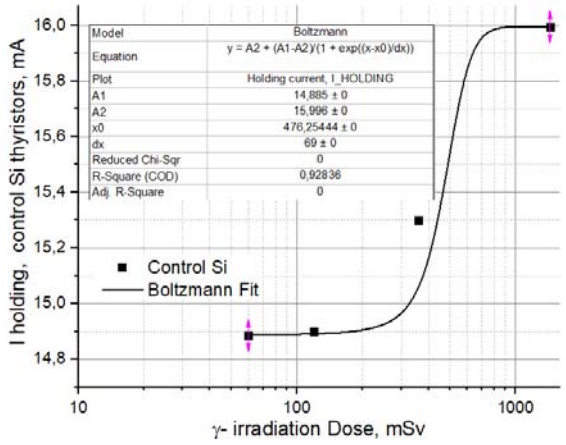

Fig. 18. Origin Pro Approximation Case Study $I_{holding}(\Phi_\gamma)$ at $60 \le \Phi_\gamma \le 2000$ [mSv].

For more simple calculations the resulting Origin PRO models were *represented in MathCAD (Listing 2)*.

The calculation results are shown in Fig. 19. The fully radiation-resistant npnp test structure exists when the irradiation range is $0 \le \Phi_\gamma \le .200$ [mSv].

At $200 \le \Phi_\gamma \le 1000$ [mSv] there is a "classical" degradation (an increase in the $I_{holding}(\Phi_\gamma)$), associated with a decrease in the lifetime of injected minority charge carriers due to the recombination processes on radiation defects.

At $\Phi_\gamma \approx 7 \cdot 10^3$ mSv in the base areas of the npnp structure, the formation of radiation defects is expected to be completed. This is indicated by the absence of an $I_{holding}(\Phi_\gamma)$ change. The strong disequilibrium of the vacancy distribution and the individual characteristics of the impurity-defective composition, which depend on the production technology of certain structures (for example, thyristors or the other types of discrete devices), lead to the possibility of implementing the so-called autocatalytic quasi-chemical reactions between defects [28]. In synergetic systems) anomalously large fluctuations arise. In this case, this is a sample of the devices under study of $I_{holding}(\Phi_\gamma)$.

The obtained results may be explained using the another concept, described in [28], namely: the possible existence of the intermittency regime, which one shows the coexistence of laminar (smooth) and chaotic (jagged) mechanisms for the accumulation and evolution of radiation defects.

$$Dose\_I\_hold := 10, 20 \ldots 10^6\ mSv$$

For the range $60 \le \Phi_\gamma \le 7000$ [mSv] the form of the equations is the following:

$$A1\_hold\_low\_dose := 14.885,\ A2\_hold\_low\_dose := 15.951,$$
$$x\_0\_I\_hold\_low\_dose := 476.2544, dx\_I\_hold\_low\_dose := 69,$$
$$\boldsymbol{I}_{hold\_low\_dose\_Si(Dose\_I\_hold)} :=$$
$$= A2\_I\_hold\_low\_dose + \frac{(A1\_I\_hold\_low\_dose - A2\_I\_hold\_low\_dose)}{1 + exp\left(\frac{(Dose\_I\_hold) - (x\_0\_I\_hold\_low\_dose)}{dx\_I\_hold\_low\_dose}\right)},$$

For the range $7000 \le \Phi_\gamma \le 3.5 \cdot 10^4$ [mSv] the form of the equations is the following:

$$I\_hold\_0\_high\_range\_dose\_Si\_2 := 14.27645, I\_hold\_x\_c\_high\_range\_dose\_Si\_2 := -19857.9878,$$
$$I\_hold\_w\_high\_range\_dose\_Si\_2 := 43736.68323, I\_hold\_A\_high\_range\_dose\_Si\_2 := 1.69026,$$
$$I\_hold\_0\_high\_range\_dose\_Si\_2(Dose\_I\_hold) :=$$
$$= I\_hold\_w\_high\_range\_dose\_Si\_2 + I\_hold\_A\_high\_range\_dose\_Si\_2 \cdot$$
$$\cdot \left[sin\left[1.071 \cdot pi \cdot \frac{(Dose\_I\_hold) - (I\_hold\_x\_c\_high\_range\_dose\_Si\_2)}{I\_hold\_w\_high\_range\_dose\_Si\_2} \right] \right]^2$$

For the range $3.584 \cdot 10^4 \le \Phi_\gamma \le 9.1 \cdot 10^5$ [mSv] the form of the equations is the following:

$$I\_hold\_0\_high\_range\_dose\_Si\_3 := 14.594, I\_hold\_x\_c\_high\_range\_dose\_Si\_3 := -300,$$
$$I\_hold\_W\_high\_range\_dose\_Si\_3 := 103800, I\_hold\_A\_high\_range\_dose\_Si\_3 := 1.372,$$
$$I\_hold\_high\_range\_dose\_Si\_3(Dose\_I\_hold) := I\_hold\_0\_high\_range\_dose\_Si\_3 +$$
$$+ I\_hold\_A\_high\_range\_dose\_Si\_3 \cdot\cdot$$
$$\cdot \left[\sin\left[\cdot \left[\frac{0.52 \cdot pi \cdot (Dose\_I\_hold) - 1 \cdot 10\text{^}5) - (I\_hold\_x\_c\_high\_range\_dose\_Si\_3)}{(I\_hold\_A\_high\_range\_dose\_Si\_3)} \right] \right] \right]^2$$

A simple program may join the obtained equations:

$$I\_hold\_Si(Dose\_I\_hold) =$$
$$:= \begin{cases} I\_hold\_low\_dose\_Si\ (Dose\_I\_hold)\ if\ 1 < Dose\_I\_hold < 2\ 10\text{^}3 \\ I\_hold\_high\_range\_dose\_Si2\ (\{Dose\}\_I\_hold + 0.001\ if\ 1.01\ 10\text{^}3 < \{Dose\_I\_hold < 3.51\ 10\text{^}4 \\ I\_hold\_high\_range\_dose\_Si\_3(Dose\_I\_hold)\ if\ 3.584\ 10\text{^}4 < (Dose\_I\_hold) < 9.1\ 10\text{^}5 \end{cases}$$

Listing 2. The Sequence of Calculation of the Approximating Dependence of the $I_{holding}(\Phi_\gamma)$ Function.

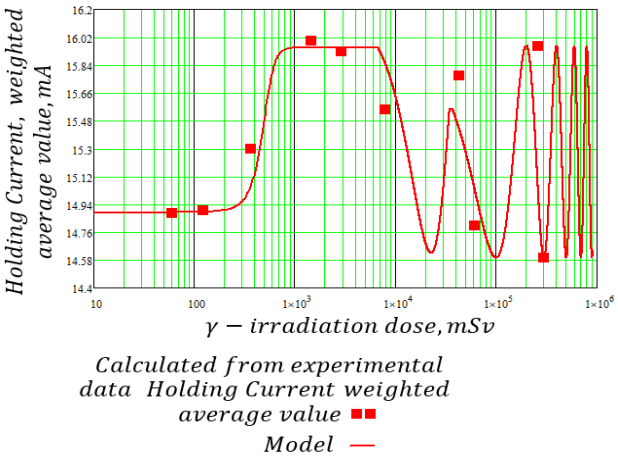

Fig. 19. $I_{holding}(\Phi_\gamma)$ Curve, Approximating the Weighted Average Value of Holding Current at Different (Φ_γ).

It's important from the practical approach. The cited work gives an impressive example. Suppose radio equipment or an element base of the electric drive is catastrophically sensitive to these fluctuations.

In that case, quasi-periodicity of failures and return of the equipment to operating condition may occur.

The experimentally shown quasi-periodicity of the change in the holding current at the different Φ_γ indicates different phases of npnp structure degradation.

The existence of chaotic (quasi-periodic) changes indicates an extraordinary evolution of defects in the device, not encountered before.

5.2. Modeling the Dose Dependence of the Holding Current Dispersion, $D_{holding\_current}(\Phi_\gamma)$

The calculation sequence is shown in Listing 3, and the results of the calculation in Fig. 20. Low doses of γ-irradiation also change the physical properties of the npnp structure in a nonlinear manner, within the range of $60 \leq \Phi_\gamma \leq 1000$ mSv there is a peak decline of $D_{holding\_current}(\Phi_\gamma)$. This may indicate a rapid improvement in the crystal structure of thyristor.

A further increase in $\Phi_\gamma > 10^3$ leads to a damped regions with different conductivity types ("low dose effect").variance oscillation (laminar (smooth) regime). There is a weakly oscillating stabilization of the properties of the Si crystal up to a dose of $\Phi_\gamma \approx 1 \cdot 10^5$ mSv. A chaotic (jagged) regime at $\Phi\gamma > 1 \cdot 10^5$ mSv may indicate an impending discrete device failure.

Significant reduction in the standard deviation of the Holding Current npnp thyristors is necessary to produce devices for parallel configurations, where good matching of electro-physical characteristics of used Devices is required [29], which can be achieved by reducing the variance of the measured parameters. Min value of standard deviation (≈ 1.85 mA) observed (Fig. 21) at $\Phi_\gamma \approx 350$ mSv and $I_{holding}(\Phi_\gamma) = 15.3$ mA. This dose can be considered technological, significantly reducing the spread of numerical values of average-weighted holding currents (decrease of $I_{holding}(\Phi_\gamma)$ standard deviation).

The observed effect most likely reflects the increase in τ_p (see Section 4.2.1).

6. Conclusions

1. The holding current degradation of a low-power npnp structure under different γ-irradiation doses ($I_{holding}(\Phi_\gamma)$) occurs non-linearly and is complicated. Shown the quasi-periodicity of the radiation change in the holding current and its dispersion.

2. Obtained experimental data confirm the theoretical approach, proposed in [28], namely: the possible coexistence of laminar (smooth) and chaotic (jagged) phase changes of physical quantity during the irradiation, which is predicted in the cited work.

This work *experimentally* showed the existence of ***different phases of $I_{holding}(\Phi_\gamma)$ degradation,*** as well as the similar changes of standard deviation (square root of Dispersion, $D_{holding\_current}(\Phi_\gamma)$.

3. Radiation resistance of npnp structure, understood as the absence of a change of $I_{holding}(\Phi_\gamma)$ at γ-exposure, is significantly lower than expected and is located in a very narrow range $0 \leq \Phi_\gamma \leq 200$ mSv. At $200 \leq \Phi_\gamma \leq 1000$ mSv *S*-shape degradation of $I_{holding}(\Phi_\gamma)$ was observed.

4. From a practical point of view, using such a low-power discrete planar npnp thyristor in the range of $1000 \leq \Phi\gamma \leq 7 \cdot 10^3$ mSv is advisable. In this very narrow range of Φ_γ holding current $I_{holding}(\Phi_\gamma)$ is very stable (the "plateau" of numerical values). Dose $\Phi_\gamma \approx 7 \cdot 10^3$ mSv is the beginning of the chaotic (jagged) phase and practically the beginning of the thyristor failure.

5. The given values of $I_{holding}(\Phi_\gamma)$ are obtained for one type of thyristor and thus are indicative. For *the realistic assessment of the radiation resistance* of *various* types of discrete devices, it is expedient to use the evaluation method used in this work, including the following (see Section 7 of the article).

a) For the range 60 ≤ Φ_γ ≤.1000 mSv

$$Dose := 10, 10 + 10..300000,$$
$$D\_0\_Si := 10.375, t0\_D\_Si := 223.99, Xc\_D\_Si := 80.028, w\_D\_\_Si := 873.874, A\_D\_Si := -41.992,$$
$$D\_Si(Dose) := D\_0\_Si + A\_D\_Si \cdot exp\left[-\frac{Dose}{t0\_D\_Si}\right] \cdot sin\left[1.137 \cdot pi \cdot \left[\frac{Dose}{w\_D\_\_Si}\right]\right],$$

b) For the range 1000 ≤ Φ_γ ≤.10^5 mSv:

$$D\_0\_middle\_range\_dose\_Si := 10.01, \quad W\_middle\_range\_dose\_Si := 12300$$
$$t\_0\_middle\_range\_dose\_Si := 72698.78101, A\_middle\_range\_dose\_Si := 0.864488,$$
$$x\_c\_middle\_range\_dose\_Si := -4710,$$

$$D\_iddle\_range\_dose\_Si(Dose) :=$$
$$= D\_0\_middle\_range\_dose\_Si + A\_middle\_range\_dose\_Si \cdot exp\left(\frac{-Dose}{t\_0\_middle\_range\_dose\_Si}\right) \cdot\cdot$$
$$sin\left[0.7002 \cdot pi \cdot \left(\frac{(Dose+5\cdot 10\text{^}3)-x\_c\_middle\_range\_dose\_Si}{w\_middle\_range\_dose\_Si}\right)\right],$$

c) For the range $\Phi_\gamma \geq 10^5$ mSv:

$$D\_0\_high\_range\_dose\_Si := 3.6, x\_c\_high\_range\_dose\_Si := 110000,$$
$$A\_high\_range\_dose\_Si\} := 7.5, w\_high\_range\_dose\_Si := 228000,$$
$$D\_high\_range\_dose\_Si(Dose) := D\_0\_high\_range\_dose\_Si + A\_high\_range\_dose\_Si \cdot$$
$$\cdot \left[sin\left[2.35 \cdot pi \cdot \frac{(Dose+6.5\cdot 10\text{^}4)-(x\_c\_high\_range\_dose\_Si)}{w\_high\_range\_dose\_Si}\right]\right]\text{^}2,$$

d) Final equation:

$$Dispersion\ (Dose) := \begin{cases} D\_Si(Dose) + 0.34, if\ 1 < Dose < 3.38\ 10\text{^}3 \\ D\_middle\_range\_dose\_Si\ \{Dose\}) - 0.1, if\ 2\ 10\text{^}3 < Dose < 1.065\ 10\text{^}5 \\ D\_high\_range\_dose\_Si\ (Dose), if\ 1.085\ 10\text{^}5 < Dose < 5.4\ 10\text{^}5 \end{cases}$$

Listing 3. Modeling of the Dose Dependence of the Holding Current Dispersion, $D_{holding\_current}(\Phi\gamma)$.

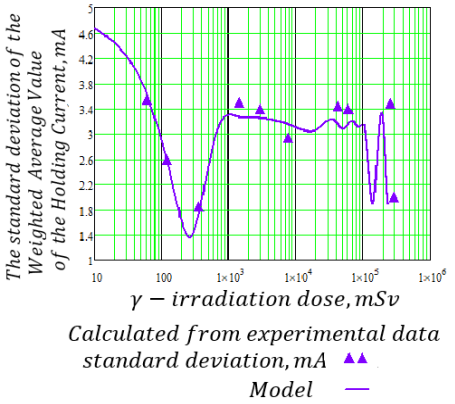

Fig. 20. Non-linear Dose Dependence of the Holding Current Weighted Average Value standard deviation (square root of Dispersion ($D_{holding\_current}$ (Φ_γ)).

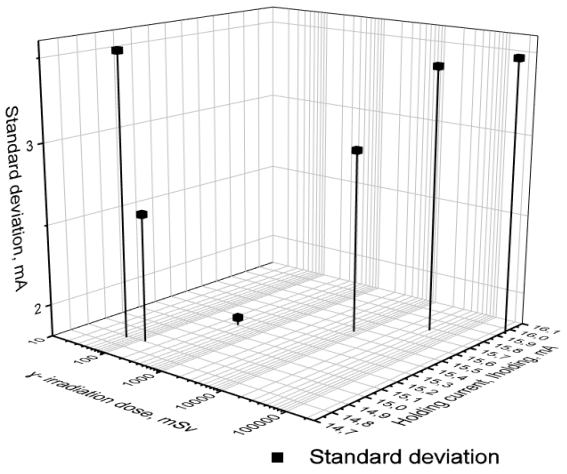

Fig. 21. Nonlinear Relationship of the standard deviation at different γ-irradiation doses.

7. Proposal

For the selected (studied) types of devices, the sample of the studied devices is irradiated with a set of doses of ionizing radiation. Measurements of the chosen parameters are to be carried out, and the experimental results obtained are processed by standard statistical methods (weighted mean, dispersion, standard deviation).

The main point is to construct dose dependences for the selected characteristics of the selected types of devices under study and to construct their approximating dependences to find laminar (smooth) and chaotic (jagged) phases. In our opinion, the laminar phase will show the ranges of *real radiation hardness (no changes)* and *predictable* changes of

device parameters under irradiation. The beginning of the chaotic phase indicates the end of the reliable npnp structure operation and the possibility of soon device failure.

References

[1]. Q. Huang, Investigation of radiation-hardened design of electronic systems with applications to post-accident monitoring for nuclear power plants, https://ir.lib.uwo.ca/etd/6025

[2]. V. Ovchinnikov, et al., Robotics in Chernobyl, *Civil Security Technology*, Vol. 16, Issue 4, 2019, pp. 70-78.

[3]. R. Smith, et al., Robotic Development for the nuclear environment: challenges and strategy, *Robotics*, Vol. 9, Issue 4, 2020, 94.

[4]. S. Coloma, et al., The effect of ionizing radiation on robotic trajectory movement and electronic components, *Nuclear Engineering and Technology*, Vol. 55, Issue 11, Nov. 2023, pp. 4191-4203,

[5]. W. Wang, et al., Robot Protection in the Hazardous Environments, *IntechOpen*, 2017.

[6]. Solid State Relays (SSR) For Space Applications, https://www.doeeet.com/content/eee-components/actives/solid-state-relays-ssr-for-space-applications/

[7]. A. Tasker, Considerations for Designs Using Radiation-Hardened Solid State Relays, Application Note AN-1068, Rev. A, https://www.infineon.com/dgdl/Infineon-Considerations_for_Designs_Using_Radiation-Hardened_Solid_State_Relays-ApplicationNotes-v01_01-EN.pdf?fileId=8ac78c8c84f2c0670184f501f53b1470

[8]. Electronics Tutorials, Solid State Relay, https://www.electronics-tutorials.ws/power/solid-state-relay.html

[9]. E. I. Yurevich, Fundamentals of Robotics: a Textbook in Specialty "Robots and Robotic Systems", 3rd Ed., :*BHV-Petersburg*, 2010.

[10]. J. Laifr, Radiation tolerant power electronics for space applications, PhD Thesis, *Czech Technical University in Prague*, November 2018.

[11]. Dealing with High-Radiation Environments, AVNET, https://www.avnet.com/wps/wcm/connect/onesite/de21c984-9388-47b0-85cb-d1b02310a936/def-aero-satellite-wp.pdf?MOD = AJPERES&CVID = mXtnMby&CVID = mXtnMby&attachment = true&id = 1575672031818)

[12]. P. Selyshchev. Self-organization of radiation defects: temporal dissipative structures*, International Journal of Engineering, Mathematical and Physical Science*, Vol. 7, Issue 6, 2013, pp. 1050-1053.

[13]. S. V. Bytkin. Quasi-periodic process of radiation degradation of the planar npnp structure holding current (iholding) under γ-irradiation, in *Proceedings of the 6th International Conference on Microelectronic Devices and Technologies (MicDAT'2024)*, 25-27 September 2024, Ibiza (Balearic Islands), Spain, pp. 5-11.

[14]. S. Bytkin, Radiation Degradation individual peculiarities of γ-irradiated discrete low power thyristors, manufactured on Si and SiGe, *Sensors & Transducers*, Vol. 263, Issue 4, December 2023, pp. 45-57.

[15]. MIL-STD-750D Test Methods for Semiconductor Devices. Method 4201.2 Holding Current, USA DoD, https://www.navsea.navy.mil/Portals/103/Documents/NSWC_Crane/SD-18/Test%20Methods/MILSTD750.pdf

[16]. Passport # 4792 for a sealed gamma-radiation source with Americium-241 radionuclide, type IGIA 5-1, # 346.

[17]. STATISTICA (Data Analysis Software System), Version 10, https://www.statsoft.com

[18]. P. Selyshchev, Influence of stochastic conditions on self-organization in irradiated materials, *Progress of Theoretical Physics Supplement,* Vol. 150, February 2003, pp. 419-422.

[19]. A. P. Mamontov, Effect of Small Doses of Ionizing Radiation, 2nd Ed., *Deltaplan*, 2009.

[20]. P. Taylor, Calculation and Design of Thyristors, *Energoatomizdat,* 1990.

[21]. A. V. Mostovshchikov, Types of Stored Energy in Solids: Monograph, *Publishing House of Tomsk Polytechnic University*, 2017.

[22]. S. A. Avdyushkin, I. A. Maksimov, S. G. Kochura, Problematic issues of application of methods of accelerated radiation testing of ECB, *Siberian Aerospace Journal*, Vol. 24, Issue 2, 2023, pp. 280-290.

[23]. B. Maxfield, Engineering with Mathcad, Using Mathcad to Create and Organize Your Engineering Calculations, *Butterworth-Heinemann*, 2006.

[24]. R. N. Vadzinsky, Reference Book on Probability Distributions, *Nauka,* 2001.

[25]. M. A. Kovaleva S. B. Voloshin, Data Analysis. Textbook, *World of Science*, 2019.

[26]. B. L. Oksengendler, A. Kh. Ashirmetov, F. A. Iskandarova, et al., Interaction of radiation with hierarchical structures, *Surface, X-ray, Synchrotron and Neutron Studies*, Vol. 1, 2023, pp. 37-49.

[27]. Introduction to Curve Fitting, https://www.originlab.com/videos/details.aspx?id = 36

[28]. B. L. Oksengendler, A. F. Zatsepin, A. Kh. Ashirmetov, et al., The concept of "complexity" in radiation physics, *Surface, X-ray, Synchrotron and Neutron Studies*, Vol. 6, 2022, pp. 1-11.

[29]. Z. Zimek, Application of radiation technologies for the modification of electronic devices, Chapter 21, in Applications of Ionizing Radiation in Materials Processing (Y. Sun, A. G. Chmielewski, Eds.), *Institute of Nuclear Chemistry and Technology*, Warszawa, 2017.

Sensors & Transducers, Vol. 267, Issue 4, December 2024, pp. 49-56

www.sensorsportal.com

Sensors & Transducers

Published by IFSA Publishing, S. L., 2024
http://www.sensorsportal.com

An Ultimate Hydrodynamic Model for Semiconductor Devices with Arbitrary Band Structure and Surface Effects

Muhammad El-Saba and Mahmoud-Sifeddin Taha
Ain-Shams University, Engineering College, 1 Research Av., 11517 Abbasia, Cairo, Egypt
E-mail: mhs1308@hotmail.com

Received: 10 June 2024 / Revised: 13 December 2024 / Accepted: 23 December 2024
Published: 30 December 2024

Abstract: In this article we present an advanced hydrodynamic model for studying the charge carrier transport in a wide range of semiconductor devices and sensors. The proposed includes the true energy band structure of any semiconductor material and its surface effects. The model has been compared with other transport models, and its primary results are accurate and closer to the more complex approaches, such as Monte Carlo device simulation. One of the most salient features of our model is its great attention of the convection transport and velocity gradients of charge carriers. Therefore, it handles the electron gas shear rate and viscosity near the rough surfaces of semiconductor devices. This is shown to limit the charge carrier mobility near the surface of semiconductor devices in general and the MOSFET nano-devices in particular. According to our knowledge, the electron/hole gas viscosity effects have not been treated yet in the literature of hydrodynamic modelling and simulation of semiconductor devices and sensors.

Keywords: Semiconductor devices, Hydrodynamic model, Electron gas viscosity, Energy band structure. Electron gas viscosity, Surface mobility.

1. Introduction

The hydrodynamic model (HDM) of charge carrier transport in semiconductors has gained a great attention as a compromising approach between classic and full quantum transport models [1]. In spite of its wide spread in the semiconductor industry, as a simulation tool, the HDM has been a target of a lot of criticism [2-10]. To name a few, the exaggerated electron temperature and velocity overshot in nano devices, were reported [5-6]. According to many authors the weak points of the early HDM are mainly attributed to neglecting the band structure effects [7], neglecting the convective part of the average carrier energy [8], and the crude approximations which are used to close the system of hydrodynamic equations (HDE's) [8-10].

In this article, we introduce an advanced HDM, which incorporates the semiconductor band structure effects, the convection transport of charge carriers and the semi-conductor surface effects. The article is organized as follows. In sections 2, 3, and 4 we introduce the proposed HDM and its development and closure procedure. In addition, we present, in section 5 some advanced models of the carrier-energy-dependent physical parameters to be used with the proposed HDM. In section 6, we present some results of simulation and discuss their significance. We also compare our results with Monte Carlo (MC) device simulations. Finally, we present our conclusions in section 7 and a list of references.

2. Development Methodology

We start the development procedure of the proposed HDM from the general moment equation of the Boltzmann transport equation (BTE) for the gas of

charge carriers (electrons or holes) in a semiconductor device [11]. The moment equation is simply obtained by multi-plying the BTE by a physically-meaningful quantity $\psi_j(\boldsymbol{k})$, and integrating both sides over the whole wavevector space ($\boldsymbol{k}$-space) of charge carriers.

$$\frac{\partial}{\partial t}\int_k \psi_j f_v d^3k + \int \psi_j (u_v.\nabla f_v)_j d^3k + \\ + \int \psi_j \left(\frac{F}{\square}.\nabla_k f_v\right) d^3k \;=\; \int \psi_j \left[\frac{\partial fv}{\partial t}\right]_{col} d^3k, \tag{1a}$$

where $f_v = f_v(\boldsymbol{x},\boldsymbol{k},t)$ is the carrier distribution function in the phase space, which combines the physical space: $\boldsymbol{x} = [x,y,z]^T$, and the carrier wavevector space: $\boldsymbol{k} = [kx,ky,kz]^T$. The subscript '$_v$' stands for '$_n$' for electrons and stands for '$_p$' for holes. Also, $\boldsymbol{u_v}$ is the carrier group velocity ($u_v = h^{-1}dE_v/dk$), where $E_v(k)$ is the carrier (conduction electron or valence holes) energy (band structure. Finally, $\boldsymbol{F}$ is the externally-applied force, and, $\psi_j = \psi_j(\boldsymbol{k})$ is a multiplier weight function. The resulting set of conservation equations has the following general form:

$$\frac{\partial}{\partial t} n\langle\psi_j\rangle + \nabla.\, n\langle u_v \otimes \psi_j\rangle + n\left\langle\frac{F}{\square}.\nabla_k \otimes \right. \\ \left. \otimes\, \psi_j\right\rangle \;=\; \left[\frac{\partial}{\partial t} n\langle\psi_j\rangle\right]_{col} \tag{1b}$$

Here, n is the average carrier density and the angular brackets <..> denote the statistical average over the carrier distribution function in the k-space

$$<\psi(\boldsymbol{k})> = \int z\; \psi(\boldsymbol{k})\, f_v(\boldsymbol{x},\boldsymbol{k},t)\; d^3\boldsymbol{k} \,/\, n, \tag{1c}$$

where $z = 2/(2\pi)^3$ is the density of states in the k-space, and $n = \int z\, f_v(\boldsymbol{x},\boldsymbol{k},t)\; d^3\boldsymbol{k}$. Note that we put $\nabla_k.F = 0$ in the derivation of (1b) from (1a), which is true if the external force $\boldsymbol{F}$ is independent of k or when $\boldsymbol{F}$ *is* normal to $\boldsymbol{k}$. Fortunately, this is the case for both electric field force ($\boldsymbol{F} = \pm e\,\boldsymbol{\zeta}$, with $\pm e$ being the charge for electrons, or holes and $\boldsymbol{\zeta}$ is the applied electric field), and the Lorentz force ($\boldsymbol{F} = \pm e\; \boldsymbol{v}_n x \boldsymbol{B}$, with $\boldsymbol{B}$ being the magnetic field density). This makes the HDM suitable for studying both conventional semiconductor devices and sensors, which employ (or measure) external magnetic fields. However, in most semi-conductor devices, $\boldsymbol{F}$ is usually due to the applied bias voltages, and therefore, $F = \pm e\boldsymbol{\zeta}$. The electric field, $\boldsymbol{\zeta} = -\nabla\square$, and the electrostatic potential, $\square$, can be found by solving the Poisson equation, using the device boundary conditions of applied bias voltages.

$$\nabla.\,(-\varepsilon\,\nabla\phi + \boldsymbol{P}) = e\,(p - n + Dop + N_t), \tag{1d}$$

where, ε is the dielectric constant, p is the concentration of holes, $\boldsymbol{P}$ is the material polarization vector, N_t is the density of traps and $Dop = |N_d^+ - N_a^-|$ is the net concentration of ionized impurities in the semiconductor.

Our proposed HDM consists of the first three moments of the BTE, with $\psi_j = 1$, the electron group velocity u_n and the electron energy E_n. For simplicity, we only write the first three moments of the BTE for electrons, which represent the conservation equations of the electron average density (n), average momentum (or velocity $\boldsymbol{v}_n$) and average energy (ω_n):

$$\partial n/\partial t \;-\; \nabla.\boldsymbol{J}_n/e) = [\partial n/\partial t]_{col}.., \tag{2a}$$

$$\partial(n\boldsymbol{v}_n)/\partial t + e\; n\; m_n^{-1}\boldsymbol{\zeta} + \nabla.\boldsymbol{P}_{ne} + \\ + \nabla.(n\;\boldsymbol{v}_n \otimes \boldsymbol{v}_n) = [\partial(n\boldsymbol{v}_n)/\partial t]_{col}, \tag{2b}$$

$$\partial(n\,\omega_n)/\,\partial t + \nabla.S_n = \zeta.\; \boldsymbol{J}_n + (\partial n\omega_n/\partial t\,)_{col} \tag{2c}$$

Here, n is the average density of conduction electrons, $\boldsymbol{v}_n = <\boldsymbol{u}_n>$ is their average velocity, $\square_n = <E_n>$ is their average energy, and $\boldsymbol{P}_{ne}$ is the electro-kinetic pressure tensor of the electron gas. By definition, $\boldsymbol{P}_{ne}$ is a second-order central moment, such that:

$$\boldsymbol{P}_{ne} = n\,<(\boldsymbol{u}_n - \boldsymbol{v}_n)\otimes(\boldsymbol{u}_n - \boldsymbol{v}_n)>, \tag{3a}$$

where the sign $\otimes$ denotes the tensorial product of two vectors. It worth notice that in we expanded the generalized moment term $n <\boldsymbol{u}_n \otimes \boldsymbol{u}_n>$, as follows:

$$n <\boldsymbol{u}_n \otimes \boldsymbol{u}_n > = \boldsymbol{P}_{ne} + n\,(\boldsymbol{v}_n \otimes \boldsymbol{v}_n) \tag{3b}$$

Also, $\boldsymbol{J}_n = -e\; n\; \boldsymbol{v}_n$ is the electron current density and $\boldsymbol{S}_n = <E_n\boldsymbol{u}_n>$ is the electron energy flux. The average collision terms, denoted by $[..]_{col.}$, at the right-hand side of the three moment equations (2a, b, c). Finally, m_n is the average mass tensor of conduction electrons, whose inverse components are defined as follows:

$$m_n^{-1}{}_{(i,j)} = <1/\hbar^2\,\partial^2 E_n/\partial k_i \partial k_j> \tag{3c}$$

Note that m_n appears naturally in the mathematical derivation of (2b) from the BTE moment equation (1b), and doesn't mean that we adopt the effective mass approximation (EMA) in the above set of hydrodynamic equations (HDE's). (2a, b, c). Actually, m_n is taken as a physical parameter in our HDM, and is considered as a function of the average electron energy ($m_n = m_n(\omega_n)$). At low electron energy, near the conduction band bottom edge, we use the term m_{no} whose value is determined experimentally. For instance, $m_{no} = 0.275 m_o$ in Si, according to the optical measurements of Sabbah and Riffe [12].

The electron current density ($\boldsymbol{J}_n$) and energy flux ($\boldsymbol{S}_n$) can be expanded into constitutive relations, from their definitions ($\boldsymbol{J}_n = -e\; n\; \boldsymbol{v}_n$ and $\boldsymbol{S}_n = <E_n\boldsymbol{u}_n>$). We show the expansion procedure in section III, when we close the system of HDE's. The average collision terms in the three moment equations (2a, b, c) are also approximated in the next section.

3. HDM System Closure Procedure

The set of HDE's contains some unknown terms (e.g., the electro-kinetic pressure and collision terms),

whose calculations need the knowledge of the electron distribution function in the phase space, $f_n(\boldsymbol{x},\boldsymbol{k},t)$. However, $f_n(\boldsymbol{x},\boldsymbol{k},t)$ is masked in the HDM development procedure. Therefore, we need some approximate closure conditions to close the system of HDE's.

The HDM system closure assumptions are mainly about approximating and modeling the following items:

- Carrier collision terms;
- Relating the electro-kinetic pressure ($\boldsymbol{P}_{ne}$) to the carrier gas pressure ($\boldsymbol{P}_n$) and the carrier temperature (T_n);
- Expanding the expressions of the carrier current density ($\boldsymbol{J}_n$) and energy flux ($\boldsymbol{S}_n$);
- Relating the average carrier energy (ω_n), to the carrier gas temperature (T_n);
- Modeling the heat flux term ($\boldsymbol{Q}_n$);
- Modeling any higher moment terms (e.g., kurtosis flux and so on), if moments are greater than three.

3.1. Collision Terms

The collision term $[\partial n/\partial t]_{col.}$, which appears explicitly in the carrier density conservation equation (2a), can be expressed as follows:

$$[\partial n/\partial t]_{col.} = -(n-n_o)/\tau_n = -U_n \tag{4a}$$

where τ_n is the lifetime of charge carriers and the net recombination rate ($U_n = R_n - G_n$) combines all the recombination rate (R_n) and generation rate (G_n) mechanisms in the semiconductor.

Because the lifetime of charge carriers is usually much greater than the energy and momentum relaxation times, ($\tau_{mn} << \tau_{wn} << \tau_n$), the collision terms in (2b,c) are usually approximated as follows:

$$[\partial n/\partial t]_{col.} = -(n-n_o)/\tau_n = -U_n, \tag{4b}$$

$$[\partial n\boldsymbol{v}_n/\partial t]_{col.} \approx -n\boldsymbol{v}_n/\tau_{mn} \tag{4c}$$

The energy dependence of the energy relaxation time, $\tau_{wn} = \tau_{wn}(\omega_n)$, which implicitly includes the energy band structure effects, can be obtained by MC simulation in the bulk of a semiconductor [13] or by measurement [14]. On the other hand, the momentum relaxation time (τ_{mn}) is not directly employed in our proposed HDM, but rather replaced with the drift mobility ($\mu_n = e\tau_{mn}/m_n$), whose model is introduced in section V-1.

3.2. Definition of the Carrier Gas Pressure and Temperature

We presume the following relation between the electron gas pressure $\boldsymbol{P}_n$ and its electro-kinetic pressure $\boldsymbol{P}_{ne}$:

$$\boldsymbol{P}_n = m_n\boldsymbol{P}_{ne} \tag{5a}$$

In fact, the ideal gas theory defines the gas pressure, $\boldsymbol{P}_n$, with a *macroscopic (k-independent)* mass density $\rho_n = n\,m_n$, as follows:

$$\boldsymbol{P}_n = \rho_n \langle(\boldsymbol{u}_n-\boldsymbol{v}_n)\otimes(\boldsymbol{u}_n-\boldsymbol{v}_n)\rangle \tag{5b}$$

Nevertheless, for the matter of compatibility with previous HDM's, where the electron gas pressure is given by: $\boldsymbol{P}_n = n\langle m_n^*(\boldsymbol{u}_n-\boldsymbol{v}_n)\otimes(\boldsymbol{u}_n-\boldsymbol{v}_n)\rangle$, we introduce here a temperature correction parameter ($\boldsymbol{g}_n$):

$$\boldsymbol{g}_n = m_n\boldsymbol{P}_{ne}\boldsymbol{P}_n^{-1} \tag{6a}$$

Therefore, we rather use the system closure condition:

$$\boldsymbol{P}_{ne} = \boldsymbol{g}_n\, m_n^{-1}\boldsymbol{P}_n \tag{6b}$$

We also adopt the ideal gas law, $\boldsymbol{P}_n = n\,k_B\boldsymbol{T}$, such that:

$$\boldsymbol{P}_{ne} = \boldsymbol{g}_n\, m_n^{-1}\, n\, k_B\boldsymbol{T}_n \tag{6c}$$

The correction parameter can be simplified as the trace of the tensor $\boldsymbol{g}_n = m_n\boldsymbol{P}_{ne}\boldsymbol{P}_n^{-1}$, where we take the sum of diagonal elements:

$$g_{n(i,i)} = m_{nii}\langle u_{ni}-v_{ni})^2\rangle / \langle m_{nii}^*(u_{ni}-v_{ni})^2\rangle \tag{6d}$$

It can be, therefore, calculated by Monte Carlo simulation [15] or modelled as a function of the average electron energy, like m_n and $\tau_{\square n}$. Fig. 1 shows the magnitude of the correction factor, according to Monte Carlo device simulation in the bulk of Si at 300K [15].

(4b)

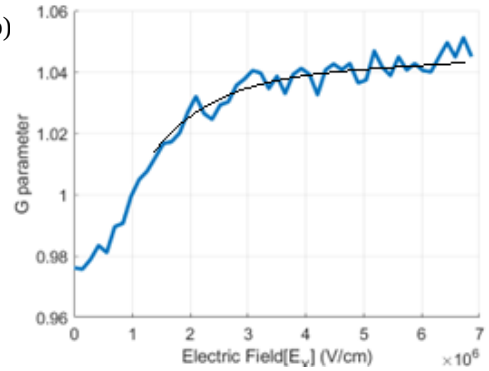

Fig. 1. Variation of the correction factor g_n and its trace versus electric field, as obtained by MC simulation, in the bulk of low-doped Si at 300K [15].

3.3. Current Density Constitutive Relation

The constitutive relations of the electron current density ($\boldsymbol{J}_n$), can be derived from its definition

($\boldsymbol{J}_n$ = -e n $\boldsymbol{v}_n$), using the momentum conservation equation(2b), in steady state

$$\nabla.(\boldsymbol{P}_{ne}) + \nabla.(n\, v_n \otimes v_n) - e\, n\, m_n^{-1}.\boldsymbol{\zeta} + + \left[\frac{\partial n\, v_n}{\partial t}\right]_{col} \quad (7a)$$

Using the momentum relaxation time approximation (4c) and substituting μ_n = eτ_{mn} /m_n and $\boldsymbol{J}_n$ = -e n $\boldsymbol{v}_n$, we get:

$$\boldsymbol{J}_n = e\, n\, \mu_n \boldsymbol{\zeta} + \mu_n\, m_n\ \nabla.\boldsymbol{P}_{ne} + + n\, \mu_n\, m_n\, (v_n.\nabla)\, v_n \quad (7b)$$

Substituting the electro-kinetic pressure ($\boldsymbol{P}_{ne}$) from its closure condition (6d), yields

$$\boldsymbol{J}_n = en\, \mu_n.\boldsymbol{\zeta} + \mu_n.m_n\, \nabla.(g_n\, m_n^{-1}\, n\, k_B T_n) + + n\, \mu_n.m_n(\boldsymbol{v}_n.\nabla)\boldsymbol{v}_n \quad (7c)$$

The above constituent relations are similar to the current density equations of the drift-diffusion model (DDM), except for the velocity gradient (or acceleration) and thermal diffusion terms. Note that the velocity gradient term is vector of three components and nine (3x3) terms, which results from the expansion of ($\nabla.(n\, v_n \otimes v_n)$).

3.4. Electron Energy Flux and Heat Flux

For expanding $\boldsymbol{S}_n$ = <$E_n\boldsymbol{u}_n$>), and ω_n = <E_n>, in terms of the electron temperature (T_n), we make use of the classical definition of electron energy E_n = ½ m_n^* v_n^2 and, therefore, apply the ideal gas laws.

$$\boldsymbol{S}_n = \boldsymbol{Q}_n + \boldsymbol{v}_n(n\, \omega_n + \boldsymbol{P}_n) = \boldsymbol{Q}_n + n\, \boldsymbol{v}_n\, (\omega_n + + k_B T_n), \quad (8a)$$

with

$$\boldsymbol{Q}_n = \int ½\, m_n^* |\boldsymbol{u}_n - \boldsymbol{v}_n|^2 (\boldsymbol{u}_n - \boldsymbol{v}_n)\, f_n\, z\, d^3\boldsymbol{k} \quad (8b)$$

As the electron distribution function, $f_n(x,k,t)$, is not known (masked) in the HDM, the electron heat flux $\boldsymbol{Q}_n$ is usually approximated, with drastic assumptions. The majority of previous formulations of the HDM, made use of the Fourier law of heat conduction to approximate the electron heat flux [16]:

$$\boldsymbol{Q}_n = -k_n^{th} \nabla T_n, \quad (9a)$$

where k_n^{th} is the electron thermal conductivity. This law was originally developed for metals, where heat conduction is primarily carried out by electrons. Therefore, the electron thermal conductivity k_n^{th} is usually modeled by the Wiedeman-Franz law at the electronic temperature [1]:

$$k_n^{th} = \gamma_n\, (k_B/e)^2\, T_n\, \sigma_n, \quad (9b)$$

where σ_n is the electrical conductivity due to electrons and γ_n is the Lorenz coefficient for electrons. According to the original Wiedemann-Franz formulation [16], γ is given by [1]:

$$\gamma_n = 5/2 + r, \quad (9c)$$

where the parameter r depends on the dominant collision mechanism. The above treatment for modeling the carrier heat flux term (Q_n), using the Fourier relation, leads to many problems in the hydro-HD simulation of semiconductor devices [7].

In the our HDM, we rather utilize an advanced heat flux model, using the 3rd order moment of the BTE [16].

$$n\boldsymbol{F}.\langle ½\, u_n^2 + u_n \otimes u_n\rangle + + \nabla.(n\langle E_n\, u_n \otimes u_n\rangle) = -\frac{S_n}{\tau_{sn}}, \quad (10a)$$

where τ_{sn} is the energy flux relaxation time of electrons. The energy flux ($\boldsymbol{S}_n$) in the above conservation equation may be then divided into two parts, namely; the convection energy part (due to $\boldsymbol{J}_n$) and the heat conduction part $\boldsymbol{Q}_n$:

$$\boldsymbol{Q}_n = -3/2\ (\ k_B^2/e)\ \mu_{sn}\, \beta_n \nabla (n\, T_n^{\,2}) = =- k_n \nabla (n\, T_n^{\,2}), \quad (10b)$$

with

$$k_n = 3/2\ (k_B^2/e)\, \mu_{sn}\beta_n \quad (10c)$$

Also, μ_{sn} is the energy flux mobility of electrons (μ_{sn} = $e\tau_{sn}/m_n$) and the beta factor (β_n) is defined as follows:

$$\boldsymbol{\beta_n} = \langle E_n(\boldsymbol{u}_n - \boldsymbol{v}_n) \otimes \otimes (\boldsymbol{u}_n - \boldsymbol{v}_n)\rangle / \omega_n \langle (\boldsymbol{u}_n - \boldsymbol{v}_n) \otimes (\boldsymbol{u}_n - \boldsymbol{v}_n)\rangle \quad (10d)$$

As shown in Figs. 2a and 2b, both β_n and μ_{sn} can be determined by MC simulation in the bulk of a semiconductor [16]. When the carrier-concentration gradient is negligible, the above formula may be further reduced to a form similar to the conventional Fourier relation ($\boldsymbol{Q}_n$ = - $k_n^{th} \nabla\ T_n$). Therefore, the thermal conductivity due to electrons in a semiconductor is given by:

$$k_n^{th} = 3\ (k_B^{\,2}/e)\ n\ \mu_{sn}\ \beta_n)\ T_n = = 3\ \beta_n\ (k_B/e)^2\ (\mu_{sn}/\mu_n)\sigma_n\ T_n \quad (11a)$$

This relation is equivalent to the well-known Wiedeman-Franz relation (k_n^{th} = $\gamma_n (k_B/e)^2\ \sigma_n\ T_n$), with the following *modified' Lorenz parameter* (γ_n):

$$\gamma_n = 3\ \beta_n\ (\mu_{sn}/\mu_n) \quad (11b)$$

In the case of low electric field, where μ_{sn} = μ_n and β_n = 1, we can easily find that γ_n = 3, which

corresponds to the classic Wiedeman-Franz relation ($\gamma_n = 5/2+r$). This indicates that our model of heat flux is more versatile than the Fourier heat flux model. It also illustrates one of the error sources when adopting the Fourier law of heat conduction in semiconductor devices, to close the set of hydrodynamic equations.

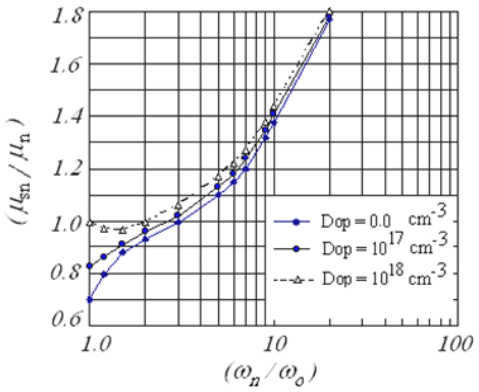

Fig. 2a. Relative energy flux mobility (μ_{sn}/μ_n) in Si at 300 K.

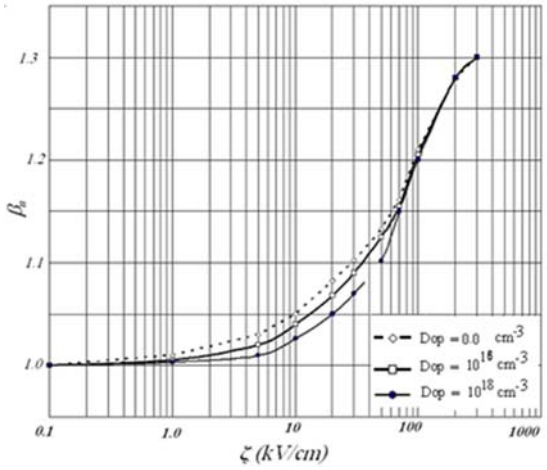

Fig. 2b. Heat flux beta factor in Si at 300K.

4. Final Set of HDE's

The final set of HDE's consists of the continuity equations of the carrier density (2a) and average carrier energy (2c), as well as the constitutive relations for the electron current density (7c) and energy flux (8a). Adding the quantum corrections [17], we can write:

$$\boldsymbol{J}_n = e\, n\, \mu_n \boldsymbol{\zeta} + \mu_n\, m_n\, \nabla.(g_n\, m_n^{-1}\, n\, k_B T_n) + \\ + n\, \mu_n\, m_n\, (v_n.\nabla)\, v_n + \boldsymbol{J}_{nq}, \tag{12a}$$

$$\boldsymbol{S}_n = \boldsymbol{Q}_n + n\, \boldsymbol{v}_n\, (\omega_n + k_B T_n), \tag{12b}$$

with

$$\omega_n = \tfrac{1}{2} m_n v_n^2 + 3/2\, k_B\, T_n + V_q \tag{12c}$$

The quantum correction potential (or Wigner potential [18]), V_q is given by:

$$V_q = \frac{\hbar^2}{8 m_n} \nabla^2 [ln\,(n)], \tag{13a}$$

and the quantum current correction is given by [17]:

$$J_{nq} = -e\, n\, \mu_n \left(\frac{\hbar^2}{6\, m_n}\right).\nabla\left(\frac{\nabla^2\sqrt{n}}{\sqrt{n}}\right) \tag{13b}$$

5. Energy-dependent Physical Parameters

The transport properties of hot carriers under high-field conditions are of great interest for high-power and high-speed semiconductor devices. Therefore, the accurate modeling of transport parameters at high fields is vital in any transport model. In the DDM, the transport parameters are usually expressed as functions of the local electric field. Nevertheless, some parameters such as the hot carrier mobility and impact ionization rate involve some non-local and energy exchange mechanisms that should better be expressed as functions of the average carrier energy, rather than the local electric field.

Fortunately, the solution of the HDM produces such information about the average carrier energy and permits to express these parameters in a physical manner, in semiconductor devices.

5.1. Energy-dependent Hot Carrier Drift Mobility

The electron drift mobility appears in the current density constitutive relation (4a). It can be expressed according to our advanced model [19]:

$$\mu_n^{-1} = \mu_{no}^{-1} \left[1 + \frac{\mu_{no}}{e\, n\, v_n^2}\left[\frac{n(\omega_n - \omega_o)}{\tau_{\omega n}} + \boldsymbol{A}.\nabla n + \right.\right. \\ \left.\left. + B.(\boldsymbol{v}.\nabla) v_n + \boldsymbol{C}.\nabla T_n + \boldsymbol{D}.\nabla m_n\right]\right], \tag{14a}$$

with

$$\boldsymbol{A} = m_n\, v_n^2 \boldsymbol{v}_n,\ B = -n\, m_n v_n, \\ \boldsymbol{C} = 3/2\, k_B\, n\, \boldsymbol{v}_n\, m_n\ \boldsymbol{D} = m_n^{-1}\, \tau_n n \boldsymbol{v}_n \tag{14b}$$

This model accounts for the non-local field effects on hot carrier transport, as well as other driving forces, due to gradient terms. In particular, the role of velocity gradients is depicted in Fig. 3, where the electron drift mobility of Si is plotted versus the average electron energy, at various values of the dimensionless parameter ($\tau_{wnn}\, \partial v_{ny}/\partial x$). It is clear from this figure that the electron gas viscosity plays a fundamental role in limiting the electron drift mobility near the surface of the semiconductor (e.g., the top surface of an n-channel planar MOSFET).

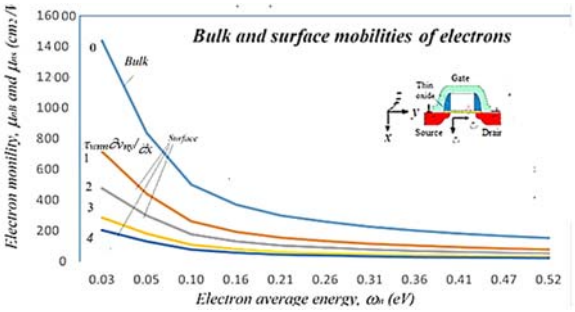

Fig. 3. Variation of the drift mobility of hot electrons, as a function of the electron average energy, and at various values of the velocity gradient ($\tau_{wn}\partial v_{ny}/\partial x$) near the surface of an n-channel MOSFET device. The low-field mobility u_{no} is assumed 1450 cm^2/V.s. After Taha and Saba [19].

5.2. Energy-dependent Impact Ionization Coefficient

The impact ionization is one of the generation mechanisms of charge carriers in semiconductors. The impact ionization phenomenon happens when colliding electrons have enough energy to ionize valence band electrons. The macroscopic impact ionization rate G_{ii} is usually expressed in terms of the impact ionization coefficients of electrons and holes, $\alpha_{n,p}$ [20].

$$G_{ii} = \alpha_n \, | J_n/e| + \alpha_p \, |J_p/e| \qquad (15a)$$

The impact ionization rate of electrons, α, can be modelled as follows [21]:

$$\alpha_n(\omega_n) = \\ = \alpha_{no}.exp\left(-\frac{E_n^{I\square}}{(\omega_n-\omega_o)\left[1+\frac{(\omega_n-\omega_o)}{\eta_n E_{p\square}}\right]}\right), \qquad (15b)$$

where $\alpha_{no} = (\omega_n-\omega_o)/(\lambda_n E_n^I)$, $E_n^I = \eta_n \; E_n^{th}$, $\eta_n = (v_n \tau_{wn}/\lambda_n)$ and E_n^{th} is the threshold ionization energy of electrons. Also, E_{ph} is the optical phonon energy and λ_n is the mean free path between electron collisions (of all scattering modes). Like $\tau_{\omega n}$ and m_n, λ_n can be expressed as a function of the mean carrier energy, by MC simulation in the bulk of semi-conductor.

At moderate average carrier energies, our impact ionization model reduces to:

$$\alpha_n(\omega_n) \approx \alpha_{no}.exp\left[-\frac{E_n^I}{(\omega_n-\omega_o)}\right] \qquad (15c)$$

The above model is plotted in Fig. 3, and compared to other models. Unlike other models [21-25], the hard threshold energy (E_n^{th}) is replaced with a soft (energy-dependent) mean threshold energy (E_n^I) in our model. As shown in Fig. 4, this coincides with the conclusions of Bude and Hess about the impact ionization soft threshold energy [24].

At very low average electron energy, where $\omega_n - \omega_o = ½ m_n v_n^2$, there exists a certain probability of impact ionization. Therefore, the so-called low-voltage impact ionization, which was reported in the literature [25], is included implicitly in our model, via the convective energy.

At warm carrier regime the convective energy ($½ \; m_n \; v_n^2$) is usually in the order of acoustic phonon energy, E_{ac}, and may be much larger in certain device regions, due to velocity overshoots or ballistic transport. Therefore, it can increase the total electron energy above the threshold energy for impact ionization in nano MOSFET devices, even at low voltages.

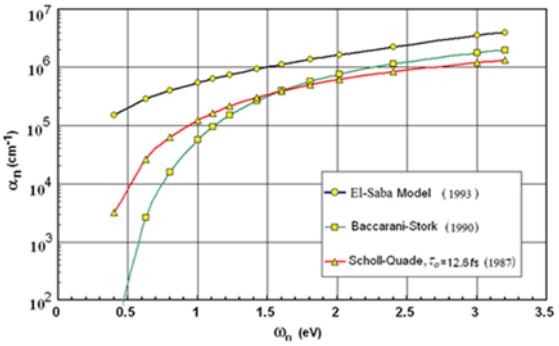

Fig. 4. Electron impact ionization rate in *Si* at 300K, as a function of average electron energy, according to Baccarani-Stork model (λ_ω = 500Å, λ_o = 65Å), Scholl-Quade model (τ_o = 14ps) and our model. In all models, the threshold ionization energy E_n^{th} = 1.2 eV.

6. Results and Discussion

The Fig. 5 shows the hydrodynamic simulation results of an N-I-N structure, representing the source-channel-drain of an n-channel MOSFET. The results are compared with those obtained by other HDM's and MC device simulation. We note that the exaggerated velocity overshoot has been suppressed when using our proposed HDM. This is primarily due to the inclusion of the convective part of the average electron energy ($½ \; m_n \; vn^2$). This convection part is descending from the tensorial product term ($n \; \boldsymbol{v}_n \otimes \boldsymbol{v}_n$), which is usually neglected in other formulations of the HDM. Such formulations are sometimes referred to as the energy-transport models (ETM). In fact the velocity gradient term ($v_n . \nabla) \; v_n$, which represents the acceleration / deceleration of electrons in the current density constitutive relation (4a), comes also from the divergence of this term $\nabla.(n \; \boldsymbol{v}_n \otimes \boldsymbol{v}_n)$. In addition, the off-diagonal elements ($v_{nj}\partial v_{ni}/\partial j$, with $i,j = x,y,z, \; i \neq j$) of the velocity gradient term, which appear in the electron mobility expression (14), are all about the electron gas viscosity. Therefore, keeping the convective transport components in our HDM is vital to capture many physical effects of the electron gas. Also, we note in Fig. 5 that the results obtained by our

HDM have more reasonable values of the electron temperature near high-field region, which are closer to MC simulation results. In fact, we can define an effective electron temperature, which combines the band structure and quantum corrections as follows:

$$T_{nm} = g_n T_n + 2/3 k_B V_{+q} \quad (16)$$

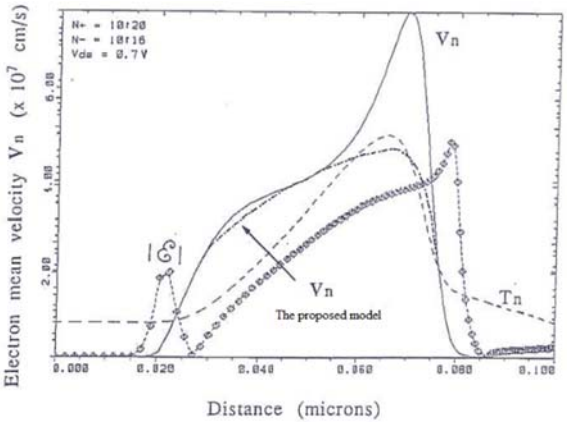

Fig. 5. Average electron velocity distributions across an N-N-I-N structure, according to our model and other models and Monte Carlo device simulation.

In another investigation of the proposed model, we simulated the bipolar transport of hot carriers across a two-dimensional reverse-biased P-I-N diode, The diode has a central (I) region of 64 um and uniform doping of 10^{14} cm^{-3}. Here, the conservation equations of carrier densities and average energies (for both electrons and holes) are solved with Poisson's equation. The Fig. 7 shows the electron and hole temperature distribution in 2D, under a reverse bias of 75 V. The surface effects are obvious near the upper surface of the diode Also, Fig. 6 show the energy flux distributions of electrons and holes of the same diode under a reverse bias of -500 V.

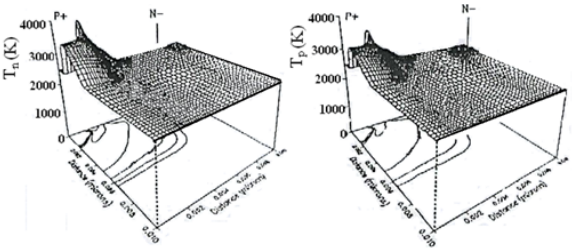

Fig. 6. Carrier temperature distributions across the P-I-N diode at reverse bias of 75 V.

7. Conclusions

In this paper, we proposed an advanced HDM for semi-conductors with arbitrary band structure and including electron gas viscosity and surface effects. There exists a few number of energy-dependent parameters, which can be determined by full-band MC simulation in the semiconductor of interest. Fortunately, almost all the model parameters are measurable physical quantities. In particular, the energy relaxation time captures the energy band structure and the dominant scattering mechanism, near the surface of semi-conductor [27]. The model has been appended with other transport models. The primary results are closer to the MC device simulation. For instance, the over-estimated electron velocity overshoot in nano-devices, has been relatively suppressed. The role of electron velocity gradients is emphasized and the underlined electron gas viscosity is therefore considered. The electron gas viscosity effects are particularly important to justify the mobility reduction near the surface of semi-conductor devices. Finally, the authors would like to attract the attention to the vital role of electron gas viscosity effects in semiconductor device modelling, which we think not reported yet in the [28]. Of course, more investigations about the proposed HDM and more comparisons with other approaches are required.

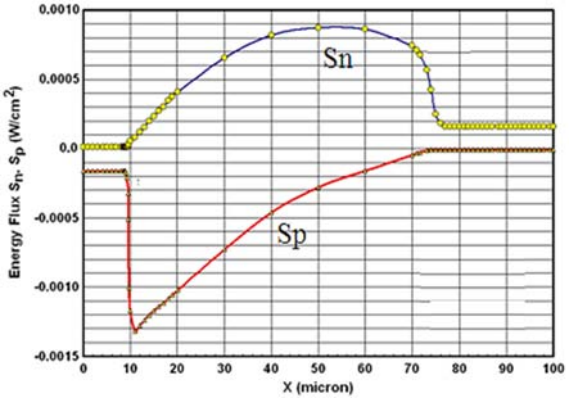

Fig. 7. Energy flux of electrons and holes along the P-I-N diode at 500 V reverse bias.

References

[1]. M. H. El-Saba, Transport of Information-Carriers in Semiconductors and Nanodevices, *IGI Global Publisher*, PA, USA, 2017.

[2]. B. Meinerzhagen, R. Thoma, H. J. Peifer, W. L. Engl, On the Consistency of the Hydro-dynamic and the Monte Carlo Models, http://www.researchgate.net/publication/37920832

[3]. M. Stettler, M. Alam, M. Lundstrom, A Critical examination of the assumptions underlying macroscopic transport equations for silicon devices, *IEEE Trans. Electron. Dev.*, Vol. 40, Issue 4, 1993, pp. 733-740.

[4]. C. Jungemann, T. Grass, B. Neinhilus, B. Meeinerzhagen, Failure of moments-based transport models in nanoscale devices near equilibrium, *IEEE Trans. Electron. Dev.*, Vol. 52, Issue 11, November 2005, pp. 2404-2408.

[5]. G. Wolodkin, J. Frey, Overshoot effects in the relaxation time approximation, in *Proceedings of the Eight International Conference on the Numerical*

Analysis of Semiconductor Devices and Integrated Circuits NASCODE VIII, Vienna, 1992, pp. 107-108.

[6]. M. H. El-Saba, Accurate estimation of electron velocity overshoots in sub-0.1 micron silicon structures and MOSFET devices, in *Proceedings of the 15th Radio Science Conference (NRSC'98)*, 1998, pp. D2/1-D2/5.

[7]. D. Chen, E. C. Kan, U. Ravaioli, W.-C. Shu, R. W. Dutton, An improved energy transport model including non-parabolicity and non-Maxwellian distribution effects, *IEEE Trans. Electron. Dev. Lett*., Vol. 13, Issue 1, 1992, pp. 26-28.

[8]. M. H. El-Saba, Accurate Non-local modeling of hot-carriers drift mobility in semiconductor devices, in *Proceedings of the 8th Int. Conference on Microelectronics*, Cairo, 1996.

[9]. M. H. El-Saba, Problems related to the semiconductors hydrodynamic model: modeling the carrier-heat flux term, in *Proceedings of the 8th Int. Conference on Microelectronics*, Cairo, 1996, pp. 162-166.

[10]. V. Romano, Non-parabolic band hydrodynamic model of silicon semiconductors and simulation of electron devices, *Mathematical Methods in the Applied Sciences*, Vol. 24, Issue 7, 2001, pp. 439-471.

[11]. C. Jacoboni, P. Lugli, The Monte Carlo Method for Semi-conductor Device Simulation, *Springer Science*, 2012.

[12]. A. J. Sabbah, D. M. Riffe, Femto-second pump-probe reflectivity study of silicon carrier dynamics, *Phys. Rev. B*, Vol. 66, 2002, pp. 165217-165228.

[13]. B. Gonzalez, V. Palankovsk, H. Kosina, A. Hernandez, S. Selberherr, An analytical energy relaxation time model for device simulation, *Solid-State Electron*, Vol. 43, 1999, pp. 1791-1795.

[14]. E. Sermuknis, J. Liberis, A. Matulionis, Microwave noise technique for measurement of hot-electron energy relaxation time and hot-phonon lifetime, *Lithuanian Journal of Physics*, Vol. 47, Issue 4, 2007, pp. 491-498.

[15]. M. Mohyee-Edin, K. Sehrawy, M. S. Taha, M. H. EL-Saba, Electro-kinetic pressure correction parameter of hydrodynamic model calculation, using Monte Carlo simulation, in *Proceedings of the International Conference on Microelectronic Devices and Technologies (MicDAT'24)*, Ibiza, Spain, 25-27 Sept. 2024 (submitted).

[16]. K. W. Böer, U. W. Pohl, Semiconductor Physics. *Springer*, 2018.

[17]. A. Jüngel, D. Matthes, A derivation of the isothermal quantum hydrodynamic equations using entropy minimization, Z. angew. Math. Mech., Vol. 85, 2005, pp. 806-814.

[18]. D. K. Ferry, S. Ramey, L. Shifren, E. Alkis, The effective potential in device modeling: the good, the bad and the ugly, *Journal of Comp. Electron*., Vol. 1, Issue 1, 2002, pp. 59-65.

[19]. M. S. Taha, M. H. EL-Saba, A unified mobility model, including band structure and semiconductor surface effects, in *Proceedings of the International Conference on Microelectronic Devices and Technologies (MicDAT'24)*, Ibiza, Spain, 25-27 Sept. 2024 (submitted).

[20]. M. H . El-Saba, Yet another hydrodynamic model for silicon devices with correlated parameters, scientific and academic publishers, *Microelectronic Devices and Solid-State Electronics*, Vol. 1, Issue 5, 2012, pp. 118-147.

[21]. M. H. El-Saba, Accurate modeling of energy-dependent impact ionization rate for hydrodynamic simulators of semiconductor devices, in *Proceedings of the IEEE Radio Science Conference (NRSC'99)*, 23-25 Feb. 1999, pp. D2/1-D2/5.

[22]. E. Schöll, W. Quade, Effect of impact ionisation on hot-carrier energy and momentum relaxation in semiconductors, *J. Phys. C: Solid State Phys.*, Vol. 20, 1987, pp. L861-L867.

[23]. E. F. Crabbé, H. Stork, G. Baccarani, M. V. Fischetti, S. E. Laux, The impact of non-equilibrium transport on breakdown and transit time in bipolar transistors, in *Proceedings of the International Electron Devices Meeting*, 1990.

[24]. P. Su, K-I. Goto, T. Sugii, C. Hu, A thermal activation view of low voltage impact ionization in MOSFETs, *IEEE Electron. Dev. Let*., Vol. 23, Issue 9, 2002, pp. 550-552.

[25]. J. Bude, K. Hess, Threshold of impact ionization in semiconductors, *J. Appl. Phys*., Vol. 72, Issue 8, 1992, 3554.

[26]. N. Nida, U. Grossner, High temperature impact-ionization model for 4H-SiC, *IEEE Trans. E. Devices*, Vol. 66, Issue 4, 2019, pp. 1899-1904.

[27]. J. Billiald, D. Backes, J. König, I. Farrer, D. Ritchie, V. Narayan, Determining energy relaxation length scales in two-dimensional electron gases, *Applied Physics Letters*, Vol. 107, 2015, 022104.

[28]. P. S. Alekseev, A. P. Dmitriev, Viscosity of two-dimensional electrons, *arXiv Preprint*, 2021, arXiv:2007-02291v4.

Sensors & Transducers, Vol. 267, Issue 4, December 2024, pp. 57-64

www.sensorsportal.com

Sensors & Transducers

Published by IFSA Publishing, S. L., 2024
http://www.sensorsportal.com

Comparison of Experimental and Theoretical Modeling of Temperature Drift in Off-Diagonal GMI Sensors

[*] Pape Abdoulaye FAM, [*] Papa Silly TRAORE and Mamaye Inès CORREA
Ecole Supérieure Polytechnique (ESP), Université Cheikh Anta Diop (UCAD), Dakar, Sénégal
Tel.: (+221) 77 399 99 41
E-mail: papasilly.traore@esp.sn

Received: 11 June 2024 / Revised: 26 December 2024 / Accepted: 28 December 2024
Published: 30 December 2024

Abstract: This article investigates the temperature sensitivity of digital Magneto-Impedance (GMI) sensors by comparing experimental data with theoretical predictions. The study demonstrates that the experimental results are in excellent agreement with the theoretical model, showing a high level of consistency within the examined dynamic range. Notably, the sensitivity of the sensor at the zero bias point is significantly lower than at other bias points, with a measured sensitivity of approximately -0.2 mΩ/°C, validating simulation predictions. The linearity around the zero bias point also aligns with theoretical expectations. The agreement between experimental and theoretical results is strong for positive fields and those near zero, with theoretical values within established confidence intervals. However, a significant discrepancy was noted between -10 and -31 µT, suggesting areas for further improvement. This work confirms the reliability of the theoretical model while identifying areas needing further research. It provides a basis for enhancing the thermal stability of GMI sensors and reducing temperature-induced drift, paving the way for advancements in magnetic sensing applications.

Keywords: GMI sensor, Temperature drift, Sensitivity, Off-diagonal configuration.

1. Introduction

The Giant Magneto-Impedance (GMI) effect observed in amorphous wires represents a significant advancement in the field of magnetic sensing technology [1]. This phenomenon occurs when a magnetic conductor, typically in the form of a wire with an amorphous structure, experiences a dramatic change in its electrical impedance under the influence of a high-frequency alternating current and an external magnetic field [2, 3]. The sensitivity of the GMI effect is such that even minor variations in the magnetic field can induce substantial changes in the impedance, making these materials highly attractive for applications that require precise magnetic field measurements [3].

GMI-based sensors are particularly noteworthy for their potential in creating highly sensitive magnetometers and magnetic sensors. These devices are capable of detecting extremely weak magnetic fields with high accuracy, which is crucial in a variety of domains. For instance, in biomedical imaging, GMI sensors can be used to detect tiny magnetic signals generated by biological tissues, providing valuable diagnostic information [4]. In geophysics, they can be employed to map subtle variations in the Earth's magnetic field, aiding in mineral exploration and environmental monitoring. Furthermore, their application in navigation systems and industrial automation highlights the versatility of GMI sensors in real-time magnetic field detection [4].

Despite these advantages, the broader adoption of GMI sensors has been hindered by a critical limitation:

their sensitivity to temperature fluctuations. The impedance of GMI materials is not only dependent on the magnetic field but also on the ambient temperature, which can cause significant drift in sensor readings [5]. This temperature-induced drift is particularly problematic in practical applications where the sensor may be exposed to varying environmental conditions. For example, in industrial settings or field applications, where temperatures can fluctuate widely, the accuracy of GMI sensors can be compromised, leading to unreliable data and reduced sensor performance.

To address these challenges, our study focuses on a detailed investigation of the temperature drift characteristics of GMI sensors. The aim is to quantify the impact of temperature variations on the impedance and performance of these sensors, and to explore potential methods for mitigating these effects. A rigorous experimental setup that allows us to measure the temperature dependence of the GMI effect is developed. This setup includes controlled thermal environments and measurement tools to ensure accurate data collection across a range of temperatures.

In addition to the experimental approach, we will compare our empirical results with theoretical models. These models, based on the underlying physics of the GMI effect, predict how temperature influences impedance changes in amorphous wires. By validating these models against experimental data, we aim to deepen our understanding of the temperature dependence of GMI sensors and identify strategies to improve their thermal stability.

Section 1 provides an understanding of the principle of the off-diagonal configuration of the GMI wire. Section 2 details a theoretical model of temperature sensitivity. Section 3 presents the measurement setup and compares the measurement results with the theoretical model. The paper concludes with a summary of findings and potential future directions.

2. The off-diagonal Configuration

After the discovery of GMI effect, micro-GMI wires were initially used in their classic configuration [2, 3]. This setup involves exciting the material by a current i_1, with the sensor output v_1, being the voltage measured across the element itself (Fig. 1.a). In the last two decades, a new GMI structure called, the off-diagonal configuration was discovered [6-8]. This new technique proposes measuring the field-modulated voltage v_2, across a pick-up coil coupled to the sensitive element, as illustrated in Fig. 1.b. Fig. 1 shows the structure of the classical and off diagonal configuration of the GMI wire.

This technique has long been used in Fluxgate sensors [9]. It is primarily based on the appearance of longitudinal magnetization within the wire when it is traversed by a high-frequency excitation current [6], which creates a circumferential field around the conductor. The axial component of this magnetization generates the flux that the pick-up coil can detect. One of the main advantages of this magnetic configuration is its potential to increase the sensor's sensitivity and to improves its linearity by improving the number of turns of the pick-up coil [7]. This new magnetic configuration used in our setup, can be seen as quadripolar representation as shown in Fig. 2.

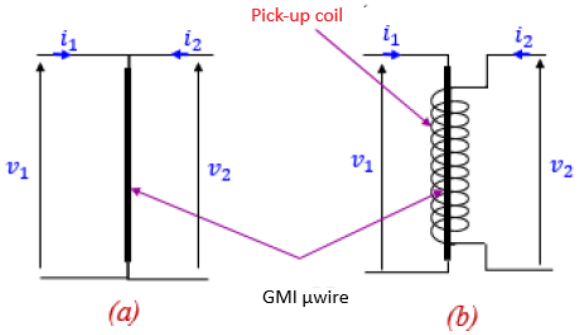

Fig. 1. (a) Classic GMI structure,
(b) GMI wire used in off-diagonal configuration.

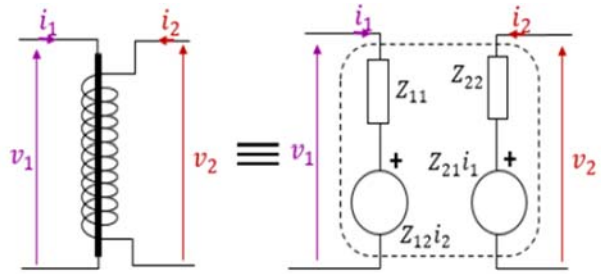

Fig. 2. Quadripolar representation of the wire
in off-diagonal configuration.

The GMI structure can be modelled as an impedance matrix according to [10]:

$$\begin{pmatrix} v_1 \\ v_2 \end{pmatrix} = \begin{pmatrix} Z_{11} & Z_{12} \\ Z_{21} & Z_{22} \end{pmatrix} \begin{pmatrix} i_1 \\ i_2 \end{pmatrix} \quad (1)$$

where v, i are the voltage and current matrices of the quadrupole, respectively.

The impedance matrix from equation (1) shows four terms corresponding to different modes of excitation and detection:

- Z_{11}: μfil excited by current, with the output taken across the wire itself.
- Z_{21}: μfil excited by current, with the output taken across the detection coil.
- Z_{12}: Coil excited by current, with the output taken across the μfil.
- Z_{22}: Coil excited by current, with the output taken across the coil itself.

The impedances of the quadrupole in the off-diagonal GMI configuration, can be expressed in terms of the magnetic mode impedance Z_M and the non-magnetic mode impedance Z_N as follows [11]:

$$Z_{11} = \frac{l}{2\pi a}(Z_M cos^2\theta_M + Z_N sin^2\theta_M) \quad (2)$$

$$Z_{21} = Z_{12} = N(Z_N - Z_M) sin\theta_M cos\theta_M \quad (3)$$

$$Z_{22} = \frac{2\pi a N^2}{l}(Z_M sin^2\theta_M + Z_N cos^2\theta_M) \quad (4)$$

with θ_M designates the equilibrium position of the magnetization, a is the radius of the micro-wire, N the number of turns of the pick-up coil.

Recently, several studies show that the off-diagonal component $Z_{12}= Z_{21}$ is significantly more advantageous compare to the other impedance because it reduces the contribution of white noise [10, 12, 13]. Therefore, it is more beneficial to use this structure (where the wire is excited by current, and the voltage across the coil is detected) in the implementation of GMI sensors [14-15].

3. Theoretical Model of Temperature Sensitivity

The temperature sensitivity S_{T21} of the GMI wire in off-diagonal configuration, expressed in Ω/K, indicates the variation of its impedance as a function of temperature. It is given by:

$$S_{T21} = \frac{dZ_{21}}{dT} \quad (5)$$

From equation (3), the impedance of the wire in off-diagonal mode is expressed, as a function of all the wire's parameters, such as the applied field *B*, the bias current I_{dc}, the magnetization and magnetic anisotropy angles θ_M and θ_k, the excitation frequency f_{ac}, the temperature *T*, and the resistivity $\rho(T)$, according to [5]:

$$Z_{21} = \frac{N}{2} sin(2\theta_M)\left[\frac{2}{a}\rho(T) + \frac{j}{2}\mu_0 a\pi f_{ac} - (1+j)\mu_0 M_s(T)\sqrt{\frac{\pi f_{ac}\rho(T)}{\alpha_{int}(\theta_M,\theta_k)+\beta_{int}(B,I_{dc},\theta_M,T)}}\right] \quad (6)$$

where μ_0 is the permeability of free space, α_{int} and β_{int} are temperature-dependent functions such that:

$$\alpha_{int} = 2k_u \cos\big(2(\theta_k - \theta_M)\big) \quad (7)$$

$$\beta_{int} = \mu_0 M_s(T)\big[H_z(B)\cos\theta_M + H_\varphi(I_{dc})\sin\theta_M\big] \quad (8)$$

Temperature also affects the magnetization angle; this implies that in the calculation of the partial derivative of impedance, the partial derivative of the magnetization angle with respect to temperature must be considered. Knowing the parameters on which the impedance depends, we can establish equation (9), assuming that the quantities f_{ac}, I_{dc}, and θ_k are constant.

$$dZ_{21}[B, I_{dc}, f_{ac}, \theta_M, \theta_k, T] = \frac{\partial Z_{21}}{\partial T}dT + \frac{\partial Z_{21}}{\partial \theta_M}d\theta_M + \frac{\partial Z_{21}}{\partial B}dB \quad (9)$$

Since the applied magnetic field is independent of the ambient temperature, the term $\frac{dB}{dT} = 0$; thus, the temperature sensitivity becomes:

$$S_{T21} = \frac{dZ_{21}}{dT} = \frac{\partial Z_{21}}{\partial T} + \frac{\partial Z_{21}}{\partial \theta_M}\frac{\partial \theta_M}{\partial T} \quad (10)$$

By considering the partial variations of Z_{21} with respect to θ_M, and expressing the variations of θ_M as a function of T, the expression for the temperature sensitivity of the off-diagonal MIG is established as follows [5]:

$$S_{T21} = \frac{N}{6a}\cos 2\theta_M[B,T]\left[12\rho[T] + ja\mu_0 f_{ac}\left(3a\pi - 2(1-j)M_s[T]\sqrt{\frac{3\pi\rho[T]}{f_{ac}k_u}}\right)\right] \times -(1+j)\frac{N}{2}\sin 2\theta_M \times \left\{\sqrt{\frac{\pi f_{ac}\rho[T]}{\alpha_{int}+\beta_{int}}}\mu_0 M'_s[T] - (1-j)\frac{\rho'[T]}{a} + \sqrt{\frac{\pi f_{ac}}{\rho[T]}}\mu_0 M_s[T]\left(\frac{(\alpha_{int}+\beta_{int})\rho'[T] - \rho[T]\frac{\partial\beta}{\partial}}{(\alpha_{int}+\beta_{int})^{3/2}}\right.\right. \quad (11)$$

The off-diagonal component and temperature sensitivity, according to equations (6) and (11), were then simulated. The simulation parameters correspond to the used microwire from Unitika Ltd. The characteristics are summarized in the Table 1. Fig. 3 shows the dependance of the off-diagonal component in function of the temperature.

Fig. 4 shows the dependance of the temperature sensitivity for different bias field.

Obtained results show that the temperature sensitivity also depends on the chosen bias point, and its variation is influenced by the sign of the applied bias field. For the used GMI wire, this variation is almost linear between -10 and 10 μT. We also note that for a zero bias field, the sensitivity is nearly zero (≈20 nΩ/°C); in other words, at this point, the sensor is insensitive to temperature. This is an interesting observation, indicating that when the bias is properly selected ($Bp = 0$), the sensor may no longer be affected by temperature. Moreover, the uniqueness of this point lies in the fact that, in the case of the off-diagonal configuration, it offers better field sensitivity and a lower noise level [10, 13, 14].

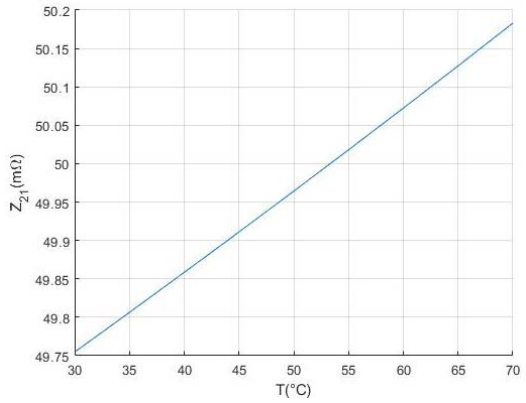

Fig. 3. Evolution of the MIG Impedance (mΩ) as a Function of Temperature (°C).

Table 1. List of parameters used in our simulation.

Data	Value
Wire diameter, (d=2a)	100 μm
Length of the wire, (l)	24 mm
Number of turn ($\mathcal{N}$)	340
Anysotropy angle θk	85°
DC bias current Idc	5 mA
Static Circumferential Field Hφ (A/m)	$Idc/\pi d$
Curie Temperature, Tc	673 K
α	0.238 $n\Omega/mK$
β	1.52 $\mu\Omega/m$
Résistivy ρ(Ω/m)	$238.10^{-12}\,T + 1{,}52.10^{-6}$
Anisotropy Constant ku	5.636
Saturation Magnetization Ms(kA/m)	$191.43(1-e^{(T-Tc)/97})$
Champ axial Hz(A/m)	$Hz=B/\mu_0$

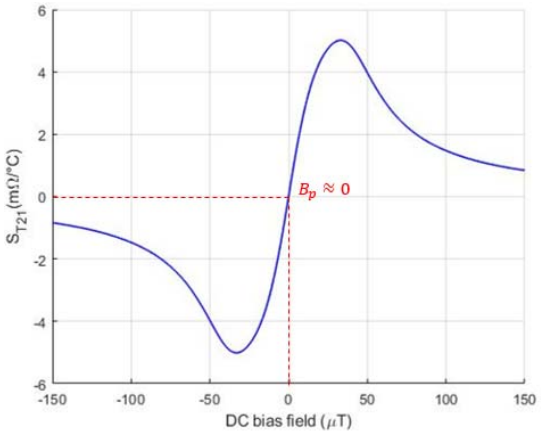

Fig. 4. Variation of the Temperature Sensitivity of the Wire for Different Operating Points in the Magnetic Field.

4. Measurement Setup

To validate our theoretical model, simulations were performed using the digital off-diagonal GMI sensor described in our recent work [13-16]. Fig. 5 illustrates the digital GMI sensor implemented in [2]. In this setup, the FPGA (Field Programmable Gate Array) circuit is situated beneath the heat sink. The wire excitation (I_{ac} and I_{dc}) is provided by a digital frequency synthesizer (DDS, or Direct Digital Synthesizer). When an external magnetic field is applied to the sensing element in off-diagonal configuration, the voltage across the pick-up coil is amplitude-modulated by the measured field. This voltage is then transmitted to the board via the digital receiver input (SDR, or Software Defined Radio) for a quadrature digital demodulation. Both the excitation system and the digital receiver functionalities are implemented in software within the FPGA [14, 17].

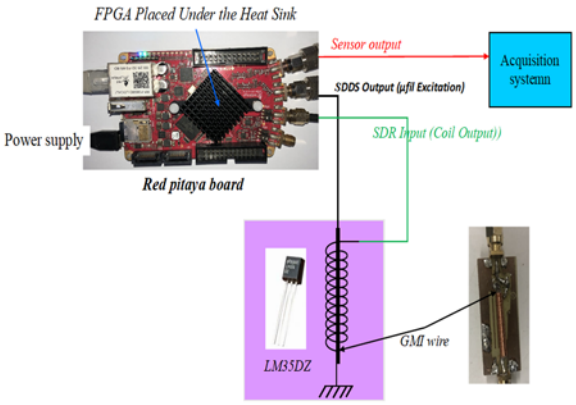

Fig. 5. Wiring around the FPGA Red Pitaya Development Board for Temperature Sensitivity Measurement.

The demodulated output signal is then digitized using a 16-bit data acquisition system to monitor the sensor's response to temperature variations. Measurements are conducted in a non-shielded environment. The GMI element in the off-diagonal configuration and a temperature sensor (LM35 DZ), which is used to monitor the ambient temperature, are housed within a box covered with aluminum foil. Hot air is blown into this box to create controlled temperature conditions.

To better evaluate the temperature sensitivity of the sensor, initial measurements were performed by heating the sensitive element and observing the sensor's output. Fig. 6 shows the behavior of the sensor's output over time when the GMI wire is subjected to different temperatures. This measurement was obtained under a polarization field of 10 µT.

The experimental results demonstrate the temperature sensitivity of the GMI-based sensor. In fact, when the temperature remains constant, the sensor's output is stable, indicating good reliability under steady thermal conditions.

As the temperature rises, the sensor's output increases. This behavior is attributed to changes in the magnetic and electrical properties of the GMI wire, such as magnetic permeability and impedance, which are temperature-dependent. When the heating stops, the sensor's output decreases along with the temperature, demonstrating a reversible relationship between temperature and output signal.

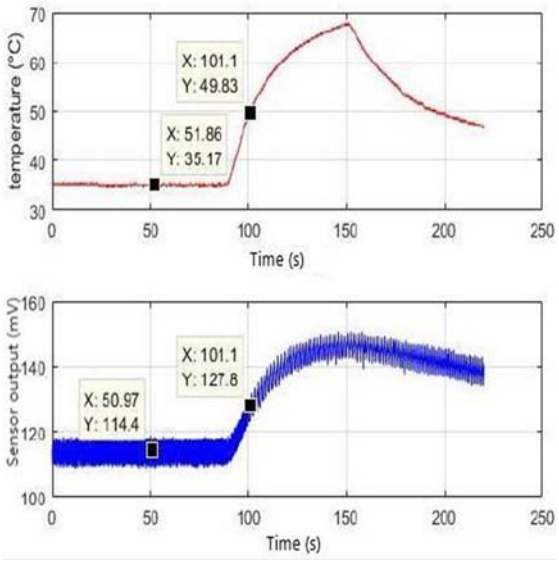

Fig. 6. Behavior of the offdiagonal GMI sensor output in function of the temperature for a bias magnetic fielf of 10 µT.

These results highlight the sensor's high sensitivity to temperature changes. This sensitivity can be advantageous for thermal monitoring applications but may require compensation in scenarios where temperature stability is crucial for magnetic field measurements.

To validate our theoretical approach, a measurement campaign was then conducted, followed by a statistical analysis to bound the results. To compare data under identical acquisition conditions, error bars were utilized. These graphical representations of variability illustrate whether differences between results are statistically significant. The error bars, most commonly associated with standard deviations, standard errors, or confidence intervals, provide an indication of the accuracy or uncertainty of the presented measurements.

For this study, a 95 % confidence interval (CI) was used to estimate the true value based on random sampling. The CI ensures that 95% of the observed means lie within approximately $\pm 2\sigma/\sqrt{N}$, where σ is the standard deviation, and N is the number of measurements. This statistical approach also determined the minimum number of samples required to achieve reliable results at this confidence level. Fig. 7 shows the measurement temperature sensitivity as a function of the bias magnetic field.

Fig. 8 shows an overlay of the measurement results with those from the theoretical model developed according to Equation (11).

This overlap of experimental and practical results confirms the theoretical model. Indeed, the practical results show a sensitivity profile that matches the one traced from the mathematical model within the dynamic range. Furthermore, at the zero bias point, the observation made in the simulation is confirmed by the measurements, with a sensitivity much lower than at other points, approximately -0.2 mΩ/°C. Similarly, the linearity observed around zero is also reflected in practice.

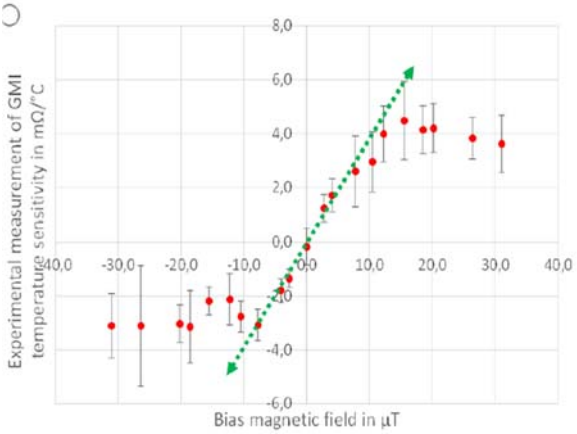

Fig. 7. Experimental behaviour of GMI Temperature sensitivity in mΩ/°C versus DC bias magnetic field in µT.

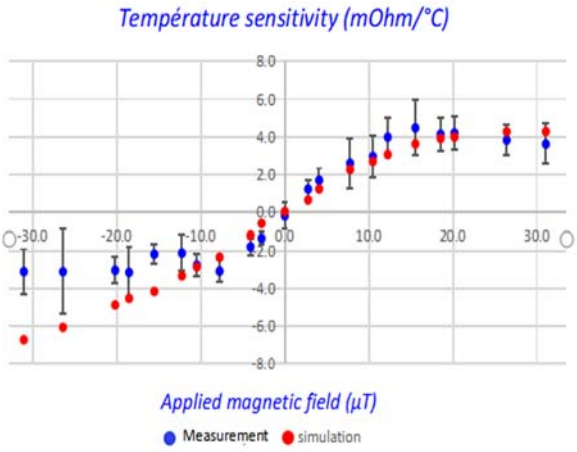

Fig. 8. Overlay of experimental and theoretical Results.

In summary, a good agreement is observed, especially for positive fields and fields around zero, with theoretical values falling within the established confidence intervals. However, a significant discrepancy is noted between -10 and -31 µT.

The observed difference between theory and practice can primarily be attributed to the theoretical parameters used in our simulation, such as the magnetic anisotropy field, the saturation magnetization, and the magnetic anisotropy angle. To better understand the impact of each parameter, several simulations were conducted. Fig. 9 shows the behavior of temperature sensitivity for different values of the magnetic anisotropy field.

A discrepancy is observed starting from −20 µT towards the more negative fields. When its magnitude decreases from 46 to 34 A/m, the sensitivity curve rises starting from −20 µT. An interesting observation,

since in Fig. 8, a similar discrepancy between the theoretical and practical curves is noted starting from −10 μT.

In the state of the art, the saturation magnetization values are typically on the order of a few hundred kA/m. We have again simulated the temperature sensitivity by first multiplying it by 2, then by 0.8. Fig. 10 shows the obtained results.

We observe that the saturation magnetization has a slight influence on the shape of the sensitivity curve. When it decreases from 191430 to 153144 A/m, its influence remains negligible, as practically its value is on the order of 190000 A/m.

Fig. 11 shows the theoretical temperature sentivity curves for different value of anisotropy angle.

The variation of the anisotropy angle, like the anisotropy field, does have an influence on the sensitivity. When it changes from −85 to 90° C, the sensitivity curve rises starting from −10 μT and is slightly lowered from 10 μT onwards. These observations are similar to the experimental curve obtained.

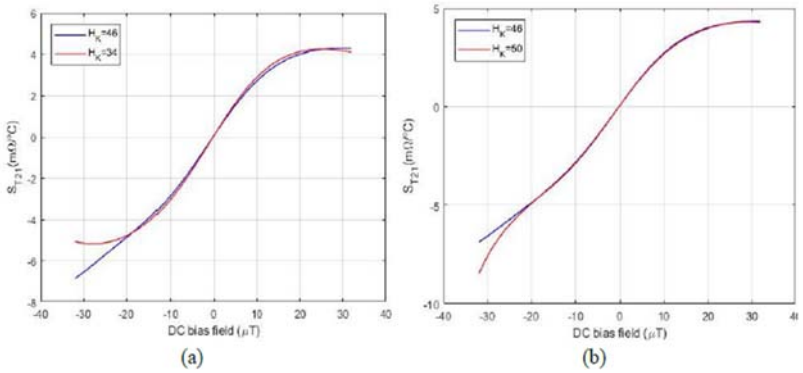

Fig. 9. Theoretical temperature sensitivity curves for an anisotropy of 46 A/m (used previously). (a) In red, a new anisotropy value of 34 A/m; (b) In red, a new anisotropy value of 50 A/m.

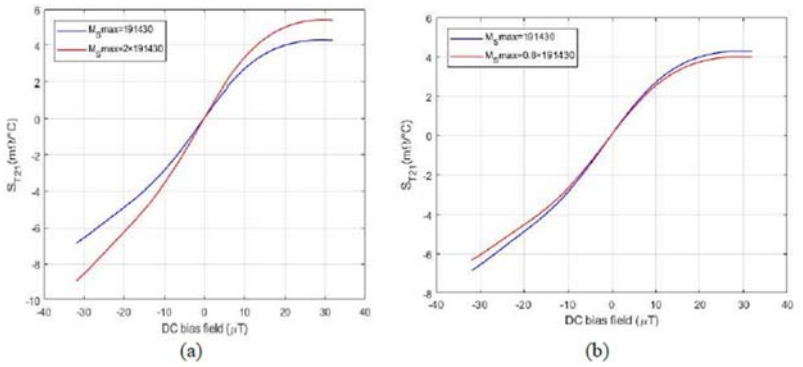

Fig. 10. Theoretical sensitivity curves with respect to temperature for a maximum saturation magnetization of 191430 A/m (used previously). In red, an amplitude of 2**191430 A/m; (b) In red, an amplitude of 0.8**191430 A/m.

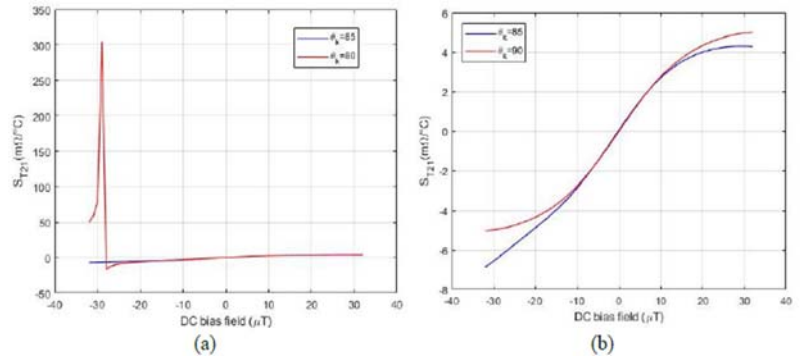

Fig. 11. Theoretical temperature sensitivity curves for an anisotropy angle of 85° (used previously). (a) In red, the angle is 80°; (b) In red, the angle is 90°.

The analysis of the modification of these intrinsic parameters in the GMI wire shows that the quantities whose variation has the most influence on the agreement between the theoretical and practical curves are the magnetic anisotropy field and the magnetization angle. In fact, magnetic anisotropy (both magnitude and direction) results from the tendency of spin moments to align along an easy magnetization direction rather than a hard magnetization direction. This anisotropy is typically linked to the crystalline structure or shape of the material. It arises from interactions between the electronic spins and the crystal field of the material, as well as from demagnetizing fields (shape anisotropy).

In the case of amorphous wires, the magnetic anisotropy that remains is largely due to mechanical stresses introduced during the rapid solidification process during manufacturing. These stresses typically result in a constant anisotropy field. However, this anisotropy field can change when the wire is subjected to additional mechanical stress.

During the fabrication of the sensing element (comprising the wire and detection coil), the wire was in contact with metallic tools such as soldering irons and cutting pliers, which bent or heated the wire. These processes altered the previously defined anisotropy properties established by the manufacturer, thereby introducing slight variations in the magnetic characteristics of the wire. These variations are likely responsible for the small discrepancy observed between the theoretical simulations and the experimental measurements.

5. Conclusion

This article provides a comprehensive analysis of the temperature sensitivity of a digital GMI (Giant Magnetoimpedance) sensor by comparing experimental results with theoretical predictions. The experimental data demonstrate a strong alignment with the theoretical model, particularly within the dynamic range studied. This consistency validates the robustness of the model, confirming that it accurately predicts the sensor's behavior under varying conditions.

At the zero bias point, the measured sensitivity is significantly lower than at other points, which aligns well with the theoretical predictions, where the sensitivity is approximately -0.2 mΩ/°C. This result is particularly important as it supports the validity of the theoretical approach, highlighting the precise control of temperature sensitivity around this critical point. Furthermore, the linearity observed around the zero bias point is also in excellent agreement with theoretical expectations, further confirming the accuracy of the model.

The agreement between experimental and theoretical results is notably strong for positive magnetic fields and those near zero, where the theoretical values fall within the established confidence intervals. This consistency suggests that the model accurately captures the key physical phenomena governing the sensor's performance in these regions. However, a notable discrepancy was observed in the range of -10 to -31 μT, where the experimental data deviated from the theoretical predictions. This discrepancy points to areas where the model may require refinement or where additional factors—such as material imperfections or measurement errors—may be influencing the results.

These findings not only validate the strength and reliability of the theoretical model but also reveal areas for potential improvement. Ultimately, the results of this study pave the way for further developments in the field, offering valuable insights that can contribute to enhancing the accuracy and reliability of GMI sensors in practical applications, particularly in fields such as medical devices, industrial sensing, and environmental monitoring.

References

[1]. K. V. Rao, F. B. Humphrey, J. L. Costa-Kramer, Very large magnetoimpedance in amorphous soft ferromagnetic wires, *Journal of Applied Physics*, Vol. 76, Issue 10, 1994, pp. 6204-6208.

[2]. L. Panina, K. Mohri, Magneto-impedance effect in amorphous wires, *Applied Physics Letters*, Vol. 65, 1994, pp. 1189-1191.

[3]. E. P. Harrison, G. L. Turney, H. Rowe, Electrical properties of wires of high permeability, *Nature*, Vol. 135, Issue 3423, 1935, pp. 961.

[4]. P. Ripka, Magnetic Sensors and Magnetometers, *Artech House Publisher*, 2001.

[5]. A. Esper, B. Dufay, S. Saez, C. Dolabdjian, Theoretical and Experimental Investigation of Temperature-Compensated Off-Diagonal GMI Magnetometer and Its Long-Term Stability, *IEEE Sensors Journal*, 20, 16, 2020, pp. 9046-9055.

[6]. L. Kraus, M. Malatek, M. Dvorak, Magnetic field sensor based on asymmetric inverse Wiedemann effect, *Sensors and Actuators A: Physical*, Vol. 142, Issue 2, 2008, pp. 468-473.

[7]. A. S. Antonov, I. T. Iakubov, A. N. Lagarkov, Longitudinal-transverse linear transformation of the HF-current in soft magnetic materials with induced anisotropy, *IEEE Transactions on Magnetics*, Vol. 33, Issue 5, 1997, pp. 3367-3369.

[8]. S. Sandacci, D. Makhnovskiy, L. Panina, K. Mohri, Y. Honkura, Off-diagonal impedance in amorphous wires and its application to linear magnetic sensors, *IEEE Transactions on Magnetics*, Vol. 40, Issue 6, Nov. 2004, pp. 3505–3511.

[9]. E. Paperno, Suppression of magnetic noise in the fundamental-mode orthogonal fluxgate, *Sensors and Actuators A: Physical*, Vol. 116, Issue 3, October 2004, pp. 405–409.

[10]. B. Dufay, S. Saez, C. P. Dolabdjian, A. Yelon, D. Ménard, Characterization of an optimized Off diagonal GMI-based Magnetometer, *IEEE Sensor Journal*, Vol. 13, Issue 1, January 2013, pp. 379-388.

[11]. L. Ding, Étude et amélioration des performances en bruit de capteurs à MagnétoImpédance Géante: Application à la magnétométrie à très haute sensibilité, Thèse de Doctorat en Électronique et

Microélectronique, *Université de Caen*, 2008 (in French).
[12]. M. Malatek, B. Dufay, S. Saez, C. Dolabdjian, Improvement of the off-diagonal magnetoimpedance sensor white noise, *Sensors and Actuators A: Physical*, Vol. 204, December 2013, pp. 20–24.
[13]. P. S. Traoré, A. Asfour, J. P. Yonnet, C. Dolabdjan, Noise Performance of SDR-Based Off-Diagonal GMI Sensors, *IEEE Sensors Journal*, Vol. 17, Issue 19, October 2017, pp. 6175-6184.
[14]. P. S. Traoré, A. Asfour, J. P. Yonnet, Design Approach for an Off-Diagonal Giant Magneto Impedance Sensor Based on Field Programmable Gate Array, *Sensors and Transducers*, Vol. 245, Issue 6, October 2020, pp. 20-26.
[15]. P. S. Traoré, S. Konan, A. Asfour, J. P. Yonnet, Analysis of the impact of the processing time-delay on the stability of a digital GMI magnetometer, in *Proceedings of the IEEE Sensors Conference*, 31 October 4 November 2021, pp. 1-4.
[16]. P. S. Traoré, A. Asfour, S. Konan and J. -P. Yonnet , Stability Criteria of a High Sensitivity Digital GMI Magnetometer, *IEEE Transactions on Magnetics*, Vol. 59, Issue 2, February 2023, 6100204.
[17]. P. S. Traoré, A. Asfour, J.-P. Yonnet, C. Boudinet, Introduction of real-time digital processing techniques for the high-sensitivity GMI sensors, *International Journal of Applied Electromagnetics and Mechanics*, Vol. 59, Issue 2, 2019, pp. 455-463.

Theory:

Digital Sensors and Sensor Systems: Practical Design

and

Practice:

Development Board EVAL UFDC-1/UFDC-1M-16

+

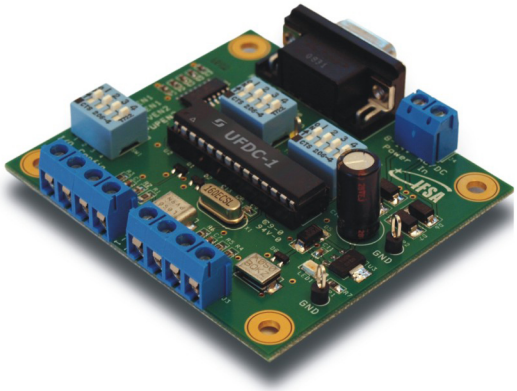

Buy book and Evaluation board together. **Save 30.00 EUR**

Development Board EVAL UFDC-1 / UFDC-1M-16

Full-featured development kit for the Universal Frequency-to-Digital Converters UFDC-1 and UFDC-1M-16. 2 channel, 16 measuring modes, high metrological performance, RS232/USB interface, master and slave communication modes. On-board frequency reference (quartz crystal oscillator). Operation from 8 to 14 V AC/DC. Development board software is included.

All existing frequency, period, duty-cycle, time interval, pulse-width modulated, pulse number and phase-shift output sensors and transducers can be directly connected to this 2-channel DAQ system. The user can connect TTL-compatible sensors' outputs to the Development Board, measure any output frequency-time parameters, and test out the sensor systems functions.

Applications:

- Digital sensors and sensor systems
- Smart sensors systems
- Data Acquisition for frequency-time parameters of electric signals
- Frequency counters
- Tachometers and tachometric systems
- Virtual instruments
- Educational process in sensors and measurements
- Remote laboratories and distance education

Order online:
http://www.sensorsportal.com/HTML/BOOKSTORE/Digital_Sensors_and_Board.htm

IFSA

International Frequency Sensor Association Publishing

www.sensorsportal.com

ISSN 1726- 5479